# Mechanical behavior of solid helium: elasticity, plasticity and defects

John Beamish*

*Department of Physics,*
*University of Alberta,*
*Edmonton, Alberta,*
*Canada T6G 2E1*

Sébastien Balibar†

*Laboratoire de Physique de l'École normale supérieure,*
*ENS, Université PSL,*
*CNRS, Sorbonne Université,*
*Université Paris-Diderot,*
*Sorbonne Paris Cité, Paris,*
*France*

(Dated: July 20, 2020)

This article reviews experiments on elasticity, plasticity and flow of solid $^4$He and $^3$He, focusing on dislocations and other defects that are responsible for the unusual mechanical behavior of such quantum crystals. Helium's zero point motion prevents it from freezing unless pressure is applied, and makes the solid extremely compressible, with elastic constants orders of magnitude smaller than those of conventional solids. Tunneling allows defects to remain mobile at low temperatures so dislocations have much larger effects on mechanical properties than in conventional solids. At temperatures below 400 mK, dislocations in hcp $^4$He are essentially undamped and, in the absence of pinning by $^3$He impurities, glide freely in the basal plane. In this regime, dislocation motion reduces the shear modulus by as much as 90%, an effect that has been referred to as "giant plasticity" although it is reversible and so might be better described as "softening". In this low temperature regime, macroscopic plastic deformation occurs via sudden dislocation avalanches with a wide range of time and length scales. At higher temperatures, dislocation motion is damped, introducing dissipation in elastic measurements, and thermally activated defect motion makes helium crystals extremely ductile, flowing under millibar stresses near melting. During the last decade, most of the properties of the dislocations that are responsible for the elastic effects described in this review have been accurately measured: their orientation, density and length distributions, the nature of their networks, and their binding to isotopic impurities. Despite this detailed understanding of mobile dislocations, there remain open questions. Much less is known about defects' roles in the elastic and plastic behavior of hcp and bcc $^3$He crystals and even in hcp $^4$He, almost nothing is known about other types of dislocations that are immobile and so do not affect elastic properties. These might be responsible for recently observed superfluid-like mass flow in $^4$He at low temperatures, although it is now clear that the apparent mass decoupling seen in torsional oscillator experiments with solid $^4$He was due to the elastic effects described in this paper, not to supersolidity.

## CONTENTS



* jbeamish@ualberta.ca
† sebastien.balibar@lpa.ens.fr

## I. INTRODUCTION

Helium is a uniquely quantum material. The most dramatic manifestation of its quantum nature is superfluidity in liquid helium. Atoms of the common isotope, $^4$He, are bosons and condense into a superfluid state below the lambda temperature $T_\lambda$ =2.176 K. The rare isotope, $^3$He is a fermion and does not become superfluid until atoms pair at much lower temperatures, around 2 mK, to form complex superfluid phases. Quantum effects are usually less significant in solids. In classical crystals, at zero temperature atoms sit at lattice sites where the potential energy is minimized. Since they are localized, they can be regarded as distinguishable particles and quantum statistics are not important. In solid helium, quantum effects change this picture in two important ways. First, helium's small mass and weak interatomic potential means that atoms have large quantum zero point motion, rather than sitting motionless at lattice sites. Secondly, tunneling allows helium atoms to exchange, so their Bose or Fermi statistics remain relevant in this quantum solid.

The zero point energy due to localizing an atom within a lattice unit cell can be estimated by considering a point particle in a 3-dimensional box. Its ground state energy is $E_0 = 3h^2/8ma^2$, where $h$ is Planck's constant, $m$ is the particle's mass and $a$ is the size of the box, i.e. the lattice parameter. A more realistic estimate for atoms with a hard core diameter $d$ would be to use $(a - d)$ rather than $a$ as the distance over which atoms are confined. This quantum mechanical energy is largest for light atoms like helium and can be compared to the potential energy of the solid, set by the depth $\varepsilon$ of the interatomic potential well. The "quantumness" of a solid can then be characterized by the de Boer parameter $\Lambda$, whose square is essentially the ratio of the zero point energy to the potential energy:

$$\Lambda^2 = \frac{h^2}{ma^2\varepsilon}. \quad (1)$$

Even for a weakly interacting inert gas like argon, the zero point energy is a small correction to the classical potential energy, $\Lambda^2 \approx 0.03$. For solid $^4$He, with its light mass and even weaker interactions, $\Lambda^2 \approx 7$, so the quantum energy dominates. Neutron scattering measurements (Adams *et al.*, 2007) of solid $^4$He atoms' zero point kinetic energy give values around 25 K, substantially larger than the depth of the potential well for helium atoms, $\varepsilon \approx 11$ K. Quantum effects are even more important in solid $^3$He, which has the same potential but a smaller mass.

The solid, liquid and vapor phases of materials are often displayed in pressure-temperature (P-T) phase diagrams like those in Fig. 1. The left panel (a) shows the phase diagram for argon, a simple classical material with a spherically symmetric interatomic potential and a close-packed face centered cubic (fcc) crystal structure. The solid (red) coexistence line in Fig. 1 (a) is the vapor pressure curve, where the liquid and gas phases coexist (or, below the melting point, it is the sublimation curve where solid and gas phases coexist). The vapor pressure curve ends at a critical point, above which the argon is fluid but there is no distinction between liquid and gas states. The dashed (black) line separating the solid and fluid phases is the melting curve, which extends to high pressure with a positive slope (the melting temperature $T_m$ increases slightly with pressure, the normal behavior for materials where the solid phase is denser than the liquid). These lines meet at the triple point, a unique point in the phase diagram where all three phases can coexist. These phases and transitions are familiar from other materials, e.g. water, ice and steam. For water, the triple point occurs at a temperature $T_c$ of 273.16 K (which was used as a fixed point to define the kelvin scale temperature) and a pressure of 612 Pa. Water is, however, a complex material, with many different solid phases. It is also unusual in that its solid phase, ice, is less dense than liquid water, which results in a melting curve with a negative slope.

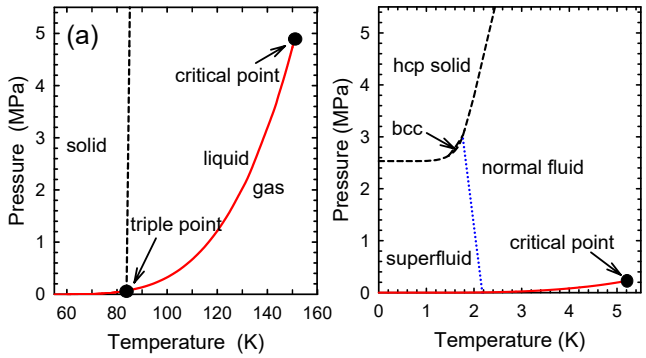


FIG. 1 Pressure-temperature (P-T) phase diagrams for (a) argon and (b) $^4$He. Melting curves are shown as dashed black lines, vapor pressure curves as solid red lines. $^4$He's superfluid transition (the "lambda line") is the dotted blue line.

The phase diagrams of nearly all materials share these features - coexistence lines between solid, liquid and gas phases that meet at a triple point. The exception is helium, for which quantum effects dominate in the liquid and solid phases. The right panel (b) of Fig. 1 shows the phase diagram of helium (for the common isotope $^4$He). In contrast to argon, and to all other materials,

there is no triple point at which solid, liquid and gas can coexist. Helium is the only liquid that does not freeze under its own vapor pressure, a consequence of its large zero point energy and its weak interatomic interactions. $^4$He can only be solidified by applying pressures greater than 2.53 MPa, with the melting curve shown as a dashed black line. At the lowest temperatures it crystallizes in the hexagonal close packed (hcp) structure, but there is a small region around 1.6 K where a body-centered cubic (bcc) phase, with a more open structure and lower zero point energy, is stable. Even higher pressures are required to solidify the lighter $^3$He isotope (3.44 MPa at zero temperature), and its bcc phase extends to low temperatures. The solid and gas phases never coexist in helium, so the vapor pressure curve (the solid red line) extends to zero temperature. The existence of a quantum liquid at arbitrarily low temperatures creates the possibility of superfluidity in the Bose isotope, $^4$He. The superfluid state appears below the dotted blue lambda line in Fig. 1 (b).

Helium's quantum nature affects its properties in the solid state. The density of low pressure helium crystals is less than half the value predicted for classical crystals with the same potential. Even at the lowest temperatures, helium atoms' zero point motion extends over a significant fraction of the unit cell (Arms *et al.*, 2003; Blackburn *et al.*, 2007), in contrast to classical crystals where thermal fluctuations are the only source of displacements away from lattice sites. Solid helium is also extremely compressible, with a bulk modulus less than a third of the value expected for a classical crystal and about five orders of magnitude smaller than that of a typical metal.

In addition to expanding the lattice and softening the crystal, helium's zero point motion allows atoms to exchange by tunneling. This exchange means that, in contrast to other materials, helium atoms' Bose or Fermi statistics remain important in the solid phase. In solid $^3$He, for example, atomic exchange leads to magnetic ordering of spins at temperatures around 1 mK. In both $^3$He and $^4$He, it allows isotopic impurities to move easily through the lattice, even at zero temperature. One intriguing possibility is that a quantum crystal could have a finite vacancy concentration at zero temperature, creating an "incommensurate solid" with perfect periodicity but fewer atoms than lattice sites. Delocalized "zero point vacancies" (ZPV) would contribute to mass flow and in $^4$He could even Bose condense to form a "supersolid" with coexisting positional and superfluid order. At present there is no clear evidence for zero point vacancies but even in their absence, exchange could still produce a supersolid in which translational symmetry breaking and superfluidity coexist.

As well as revealing uniquely quantum phenomena in solids, helium has advantages as a model system to study material properties of solids. For example, at low temperatures helium's latent heat of melting disappears, so melting and freezing become purely mechanical processes. This allows the liquid-solid interface to be studied in detail, in contrast to conventional crystals where the latent heat makes it difficult to achieve equilibrium. Many of its unusual properties have been experimentally studied, including its surface tension (Andreeva and Keshishev, 1991; Babkin *et al.*, 1995; Balibar *et al.*, 1979; Edwards *et al.*, 1990; Gallet *et al.*, 1984; Keshishev *et al.*, 1979; Rolley *et al.*, 1989, 1995b), roughening transitions (Alles *et al.*, 2001; Gallet *et al.*, 1984; Keshishev *et al.*, 1979; Landau *et al.*, 1980; Rolley *et al.*, 1986, 1989; Todoshchenko *et al.*, 2005; Tsepelin *et al.*, 2001; Wagner *et al.*, 1996; Wolf *et al.*, 1985), melting/freezing waves (Bodensohn *et al.*, 1986; Keshishev *et al.*, 1981; Rolley *et al.*, 1995b) and wetting behavior. Helium also provides unique opportunities to study fundamental properties of defects like impurities and dislocations, and their roles in elastic and plastic deformation (Balibar and Nozières, 1994; Balibar *et al.*, 2005). Helium crystals of extraordinary purity can be prepared since at low temperatures all but isotopic impurities freeze out, and these have low concentrations. $^3$He concentrations in commercial $^4$He gas are of order $10^{-7}$ and can be reduced to the $10^{-12}$ level using a superfluid heat flush technique, or to essentially zero by freezing at very low temperatures. High quality single crystals can be grown quickly and their density can be varied over a substantial range with moderate pressures. The complete temperature range is accessible, from essentially zero up to the melting temperature.

In this paper, we review the current state of understanding of defects in solid helium, particularly their effects on these quantum crystals' elastic and plastic properties. Many of the measurements we describe were inspired by Kim and Chan's 2004 claim of the discovery of supersolidity in torsional oscillator measurements (Kim and Chan, 2004a,b). These torsional oscillator effects are now understood as a manifestation of the unusual elastic behavior of solid $^4$He (Day and Beamish, 2007b; Haziot *et al.*, 2013c), rather than as mass decoupling of a supersolid (Beamish *et al.*, 2012; Maris, 2012; Maris and Balibar, 2011; Reppy *et al.*, 2012). However, interest in solid helium's quantum and mechanical properties began much earlier, and many experiments were spurred by predictions of supersolidity and of unusual quantum motion of diffusion of vacancies and impurities (Andreev and Lifshits, 1969; Chester, 1970; Leggett, 1970).

Helium was discovered spectroscopically in the sun in 1868 and subsequently found on earth as a product of uranium ore in 1895. It was first liquefied in 1908 but it was not until 1926 that $^4$He was frozen by applying pressures greater than 2.5 MPa (Keesom, 1926). The crystal structure (hcp) was determined by x-ray diffraction (Keesom and Taconis, 1938) in the same year that the superfluid nature of the He II phase of liquid $^4$He was discovered. The rare isotope, $^3$He, is a decay prod-

uct of tritium and became available as a byproduct of thermonuclear weapons programs (Osborne *et al.*, 1949). Osborne *et al.* (1951) solidified $^3$He in 1951 and its bcc and hcp structures were identified by Schuch *et al.* (1958). Phase separation of solid $^3$He-$^4$He mixtures at low temperatures was observed in 1962 (Edwards *et al.*, 1962).

Ultrasonic measurements on solid helium began with longitudinal waves in bcc $^3$He (Abel *et al.*, 1961) and in $^4$He (Vignos and Fairbank, 1961). The latter measurements led to the discovery of the bcc phase of $^4$He, which occupies a small region of its phase diagram. Shortly after, transverse ultrasound was propagated in hcp and bcc $^4$He (Lipschultz and Lee, 1965). During the first half of the 1970s, elastic constants were measured in oriented single crystals of hcp and bcc $^4$He (Greywall, 1971, 1976) and of bcc $^3$He (Greywall, 1975). The temperature dependences of sound speeds were measured soon after (Wanner *et al.*, 1973; Wanner and Mueller Jr, 1974). In 1976, dislocations were identified as the source of low temperature anomalies in ultrasonic velocities (Wanner *et al.*, 1976). Between 1979 and 1983, more complete measurements of the ultrasonic velocity and attenuation were made in hcp $^4$He (Iwasa *et al.*, 1979; Iwasa and Suzuki, 1980) and in bcc and hcp $^3$He (Beamish and Franck, 1982, 1983; Iwasa and Suzuki, 1982). These provided new information about the mobility and pinning of dislocations in solid helium. During the same period, there were a number of plastic deformation experiments on helium, revealing "metallurgical" phenomena like yield drops (Suzuki, 1973, 1977) and plastic flow, at stresses much lower than in conventional crystals (Sanders *et al.*, 1977, 1978).

The study of defects in helium was less active during the 1980s and 1990s, but work included direct x-ray diffraction measurements of vacancy energies and concentrations (Fraass *et al.*, 1989; Heald *et al.*, 1984; Simmons, 1994) and x-ray topography experiments that directly imaged dislocation arrays associated with low angle grain boundaries (Iwasa *et al.*, 1995). The liquid-solid surface tension and wetting behavior of helium were thoroughly studied (Balibar and Castaing, 1985; Balibar *et al.*, 1979). The non-wetting of many substrates by solid helium was shown to suppress freezing in porous materials which, for example, raised the freezing pressure in the nanoscale pores of Vycor glass by more than 1 MPa (Adams *et al.*, 1987; Beamish *et al.*, 1983; Molz and Beamish, 1995).

In 2004, interest in solid $^4$He was reinvigorated by the apparent discovery of supersolid helium, based on torsional oscillator (TO) measurements. The TO frequency increased below 200 mK, which was interpreted as evidence of a supersolid mass fraction decoupling from the oscillator, in analogy to the classic Andronikashvili experiment that measured the superfluid fraction of liquid $^4$He (Andronikashivili, 1946). The frequency shifts for solid $^4$He were suppressed at high oscillation amplitudes, which was taken as evidence of a superfluid-like critical velocity. Other features of the TO data were unexplained, but suggested defects were important. The transition was rounded, rather than sharp, and was accompanied by a dissipation peak. The amount of decoupling varied by orders of magnitude in different experiments and usually decreased when samples were annealed. The transition temperature was extremely sensitive to $^3$He impurities, decreasing by a factor of more than 2 when the impurity concentration $x_3$ was reduced from $3\times10^{-7}$ to $10^{-9}$.

In 2007, low frequency measurements of polycrystalline $^4$He's shear modulus $\mu$ showed very similar behavior (Day and Beamish, 2007b). The shear modulus increased below 200 mK, with the same dependence on temperature, $^3$He concentration and amplitude as the TO frequency change. However, the shear modulus behavior had a natural explanation in terms of mobile dislocations, which softened the crystal at high temperature but were pinned by $^3$He impurities low temperature. The amplitude dependence was explained as stress-induced breakaway from the weak $^3$He pinning centers. It was clear that the torsional oscillator and shear modulus behaviors were closely related, but difficult to understand how the shear modulus changes would affect different torsional oscillators. In 2012, several papers addressed this question and it became clear that the stiffening of torsional oscillators, due to shear modulus changes in solid helium in the torsion rod (Beamish *et al.*, 2012) or in other parts of the oscillator (Maris, 2012; Reppy *et al.*, 2012), was sufficient to explain the observed TO frequency shifts. Since then, a number of the original TO experiments have been repeated in rigid oscillators designed to minimize the effects of the solid helium's shear modulus. The frequency shifts were essentially eliminated (Choi *et al.*, 2015; Kim and Chan, 2012), confirming that they were due to elastic changes in the helium, not signatures of mass decoupling in a supersolid.

However, the shear modulus changes themselves were dramatic and unexpected. Further measurements on single crystals showed that mobile dislocations could reduce the shear modulus of hcp $^4$He's by as much as 90%, orders of magnitude larger than dislocation effects in conventional materials (Alers and Zimmerman, 1965; Bauer and Gordon, 1962; Thompson and Holmes, 1959). This effect was described as "giant plasticity". These experiments identified the mechanism in hcp $^4$He as basal glide (Haziot *et al.*, 2013c), confirmed that thermal phonon scattering was the source of dislocation damping (Haziot *et al.*, 2013a), identified a critical dislocation velocity related to the propagation velocity of $^3$He impurities (Haziot *et al.*, 2013b), and extracted the dislocation density and length distribution in $^4$He crystals (Fefferman *et al.*, 2014). Measurements in polycrystalline hcp $^3$He identified an additional dislocation damping mechanism associated with the $^3$He spins (Cheng and Beamish,

2017). The effects of dislocations on the elastic behavior of these quantum solids are now well-established.

Dislocations are also central to plasticity. Early plastic deformation experiments (Sanders *et al.*, 1977, 1978; Suzuki, 1973, 1977) were done at high temperatures, where thermal processes like vacancy diffusion control the flow behavior. Recent measurements (Cheng and Beamish, 2018b) at much lower temperatures showed a crossover, from thermally activated creep above 400 mK to sudden dislocation avalanches and acoustic emission at lower temperatures.

Other experiments have studied mass flow in response to pressure gradients across solid helium. At high temperatures, flow can occur via motion of vacancies or dislocations (Day and Beamish, 2007a; Lisunov *et al.*, 2014, 2015; Suhel and Beamish, 2011). This defect motion is thermally activated, so flow rates decrease rapidly at low temperatures. Inspired by the search for supersolidity, a number of experiments (Bonfait *et al.*, 1989; Day and Beamish, 2006; Greywall, 1977b) looked unsuccessfully for evidence of superflow in hcp $^4$He at low temperatures. More recently, however, a group of experiments revealed non-thermal flow that began around 0.6 K and extended to temperatures below 100 mK (Cheng and Beamish, 2016; Hallock, 2019; Ray and Hallock, 2008; Shin *et al.*, 2017; Vekhov *et al.*, 2014). This may be an example of superflow associated with dislocations, but the flow channels have not been unambiguously identified and some aspects of the experiments are not yet understood.

Our theoretical understanding of quantum solids has also developed in recent decades. Classical calculations, which worked well for heavy inert gas crystals (Beamish, 2001), greatly overestimated the values of solid helium's density, binding energy and bulk modulus. In fact, the helium atoms sit at local maxima of the interatomic potential, where classical lattice dynamics predicts imaginary phonon frequencies. Early theories of solid helium (Glyde, 1976; Klein and Horton, 1972; Werthamer, 1969) incorporated quantum zero point motion but also had to recognize the correlations between atoms' positions due to their hard core repulsion, leading to effective potentials with renormalized force constants and sound speeds. Phonon dispersion curves were calculated and the normal, albeit slow, propagation of sound waves in solid helium was understood. Around the same time, it was realized that quantum exchange of atoms via tunneling would have dramatic effects on point defects like vacancies and impurities, allowing them to propagate through a helium crystal, even at low temperatures (Andreev and Lifshits, 1969; Andreev, 1976). Exchange was also recognized as crucial to magnetic order in solid $^3$He at mK temperatures.

The development of path integral Monte Carlo (PIMC) techniques, combined with advances in computational power, made it possible to do fully quantum mechanical, first principles simulations for condensed helium using accurate interatomic potentials (Ceperley, 1995). These directly confirmed the importance and consequences of quantum zero point motion and exchange in liquid and solid helium. Early PIMC work included computing the Bose condensate and superfluid fractions, and the transition temperature in liquid $^4$He (Ceperley and Pollock, 1986; Pollock and Ceperley, 1987). For solid helium, the atomic exchange constants for bcc $^3$He were determined (Ceperley and Jacucci, 1987), giving nearest neighbour exchange frequencies of order 10 MHz and confirming that next nearest neighbor and multiple exchanges are also important. The calculated exchange frequencies for hcp $^4$He were much smaller (Bernu and Ceperley, 2005), of order 100 kHz near the melting density. This is still significant but, given $^4$He's lack of spin, there is no direct experimental confirmation of the values. More recent PIMC simulations involved defects in solid helium, including studies of vacancies and interstitials in hcp $^4$He (Boninsegni *et al.*, 2006a; Clark and Ceperley, 2008). Following the development of a new PIMC "worm" algorithm (Boninsegni *et al.*, 2006b), simulations have been expanded to larger particle numbers, allowing extended defects like grain boundaries (Pollet *et al.*, 2007) and dislocations (Boninsegni *et al.*, 2007) to be studied.

The properties of helium, including its solid phases, were comprehensively reviewed in the late 1960s in monographs by Wilks (1967) and by Keller (1969). A more recent overview of $^3$He is available in a recent book by Dobbs (2000). Other reviews have focused on specific aspects of solid helium. These include theoretical and experimental aspects of exchange and the diffusion of defects (Andreev, 1982; Grigor'ev, 1997; Guyer *et al.*, 1971), vacancies in $^4$He (Burns and Goodkind, 1994), the surface of helium crystals (Balibar *et al.*, 2005), and magnetic phases in $^3$He (Adams, 2004; Bennemann and Ketterson, 1976; Osheroff, 1992). Two recent papers discussed aspects of plasticity (Beamish, 2019) and superflow (Hallock, 2019) in solid helium. This review will focus on the mechanical properties of solid helium, which have not been comprehensively described since the 1972 review by Trickey *et al.* (1972), written at a time when ultrasonic measurements were just beginning and the effects of defects on helium's elastic and plastic behavior had not been explored.

## II. STRUCTURE, PHASE DIAGRAMS AND CRYSTAL GROWTH

The phase diagrams of $^4$He and $^3$He include multiple crystal structures at easily accessible pressures, and high quality single crystals can be rapidly grown at low temperatures. This provides unique opportunities to study defects, and to distinguish between quantum and structural effects on their behavior. However, as for other materials, the quality of helium crystals depends on their

preparation.

### A. Phase diagrams

Helium does not freeze under its own vapor pressure so its phase diagram has no triple point and the solid never coexists with low density gas. At zero temperature, a pressure of about 2.53 MPa (25.3 bar) is required to freeze $^4$He. For $^3$He, with its larger zero point motion, the minimum freezing pressure is 2.93 MPa (29.3 bar) at 315 mK, and an even higher pressure, 3.44 MPa, is needed at zero temperature. The melting pressures increase at higher temperatures. For example, at 2 K the melting curve pressures are about 38 bar for $^4$He and 77 bar for $^3$He. Figure 2 shows the pressure vs. temperature (P-T) phase diagrams for $^4$He (Grilly, 1973; Grilly and Mills, 1962; Hoffer *et al.*, 1976; Straty and Adams, 1966a; Vignos and Fairbank, 1961) and $^3$He (Grilly, 1971; Straty and Adams, 1966b), at temperatures up to 4.2 K and pressures to 20 MPa (200 bar). For both isotopes, there are stable bcc and hcp phases. The bcc region is very small for $^4$He (inset) and at zero temperature solid $^4$He is in the close-packed hcp phase. The larger zero point motion of $^3$He favors the more open bcc phase, which occupies a much larger region extending down to zero temperature. Not shown in Fig. 2 are the close-packed face-centered cubic (fcc) phases found in both $^4$He and $^3$He at much higher pressures and temperatures (above 100 MPa and 15 K).

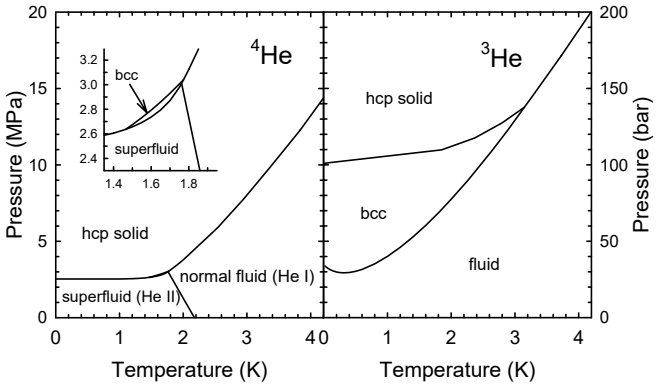


FIG. 2 Pressure-temperature (P-T) phase diagrams for $^4$He (left panel) and $^3$He (right panel). The inset is an enlargement of the bcc region for $^4$He. The pressure scales are the same for $^3$He and $^4$He, but are labeled in MPa (on the left axis) and bar (on the right axis).

Figures 3 and 4 show the low pressure regions of the phase diagrams for $^4$He and $^3$He, respectively. The P-T diagrams (upper panels of the figures) show the melting curves separating liquid and solid, as well as the hcp-bcc coexistence line and the lambda line separating the normal (He I) and superfluid (He II) phases of $^4$He. The lower panels show the corresponding molar volume vs. temperature (V-T) diagrams, with the different phases and their coexistence regions.

The large compressibility of solid helium means that measurements are usually made at constant volume and density, since the pressure cells in which the solid is grown are much more rigid than the helium. It also means that helium can be frozen at constant mole number, since increasing the pressure by about 20 bar compresses the liquid to solid densities. If a cell containing high density liquid is cooled without adding or removing helium, e.g. by blocking the fill capillary, the liquid begins to freeze when the temperature reaches the melting curve. It then follows the melting curve until all the helium is frozen at a lower pressure. The solid then cools at nearly constant pressure. Examples of such "blocked capillary" freezing paths are shown as horizontal (constant volume) dashed red lines in the lower V-T diagrams of Figs. 3 and 4. The upper panels show the corresponding P-T paths. Depending on the starting density, the system may pass through several phases and coexistence regions during cooling. For example, for a starting pressure of 5.1 MPa, the molar volume of liquid $^4$He is 20.9 cm$^3$. At this density, the liquid would begin to freeze into the hcp phase around 2.35 K. Upon cooling, the liquid-hcp mixture would transfom to a hcp-bcc mixture at the upper triple point of the bcc phase (1.772 K) and then follow the hcp-bcc coexistence curve until the bcc phase disappears around 1.50 K. The hcp solid would then cool at a nearly constant pressure of about 2.7 MPa. Samples at higher densities would go directly from liquid to hcp, for example the freezing path for a molar volume of 20.5 cm$^3$, shown as a dashed red curve in Fig. 3. At low densities (molar volumes larger than 21.0 cm$^3$, corresponding to starting pressures below 49 bar) the $^4$He remains partially liquid at low temperatures, and the solid portion transforms from hcp to bcc and then back to hcp again.

Helium crystals can also be grown at constant pressure, by keeping the fill capillary open and adding helium as the liquid freezes. This corresponds to vertical paths in the V-T diagrams of Figs. 3 and 4. This method avoids hcp-bcc crystallographic transformations and the crystals experience much smaller stresses than during blocked capillary growth, where there are large pressure and temperature changes.

The minimum in the $^3$He melting curve shown in Fig. 4 ($P_{min}$ = 2.931 MPa at $T_{min}$ = 315 mK) is due to $^3$He's spin. Below 315 mK, the spin entropy of the solid is larger than the total entropy of the liquid. This unusual situation means that the slope of the melting curve is negative below 315 mK and low density $^3$He crystals partially remelt when cooled at constant volume, as indicated by the dashed red lines in Fig. 4 which show a blocked capillary path at a molar volume of 24.6 cm$^3$.

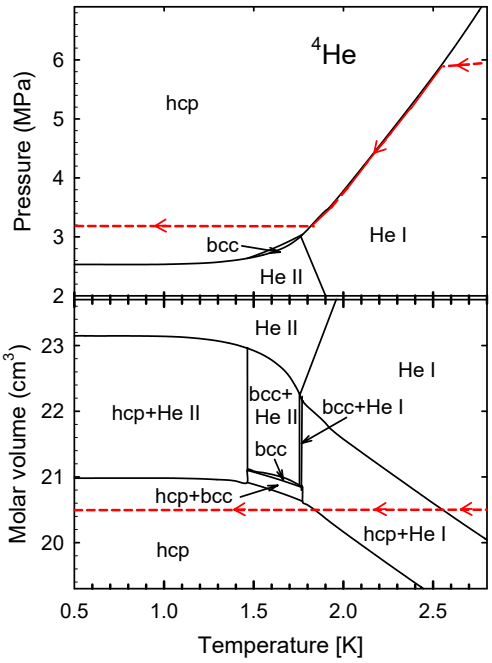


FIG. 3 P-T (upper panel) and P-V (lower panel) phase diagrams for $^4$He. The dashed red lines and arrows indicate the path followed during blocked capillary freezing at molar volume of 20.5 cm$^3$.

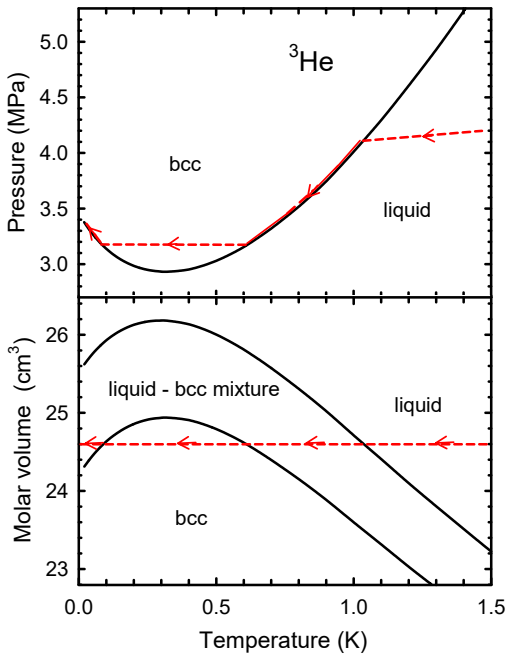


FIG. 4 P-T (upper panel) and P-V (lower panel) phase diagrams for $^3$He. The dashed red lines and arrows indicate the path followed during blocked capillary freezing at a molar volume of 24.6 cm$^3$.

### B. Crystal growth and quality

Since the discovery of solid $^4$He by W.H. Keesom (1926), helium has been solidified using different methods which produce either polycrystals or single crystals. The orientations of single crystals can be determined using diffraction or optical techniques. Keesom and Taconis (1938) were the first to apply x-ray diffraction to helium, using Laue diffraction to determine the crystal structure of hcp $^4$He. As discussed by Greywall (1971), this technique has been used to find the orientation of crystals in some experiments, while other authors have used inelastic neutron scattering. Optical birefringence can also be used to orient hcp helium crystals, as shown by Heybey and Lee (1967). The facets that are visible during crystal growth provide a more general way to orient crystals, if optical access if available.

For their study of sound propagation in hcp $^4$He crystals, Crepeau *et al.* (1971) grew single crystals by filling a cell that was kept at constant temperature $T$. They observed that below 1.45 K this led to single crystals whose crystal orientations they determined using optical birefringence. For his ultrasonic measurements of elastic constants, Greywall (1971) used a constant pressure growth method, which had been introduced by Shal'nikov (1962) and improved by Mezhov-Deglin (1966). Freezing slowly in a temperature gradient allowed him to grow single crystals at various pressures $P$, whose orientations were determined using Laue x-ray diffraction.

The blocked capillary method used to grow helium crystals at constant volume has been shown by Sasaki and Balibar (2008) to produce polycrystals because many different crystallites nucleate on favorable sites on the cell walls. Growing crystals from the superfluid liquid at constant temperature, on the other hand, usually produces a single crystal, or a few large crystals, at or close to the liquid-solid equilibrium pressure. When grown below ∼1 K, the crystals have facets with edges that can be easily analysed to determine the crystal orientation (Haziot *et al.*, 2013c; Sasaki and Balibar, 2008).

#### 1. Polycrystals

For low temperature measurements, the experimental cell is usually attached to the lowest temperature stage of a dilution refrigerator and the solid helium has to be grown from the liquid phase inside a closed cell. For blocked capillary growth, the first step is to admit helium through a thin capillary until the cell is filled with normal liquid $^4$He at high pressure (greater than about 4.8 MPa). This is typically done at ∼3 K, to ensure that the helium is liquid everywhere along the fill line. In order to cool down, one usually starts by pumping on the refrigerator's $^4$He pot, which rapidly cools to about 1 K. Since the fill capillary is thermally anchored to this "1 K pot", a plug

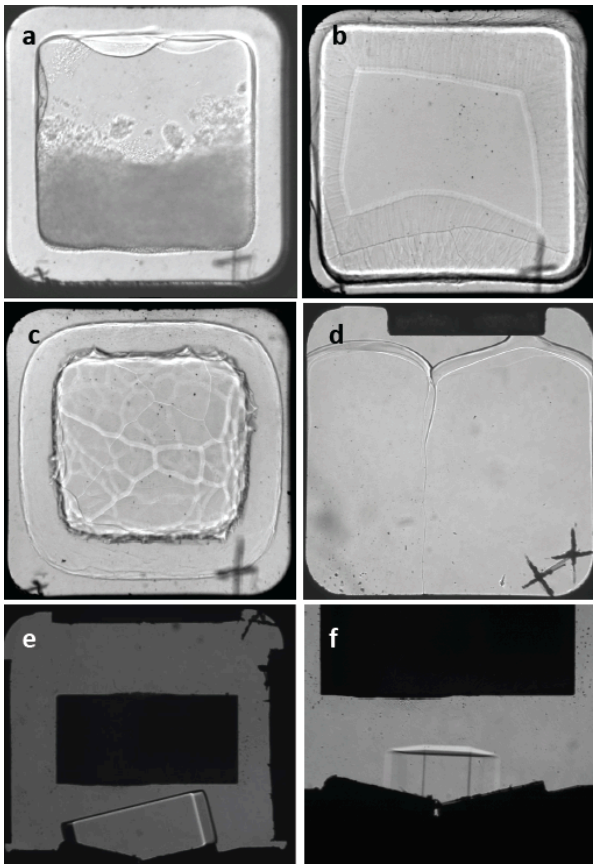


FIG. 5 Images of $^4$He crystals, obtained in a transparent cell by Sasaki and Balibar (2008) when using different growth methods. Crosses visible in the lower right corner of the images were carved on the windows to help adjust the focusing.

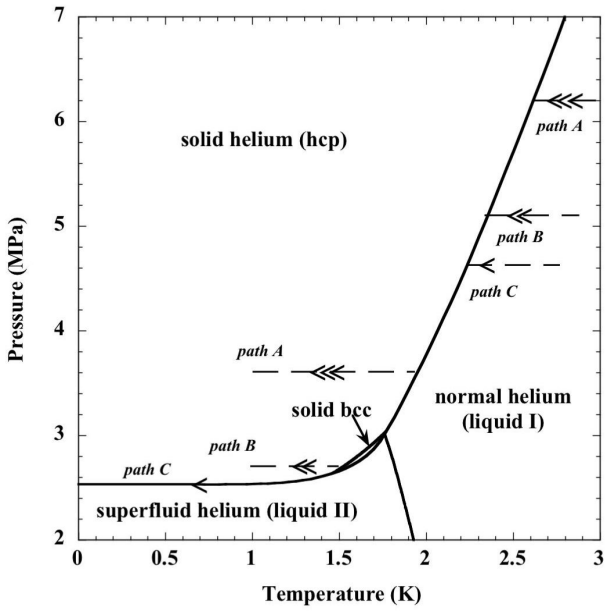


FIG. 6 Paths followed when $^4$He is solidified using the "blocked capillary method". The paths shown correspond to isochores for different starting pressures: Path A (starting pressure 6.2 MPa), Path B (5.1 MPa) and Path C (4.63 MPa).

of solid helium quickly forms there, isolating the mass of helium inside the cell from the external helium supply. Assuming that this plug does not move and blocks all flow of helium, the amount of helium in the cell is essentially constant when the cell is cooled and the helium freezes. If the fill line volume is negligible compared to the cell volume, freezing occurs along an isochore that first meets the melting curve at a temperature $T_i$ and leaves it when the helium is completely frozen at a lower temperature $T_f$.

Figure 5 shows examples of optical images of $^4$He crystals obtained by Sasaki and Balibar (2008) for various growth methods. The crystals were grown in an optical cell between two transparent glass windows closing a 11×11 mm hole through the body of the cell (3 to 10 mm thickness). The windows were sealed with indium O-rings. The crystal shapes and the quality of the solid samples depended on the growth method. For example, panel (a) of Fig. 5 shows the result of rapid pressurization (over a time 140 ms in this example) of normal liquid helium (here at 1.8 K). This produced irregular "snowflakes" and a highly disordered solid.

Figure 6 shows blocked capillary growth paths on the P-T diagram of $^4$He. The images in panels (b) and (c) of Fig. 5 correspond to slow crystallization (typically over 3 hours) for path B of Fig. 6, starting with liquid at 5.1 MPa. When the cell reached 2.36 K, freezing began on the walls, which were colder than the center of the cell, producing the disordered hcp crystal visible in panel (b). The network of lines in the center part of the image corresponds to defects in a thin solid layer covering the front and back windows. At 1.77 K, the upper triple point of the bcc-hcp transition, the bcc phase appeared between the hcp solid on the walls and the liquid in the center of the cell, as shown in panel (c). Here again the network of lines in the central part corresponds to grain boundaries in a thin layer covering the glass windows. Upon further cooling, the bcc region expanded and the liquid region shrank. The last liquid disappeared at 1.66 K. The bcc region in the center then shrank and disappeared completely by 1.59 K, leaving only hcp solid. Note that this behavior differs slightly from that expected based on $^4$He's V-T phase diagram (the lower panel of Fig. 3). The initial pressure (5.1 MPa) corresponds to a liquid molar volume of 20.9 cm$^3$. At this density, all of the liquid should freeze at a fixed temperature of 1.772 K, since the three phases (liquid, bcc and hcp) can only coexist at a triple point. Their coexistence over a range of temperatures (between 1.77 and 1.66 K) indicates that there are temperature and/or pressure gradients in the cell during blocked capillary growth.

Solidification along the A or C isochores led to similar images. The highest pressure sample (path A) started

with liquid at 6.2 MPa and began freezing at $T_i$ =2.58 K. Freezing was complete at $T_f$ ≈1.95 K, at a pressure around 3.6 MPa in the hcp phase. According to Fig. 3, there should still have been some liquid in the cell at 1.95 K, suggesting that additional helium entered the cell, despite the solid plug in the capillary. The lowest pressure sample (path C) started at a pressure of 4.63 MPa and freezing into the hcp phase began at $T_i$ =2.19 K. As the sample cooled along the melting curve, some hcp solid converted to bcc near the triple point but the three phases again appeared together until the hcp phase disappeared at 1.70 K. On further cooling, the remaining liquid froze, leaving only bcc solid by 1.56 K. At 1.46 K, the lower bcc-hcp triple point, the bcc solid suddenly converted to the denser hcp phase, and some liquid reappeared. The liquid region shrank during futher cooling along the melting curve but some remained even at 35 mK.

In all three cases, solidification began from the normal liquid and, in the absence of a controlled thermal gradient, it was very difficult to obtain good quality single crystals. For paths A and B, the phase transitions between the hcp and bcc phases introduced additional stresses and disorder. To grow high quality single crystals such as those shown in panels (d), (e) and (f), a different growth method is required.

### 2. Single crystals

By pressurizing liquid $^4$He at constant temperature in the superfluid phase, one can obtain single crystals (Pantalei *et al.*, 2010). This can be done by slowly injecting helium from an external source into a cell at a regulated temperature. The pressure in the cell rises until it reaches the crystallization pressure, where it remains until the cell is full of solid and the fill line spontaneously blocks. It is surprising that this can be done even at temperatures below 0.775 K, where there is a shallow minimum in the $^4$He melting curve (Grilly, 1973; Straty and Adams, 1966a). One would expect the helium to crystallize in the fill line at that temperature, preventing more liquid from reaching the cell. However, helium remains in a metastable liquid state, only crystallizing at pressures about 10 mbar above the liquid-solid equilibrium curve (Balibar *et al.*, 1980, 2000; Grilly, 1973; Pantalei *et al.*, 2010; Ruutu *et al.*, 1996; Tsymbalenko, 1992), so that crystallization begins in the cell, not in the fill line. If the capillary is large enough and the helium is injected sufficiently slowly, typically over a few hours, the pressure in the fill line does not increase enough to nucleate solid and it remains open until the helium in the cell is frozen.

Using this method, one usually obtains a single crystal in equilibrium with the superfluid liquid (Balibar *et al.*, 2005). More than one crystal may nucleate on different favorable defects of the cell walls but the largest crystal grows at the expense of the smaller ones due to the smaller curvature of its liquid-solid interface. Because the temperature inside a superfluid is homogeneous, gravity is relevant and when this single crystal grows to a size larger than the capillary length $l_c \approx 1$ mm, it usually falls to the bottom of the cell. This fall may damage the crystal quality but it can be melted down to a much smaller size and the crystal can then be regrown from the small seed crystal at the bottom of the cell. By regrowing the crystal slowly, the cell can be filled with a large high quality single crystal like those shown in panels (e) and (f) of Fig. 5. This procedure is only possible if the cell has optical access so the crystal size can be controlled. Furthermore, the moving liquid-solid interface has a tendency to stick to defects on the walls, especially at points where a facet touches the wall. In this case, crystal growth proceeds by successive jumps, which creates defects.

Ruutu *et al.* (1998) were able to grow free standing single crystals with no screw dislocations. Their study showed the importance of screw dislocations in crystal growth, with drastic differences between the growth rates of faceted crystals with or without emerging screw dislocations. In an attempt to grow perfect crystals, Souris *et al.* (2015) grew crystals very slowly in a carefully machined and polished cell with a completely open geometry. However, even at growth velocities as low as 270 nm/s, they found it impossible to grow crystals with fewer than $10^4$ dislocations per cm$^2$. Their crystals, as well as those studied by Haziot *et al.* (2013a) and by Fefferman *et al.* (2014), typically had dislocation densities of order $10^5$ to $10^6$ per cm$^2$. However, those dislocation densities were determined from elastic measurements that are only sensitive to the samples' mobile edge dislocations, not screw dislocations like those measured by Ruutu *et al.* (1998).

For many types of experiment it is important to realize that liquid regions can remain, even when a cell appears to be full of solid. A grain boundary can create a liquid channel, with a triangular cross section where it meets a wall. These are sometimes visible, as in panel (d) of Fig. 5 (Sasaki *et al.*, 2008), and provide channels for superfluid flow. The size of such channels decreases with increasing pressure, but some liquid remains as long as the pressure is within about 10 bar of the liquid-solid equilibrium pressure $P_{eq}$. Liquid channels have also been seen at grain boundaries in high pressure fcc $^4$He crystals growing on sapphire windows (Franck *et al.*, 1983). The image in panel (d) of Fig. 5 also shows that the solid phase does not wet the cell walls. The contact angle of the liquid-solid interface, which is near 135 degrees, depends on the wall material and shows hysteresis, as usual for rough walls (Sasaki *et al.*, 2008). A consequence of this non-wetting is that the solid phase does not enter corners nor fill narrow cavities or sharp grooves in the

cell walls unless the pressure is significantly higher than $P_{eq}$. It can also allow a liquid layer to form between a helium crystal and the cell wall (Dash and Wettlaufer, 2005) at low pressures.

The procedure described above produces nearly random crystal orientations but it would be useful for many experiments if the orientation could be controlled. Two methods have been used to obtain oriented single crystals of helium. Both work if the temperature is low enough for the crystals to be facetted during growth (Balibar *et al.*, 2005). When a faceted crystal falls to the bottom of a cell, it often has a flat shape, like a coin whose faces are perpendicular to the c-axis of the crystal structure. In that case, it often lands on a c-facet, i.e. on a hexagonal plane of the crystal. By trying this procedure a few times, one can obtain a crystal with its 6 fold-symmetry axis (c-axis) vertical, as was done by Rolley *et al.* (1994b) for their study of the properties of stepped surfaces of helium crystals. In order to nucleate and force the first seed to fall down freely to the bottom of the cell, they used a local electric field on top, a method that had been used by Keshishev *et al.* (1979) and by Tsymbalenko (1995).

One can also grow oriented helium crystals by epitaxy on a graphite surface (Balibar *et al.*, 1980; Eckstein *et al.*, 1980; Ramesh *et al.*, 1984; Sasaki and Balibar, 2008). This can work if the graphite surface has been sufficiently well cleaned (Sasaki and Balibar, 2008), but it is not always successful. Panel (e) of Fig. 5 shows a faceted helium crystal that nucleated on the right side of the V-shaped graphite piece at the bottom of the cell, and is consequently oriented parallel to it. Panel (f), however, shows a crystal that nucleated somewhere else in the same cell and when it fell down, it was misoriented with respect to the graphite.

Even if crystal orientations cannot be controlled, direct optical observation of growth shapes allows the orientation to be determined rather easily. For refrigerators with optical access through sets of windows, temperatures are limited to about 10 mK due to the absorption of light and RF radiation from the outer world. To image crystals in the sub-millikelvin range, groups in Leiden (Wagner *et al.*, 1996) and in Helsinki (Manninen *et al.*, 1992) have used CCD cameras working at 65 K inside the refrigerator.

### 3. $^3$He crystals

As with $^4$He, it is possible to freeze $^3$He using the blocked capillary method. However, the deep minimum in the $^3$He melting curve at $T_{min} = 315$ mK means that low density $^3$He crystals partially remelt when cooled at constant volume, as indicated by the dashed red lines in Fig. 4 for a molar volume of 24.6 cm$^3$. To ensure that $^3$He is completely frozen at low temperatures, initial liquid pressures greater than about 4.5 MPa are required when using this technique. Growing $^3$He crystals directly into the high pressure hcp phase (not shown in Fig. 4) requires starting pressures above 18 MPa.

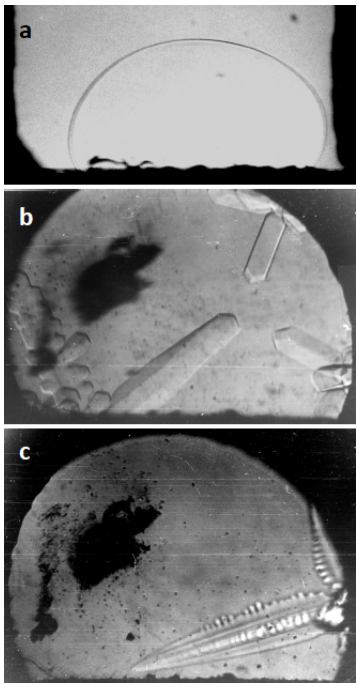


FIG. 7 $^3$He crystal shapes obtained by Rolley *et al.* (1986, 1994a). Panel (a): equilibrium shape at $T = 320$ mK. Panel (b): (110) facets on a growth shape of a bcc $^3$He crystal at 70 mK. Panel (c): dendritic growth obtained with high growth rates (30 $\mu$m/s) at 100 mK.

The minimum in the melting curve also means that it is not possible to grow single crystals of $^3$He by injecting mass through a fill line, since the fill line will block near $T_{min}$. Instead, one has to use a cell with a deformable membrane so that the liquid can be compressed. Using this method, Rolley *et al.* (1986) grew $^3$He crystals at temperatures as low as 60 mK. Figure 7 shows images of these crystals coexisting with liquid $^3$He. Panel (a) shows a crystal at the minimum of the melting curve minimum, $T = 0.32$ K. This is above the roughening transitions in $^3$He and the rounded equilibrium shape, due to gravity and surface tension, was analyzed by Rolley et al. to measure the surface tension of $^3$He or, more precisely, the liquid-solid interfacial tension (Rolley *et al.*, 1989). During slow crystal growth at 70 mK, they also observed (110) facets of these crystals, shown in panel (b). At much lower temperature, additional facets were discovered by Wagner *et al.* (1996), by Alles *et al.* (2001) and by Tsepelin *et al.* (2002).

## III. DEFECTS IN SOLID HELIUM

Some defects in solids can exist in thermal equilibrium; others are produced during crystal growth or

by subsequent deformation. They can be classified as point defects (vacancies, interstitials and impurities), 1-dimensional defects (dislocations), or two dimensional defects (grain boundaries and stacking faults). As in other materials, these defects affect many of the crystals' properties. In particular, dislocations and their interactions with other defects dominate the mechanical behavior of crystals. Quantum effects in helium crystals can make defects highly mobile at low temperatures, which results in unique behavior.

### A. Vacancies

Creating a vacancy corresponds to moving an atom from an interior lattice site to the crystal's surface. This increases the energy, entropy and volume (or the pressure, in the case of solid helium where the solid is held at constant volume). The equilibrium vacancy concentration at temperature $T$ and pressure $P$ is

$$x_v(T) = e^{(\frac{s_v}{k_B})} e^{-(\frac{E_v + P v_v}{k_B T})}. \quad (2)$$

where $E_v$, $v_v$ and $s_v$ are the vacancy formation energy, volume and non-configurational entropy. The vacancy concentration increases with temperature and decreases under pressure. Since a crystal lattice is not perfectly rigid, neighboring atoms relax inward when an atom is removed and the vacancy formation volume $v_v$ is smaller than the atomic volume $v_a$ in a perfect crystal, typically $v_v \approx 0.5 - 0.7 v_a$ (Cai and Nix, 2016). In classical crystals, the formation energy, which reflects the energy of broken bonds with atoms adjacent to a vacancy, can be roughly estimated from the solid-liquid interfacial energy $\sigma_{LS}$ (Andreeva *et al.*, 1989; Balibar and Castaing, 1985; Edwards *et al.*, 1991; Keshishev and Andreeva, 1991) and the surface area of the removed atom. The formation entropy, which is separate from the configurational entropy of the vacancy, is associated with local changes in vibrational frequencies and is of order $k_B$.

The most direct way to determine the vacancy formation energy is to measure the temperature dependence of $x_v$, by comparing changes in the density of lattice sites (measured by x-ray diffraction) to changes in the density of atoms (from thermal expansion measurements). In the case of helium crystals confined in a rigid cell, the number of atoms and total volume are fixed, so the vacancy formation energy and entropy can be determined from the temperature dependence of the lattice parameters. The lattice parameter changes are substantial, since vacancy concentrations in solid helium are as large as ∼0.3% near melting. Such x-ray measurements have been made for the bcc and hcp phases of both $^3$He and $^4$He (Fraass *et al.*, 1989; Granfors *et al.*, 1987; Heald *et al.*, 1983, 1984; Simmons, 1994). Formation energies in $^3$He varied from 2.3 K for the bcc phase at low density (molar volume $V_m$=24.86 cm$^3$, pressure P=2.98 MPa) to 21.4 K in the hcp phase at $V_m$=18.8 cm$^3$ (P=13.8 MPa). For $^4$He, measurements were made over a narrower density range, with comparable formation energies, e.g. 9.6 K in the hcp phase at $V_m$= 20.68 cm$^3$ (P=3.14 MPa). The bcc phase of $^4$He exists only over a narrow temperature range so the formation energy (∼9 K) is less precise.

Vacancy formation energies can also be extracted from their effects on properties like the pressure or heat capacity, but this requires that the contributions of phonons or other thermal excitations are accurately known. An analysis of heat capacity data in bcc $^3$He (Greywall, 1977c) gave vacancy energies similar to x-ray values. Surprisingly, there is no clear evidence of a similar vacancy contribution to the specific heat of hcp $^4$He, although it should be substantial (Gardner *et al.*, 1973), perhaps reflecting a wide vacancy bandwidth with a small density of states at low energies (Fraass *et al.*, 1989).

The motion of vacancies also contributes to diffusion in helium crystals, dominating at high temperatures. NMR can be used to probe the motion of atoms with spin and has been extensively used to study diffusion of $^3$He in helium crystals (Allen *et al.*, 1982; Grigor'ev, 1997; Kim *et al.*, 2013). In solid $^3$He, self-diffusion activation energies have been measured with NMR. They agree quite well with the direct x-ray values for vacancies in bcc $^3$He, but are significantly larger in hcp $^3$He (Heald *et al.*, 1984). The activation energy for vacancy diffusion can be larger than for formation if vacancies have to overcome an energy barrier in order to move. The agreement between the two energies for bcc $^3$He suggests that vacancies move by tunneling. The higher diffusion activation energy in hcp $^3$He indicates that tunneling is less effective and diffusion is largely due to classical activation over an energy barrier of about 12 K.

Since $^4$He atoms do not have spin, NMR cannot be used to study self-diffusion in solid $^4$He, but it can be used to study the diffusion of $^3$He impurities in $^4$He crystals. At high temperatures, the diffusion is thermally activated with activation energies similar to vacancy formation energies from x-ray measurements, although there is large scatter between activation energies from different NMR measurements (Fraass *et al.*, 1989).

Motion of vacancies can also be studied through the associated mass transport, since moving a vacancy by one lattice site is equivalent to moving a helium atom the same distance in the opposite direction. Because of the pressure dependence of $x_v$ in eqn. 2, a pressure gradient in a crystal will produce a corresponding vacancy concentration gradient. Thermal vacancies will diffuse from high to low concentration (low to high pressure), so mass will flow in the opposite direction, reducing the pressure gradient. The deformation associated with such vacancy diffusion flow is, for example, a limiting factor in metals for high temperature turbine applications. For helium, vacancy diffusion flow has been shown to explain

the frequency-dependent ultrasonic relaxation for solid $^4$He confined in the nanoscale pores of Vycor glass, giving vacancy activation energies similar to other techniques (Beamish *et al.*, 1991). Recent experiments studied the pressure-induced flow of solid $^3$He (Lisunov *et al.*, 2015, 2016) and $^4$He (Lisunov *et al.*, 2014) along 6-8 $\mu$m diameter channels through a 10 $\mu$m thick membrane. At high temperatures the flow was thermally activated, with the activation energies of vacancies. Although vacancy diffusion can also relax pressure gradients in larger samples, diffusion time constants scale with the square of the sample dimensions. In macroscopic crystals, vacancy diffusion is an effective annealing mechanism only at temperatures close to melting. Also, since vacancy activation energies increase with density, the vacancy concentration at a particular temperature decreases rapidly at high pressures and diffusion becomes much slower.

The quantum nature of helium crystals has important consequences for vacancies. The small energy barrier for exchange of a vacancy and a neighboring atom means that quantum tunneling is rapid, and vacancies can diffuse through helium crystals even at low temperatures. In the periodic lattice potential of $^4$He crystals they can propagate as quasiparticles known as "vacancions" (Andreev and Lifshits, 1969; Burns and Goodkind, 1994; Grigor'ev, 1997). Vacancies in solid $^3$He are also delocalized but, in contrast to $^4$He, are not expected to propagate coherently. At temperatures above a few mK, the $^3$He is in a paramagnetic state, with disordered spins. Exchange of a vacancy and a $^3$He atom changes the local spin configuration, so the lattice potential through which a vacancy moves is random, not periodic, and the vacancy motion is diffusive (Bernier and Hetherington, 1989).

Exchange in helium crystals gives vacancies a bandwidth which, if sufficiently large, creates an intriguing possibility that some vacancies in helium crystals could have negative energies. This would lead to a finite vacancy concentration at zero temperatures, i.e. an "incommensurate solid" with perfect periodicity but fewer atoms than lattice sites. In $^4$He crystals, these zero point vacancies (ZPV) would propagate and contribute to mass flow. They could even Bose condense to form a "vacancy supersolid" with coexisting positional and superfluid order. This mechanism was initially suggested as an explanation of apparent mass decoupling seen in torsional oscillator measurements on solid $^4$He (Kim and Chan, 2004a,b) but it is now clear that the apparent mass decoupling was caused by the extraordinary elastic effects described later in this paper, rather than being evidence of supersolidity (Beamish *et al.*, 2012; Maris, 2012; Reppy *et al.*, 2012). At present, there is no convincing experimental evidence for ZPV or for supersolidity in perfect crystals of $^4$He. This conclusion is supported by PIMC simulations on hcp $^4$He (Boninsegni *et al.*, 2006a; Prokof'ev and Svistunov, 2005) that find a vacancy activation energy of 13 K, consistent with experimentally measured values. The vacancies cluster and phase separate at low temperatures, leaving a defect-free solid with no zero point vacancies or evidence of superfluidity. However, PIMC simulations suggest that the vacancy activation energy in $^4$He may drop to zero in the presence of large strains (Pollet *et al.*, 2008), such as those near dislocations or grain boundaries.

### B. Impurities

Because of the low temperatures at which helium crystals are studied, most impurities present in helium gas freeze to the walls, leaving only isotopic impurities ($^3$He impurities in $^4$He, or $^4$He impurities in $^3$He). These are chemically identical to the atoms of the host crystal but have different effective sizes. The lighter $^3$He atoms occupy larger volumes in a $^4$He lattice because of their greater zero point motion, while $^4$He impurities are smaller than the host atoms in a $^3$He crystal. The isotopic impurities sit at lattice sites as substitutional impurities since interstitials are high energy defects in helium (Boninsegni *et al.*, 2006a).

Commercial helium gas has a $^3$He concentration $x_3$ of about $10^{-7}$ (100 ppb). However, this varies from about 25 to 300 ppb, depending on the source of the gas (Oxburgh *et al.*, 1986; Souris *et al.*, 2014). Lower $^3$He concentrations can be achieved by distillation ($\sim$1 ppb) or by a superfluid heat flush technique ($x_3 \lesssim 10^{-12}$) (Hendry and McClintock, 1987). It is, however, challenging to measure such low concentrations. This is most commonly done using dedicated helium mass spectrometers, which have resolution limits for $x_3$ of about 1 ppb (Amidon and Farley, 2010), although this can be extended to measure $^3$He concentrations in the $10^{-12}$ range. Accelerator mass spectroscopy has been used for measurements at even lower concentrations, down to $10^{-14}$ (Mumm *et al.*, 2016). The rarer and more expensive isotope, $^3$He, is harder to purify since distillation is not straightforward and the superfluid heat flush technique is not available. Impurity concentrations as low as $x_4 \approx 10^{-6}$ are possible, although not widely available.

Much purer $^4$He crystals can be produced *in situ* if they are in contact with liquid $^4$He at low temperatures, since $^3$He impurities are more tightly bound in the liquid. The difference in binding energies is 1.36 K (Edwards and Balibar, 1989), so the equilibrium $^3$He concentrations are very different at the low temperatures of many experiments, e.g. a ratio greater than $10^{20}$ at 20 mK (Pantalei *et al.*, 2010). However, defects in the solid provide sites where $^3$He impurities may be preferentially bound. Shear modulus measurements (Haziot *et al.*, 2013b; Syshchenko *et al.*, 2010) on hcp $^4$He show that edge dislocations are immobilized at low temperatures by $^3$He impurities, which bind to them with an en-

ergy $E_B$ ≈0.7 K . Since this is smaller than $^3$He's binding energy in liquid $^4$He, $^3$He impurities would still migrate to the liquid at low temperatures, but the binding sites in the solid may make it difficult to achieve equilibrium between the $^3$He concentrations in the solid and liquid. There may also be other locations in the crystal with even larger binding energies, e.g. nodes where dislocations meet or grain boundaries, so some $^3$He may remain attached to defects at low temperatures. However, $^4$He crystals can be grown from the superfluid at temperatures as low as 20 mK, where all the $^3$He impurities will remain in the liquid. This produces $^4$He crystals containing essentially no $^3$He (Pantalei *et al.*, 2010), although $^3$He impurities do accumulate at the $^4$He liquid-solid interface, with a binding energy estimated as 3 to 4 K (Rolley *et al.*, 1995a; Treiner, 1993; Wang and Agnolet, 1992).

At high temperatures, the motion of impurities is dominated by thermally activated vacancies, since the barrier for vacancy-impurity exchange is small. However, direct exchange with host atoms allows impurities to move, even in the absence of vacancies. At low temperatures this quantum tunneling allows $^3$He atoms to propagate as "impuritons" in the periodic $^4$He lattice. These quasiparticles have a bandwidth $zJ_{34}$ and group velocity $v_3 = zaJ_{34}$, where $z$ is the number of nearest neighbors (12 for hcp crystals) and $a$ is the atomic spacing. NMR measurements give a $^3$He-$^4$He exchange frequency $J_{34}/2\pi \approx 0.8$ MHz (Kim *et al.*, 2013), which implies that $^3$He atoms in solid $^4$He are very mobile at low temperature, with velocities of order cm/s. Their bandwidth $\Delta = zJ_{34}$ is ≈0.5 mK, so $^3$He impuritons are narrow band quasiparticles. This bandwidth is much smaller than the potential wells or barriers produced by elastic strains around dislocations or other $^3$He atoms, which results in large elastic scattering cross-sections for such defects (Andreev, 1982; Guyer *et al.*, 1971). The ballistic motion of $^3$He impurities is limited by $^3$He-$^3$He scattering, giving a mean free path inversely proportional to the $^3$He concentration (Grigor'ev, 1997), of order 100 nm at the lowest concentrations $x_3$ ≈60 ppm.

Less is known about the motion of $^4$He impurities in solid $^3$He since, being spinless, their diffusion cannot be studied directly with NMR techniques and, unlike vacancies, impurities do not contribute significantly to mass flow. The $^4$He impurities must be delocalized, with exchange rates comparable to those of $^3$He atoms in $^4$He crystals but, as for vacancies, spin disorder in solid $^3$He prevents them from propagating coherently.

### C. Dislocations

Dislocations are one-dimensional structural defects (Hull and Bacon, 2011) that can have edge or screw character, as illustrated in Fig. 8. The edge dislocation on the left is simplest to describe and can be thought of as the result of inserting a vertical half plane of atoms into the lattice. The bottom boundary of the half plane, the solid blue line in Fig. 8, is the edge dislocation. In the core region very close to the dislocation the crystal is highly distorted but far away the lattice deformations are small and can be described by linear elasticity. A dislocation is characterized by its Burgers vector, $\vec{b}$, the lattice vector defined by the gap in a path that makes a circuit around the dislocation that would close in a perfect crystal. For an edge dislocation, the Burgers vector (shown as a short black line above the diagram) is perpendicular to the dislocation line and to the added half plane that created it, i.e. horizontal in Fig. 8. A screw dislocation, illustrated on the right in Fig. 8, can be thought of as the result of cutting a slit partway through a a crystal and shifting the atoms on one side in the direction parallel to the border of the slit. For a screw dislocation, the Burgers vector (the short black line below the diagram) is parallel to the dislocation line (the edge of the slit, i.e. the solid blue line near the center of the diagram).

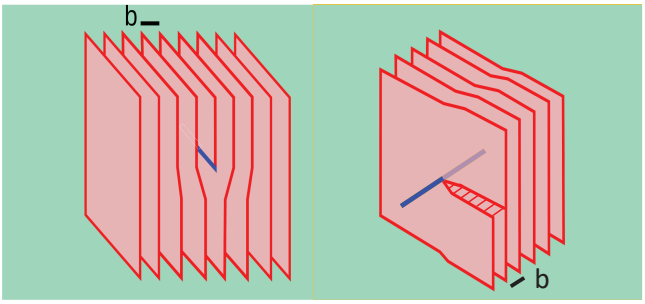


FIG. 8 Deformations around edge (left) and screw (right) dislocations. The dislocations are the lines near the centers of each diagram (shown in blue). The short black lines at the top (bottom) of the left (right) diagrams are their corresponding Burgers vectors **b**.

If a shear stress $\sigma$ is applied to a crystal containing a dislocation, the dislocation experiences a force proportional to the stress and can move via a process known as glide. An edge dislocation moves in the glide plane defined by the dislocation line and its Burgers vector. If the dislocation moves horizontally through a crystal, the top half of the crystal is displaced with respect to the bottom half over the slipped region, by an amount equal to the Burgers vector. This is illustrated in the left panel of Fig. 9. The dislocation shear strain $\epsilon_{dis}$ adds to the elastic strain $\epsilon_{el}$ that the shear stress would produce in a perfect crystal, increasing the total strain $\epsilon$ and therefore reducing the solid's effective shear modulus $\mu = \sigma/\epsilon$. Since glide involves only local rearrangements of atoms near the core of a dislocation, plastic deformation can occur at much smaller stresses than would be needed to displace the entire plane of atoms in a perfect crystal.

The energy of a dislocation depends on its position, so it moves in a "Peierls potential" with the periodicity of the lattice (Friedel, 1964; Suzuki *et al.*, 2013). The height of the energy barrier between neighboring minima is the Peierls energy (per unit length), $E_P$, and the minimum stress required to move a dislocation over this barrier is the Peierls stress, $\sigma_P = \frac{2\pi}{b^2} E_P$. The Peierls stress depends on the crystal structure and on the glide direction, and is usually smallest for glide in close-packed crystal directions. It also depends on the detailed structure of the dislocation core, decreasing exponentially with increasing dislocation width (Hull and Bacon, 2011), and is difficult to calculate accurately although there are general trends. In hcp and fcc materials, the dominant glide directions are usually in the close-packed planes. This leads to anisotropic slip behavior in hcp crystals where the slip occurs in the basal plane. General plastic deformations require slip in multiple directions so the stress at which they begin may be controlled by the largest Peierls barrier, not by the easy slip direction.

For dislocations that lie along crystallographic directions, the glide described above corresponds to moving the entire dislocation line from its low energy configuration along a lattice direction, over the Peierls barrier to the next lattice row. In fact, dislocations are not usually perfectly aligned with a lattice direction, which introduces "grown in" or "geometric" kinks, i.e. locations at which the dislocation line crosses between neighboring minima of the Peierls potential, as illustrated in the left diagram of Fig. 9. If such a kink moves along the full length of the dislocation, the entire line is displaced by one lattice constant. The one-dimensional periodic potential seen by a kink moving along the dislocation is generally smaller than the Peierls potential for moving an entire dislocation line, so glide may proceed by motion of kinks along dislocations. Even in the absence of geometric kinks, kink-antikink pairs can be thermally excited at high temperature, and dislocations can glide when these pairs separate and the kinks and antikinks move in different directions along the dislocation. In a quantum solid like helium, it is possible that these pairs could be created by tunneling, which would effectively eliminate the Peierls barrier and delocalize the dislocation.

In an hcp crystal, the primitive unit cell has a basis of two atoms. A perfect edge dislocation in the basal plane corresponds to inserting the vertical planes corresponding to both sets of atoms and has a Burgers vector $b$ equal to the lattice spacing in the basal plane. Inserting a single plane involves less lattice distortion, but the corresponding displacement is not a lattice vector of the hcp crystal. Instead it creates a "partial dislocation" with a Burgers vector $b_p = b/\sqrt{3}$ at an angle $\pm$ 30° with respect to the perfect dislocation. The perfect dislocation could split into two such partials which, being of the same sign, repel each other elastically. Since the elastic energy of a dislocation is proportional to the square

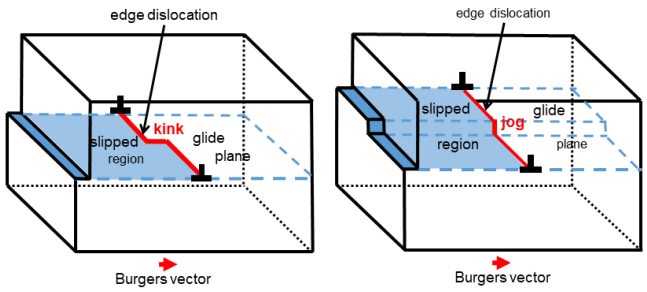


FIG. 9 Kinks (left diagram) and jogs (right diagram) on edge dislocations. An edge dislocation (the solid red line) corresponds to the edge of a vertical half plane inserted into the lattice. Its Burgers vector, indicated by the red arrow at the bottom of each diagram, is perpendicular to the dislocation line. The dislocation line and its Burgers vector define the horizontal glide plane, outlined by the dashed blue lines. The shaded regions of the glide plane are the portions of the crystal where slip has occurred. The kink (left panel) is a horizontal step in the dislocation line, in the direction of the Burgers vector. The jog (right panel) is a vertical step in the dislocation line, perpendicular to the Burgers vector.

of its Burgers vector, splitting into two widely separated partials would lower the total elastic energy by a third. However, this creates a stacking fault in the two dimensional region between the two partial dislocations (Hull and Bacon, 2011). The energy of this stacking fault is proportional to its area, i.e. to the separation $D$ between the partials, so there is an attractive force between them. The balance between these forces determines the equilibrium separation $D$ of the partials, roughly proportional to $\mu a^2/\gamma$, where $\gamma$ is the stacking fault energy per unit area. For the edge dislocation that glides in the basal plane of hcp crystals, the stacking fault corresponds to a layer of fcc structure. The hcp and fcc structures have the same number of nearest neighbors and very similar energies so $\gamma$ is small and this dislocation is expected to split into widely separated partials. In hcp crystals there are no stable stacking faults in other directions so edge dislocations with, for example, Burgers vectors along the c-axis do not split into partials.

In addition to glide, which does not require mass transport within the crystal, an edge dislocation can move in a direction perpendicular to its Burgers vector (vertically in Fig. 8) via a process known as climb. This involves adding or removing atoms at the edge of the inserted half plane, so requires mass flow to or from the dislocation. At high temperatures this can occur via diffusion of thermal vacancies. Dislocations do not climb as a straight line but rather form vertical jogs, as shown in the right hand diagram of Fig. 9. The jogs move along the dislocation when atoms are removed, allowing the dislocation to climb vertically. Jogs are essentially short sections of dislocations with a perpendicular orientation. If, as often

happens, the Peierls stress in that direction is large, jogs may pin the dislocations and prevent them from gliding.

For an edge dislocation like that shown in Fig. 8, the lattice is compressed above the dislocation and expanded below it. For screw dislocations, there is no compression, only shear distortions. Within the cores of dislocations, atomic displacements are large and depend on details of interatomic interactions, but at distances larger than a few lattice constants the deformations can be described as elastic strain fields. The energy per unit dislocation length associated with this elastic field can be computed by integrating the strain energy from the radius $r_0$ of the dislocation core region to a cutoff distance $R$ that is roughly the separation between dislocations (Hirth and Lothe, 1982; Hull and Bacon, 2011), giving

$$E_{edge} = \frac{\mu b^2}{4\pi(1-\nu)} \ln \frac{R}{r_0}; \qquad E_{screw} = \frac{\mu b^2}{4\pi} \ln \frac{R}{r_0} \quad (3)$$

for edge and screw dislocations, where $\mu$ and $\nu$ are the crystal's shear modulus and Poisson ratio (the crystal is assumed to be elastically isotropic). The dislocation's total energy includes the core energy, which is difficult to estimate, but is usually small compared to the elastic energy.

Dislocations cannot simply end within a crystal but two dislocations can join to form a third dislocation as long as the total Burgers vector is preserved. Dislocations form a network of connected dislocations, characterized by the dislocation density $\Lambda$ (total length of dislocations per unit volume) and the average distance between nodes, known as the network length $L_N$. These parameters are not independent - when the dislocation density is high the probability of intersecting is larger and the network length is smaller. If dislocations formed a perfect cubic network of intersecting dislocations, they would be related by $\Lambda L^2 = 3$. Networks in real crystals are disordered, of course, with, a distribution of network lengths. Also, if dislocations are somehow aligned to avoid crossing, e.g. parallel dislocations in a low angle grain boundary or non-intersecting 2D networks, then $\Lambda L^2$ can be much larger, as we will see for helium.

Defects like dislocations and impurities interact elastically through their strain fields. For example two parallel dislocations of the same sign (Burgers vectors in the same direction) repel each other, while dislocations of opposite sign attract. Similarly, an impurity with a radius $(1+\delta)r_a$ that is larger than $r_a$ of the host atoms (e.g. a $^3$He atom in a $^4$He crystal) will be attracted to the expanded region on one side of an edge dislocation. A smaller impurity (e.g. a $^4$He atom in a $^3$He crystal) will be attracted to the opposite side, where the lattice is compressed. The binding energy can be estimated as $E_B \sim \mu\delta\, v_a$ where $\delta$ is the misfit parameter and $\mu$ is the solid's shear modulus. The small value of $\mu$ for helium results in very small estimates of binding energies for isotopic impurities, e.g. $E_B$ ∼0.6 K for hcp $^4$He (Iwasa and Suzuki, 1980), similar to the binding energy inferred from elastic measurements, ∼0.7±0.1 K (Fefferman *et al.*, 2014; Syshchenko *et al.*, 2010). Using PIMC techniques, Corboz *et al.* (2008) have computed a binding energy of 0.8 K for a $^3$He atom on a screw dislocation in hcp $^4$He, but this has not been experimentally confirmed. The calculations required modifications of standard PIMC techniques and the origin of impurity binding is not obvious since there are only shear deformations around screw dislocations.

An impurity bound to a dislocation acts as a pinning center, since impurities normally can move through the lattice only via diffusion. However, individual impurities are relatively weak pinning centers and dislocations will break away from them at large stresses, leaving only the much stronger network pinning at nodes where dislocations meet. The impurity pinning length is inversely proportional to the concentration of impurities bound to the dislocation, $x_i^{dis} = x_i\, e^{\frac{E_B}{k_B T}}$, and in contrast to conventional solids where impurity motion freezes out during cooling, impurities in helium remain mobile at low temperature, so the dislocation and bulk impurity concentrations can quickly reach equilibrium. At low temperatures, $x_i^{dis}$ can be much larger than the bulk impurity concentration $x_{i0}$, e.g. by a factor of more than $10^8$ at 50 mK for $E_B = 1$ K. When $L_i = a/x_i^{dis}$ becomes comparable to the network length $L_N$, impurity pinning reduces the dislocations' mobility. At lower temperatures, impurities can saturate dislocation lines ($L_i \sim a$), completely immobilizing them.

The effects of gliding dislocations on a solid's elastic behavior were analyzed by Granato and Lücke (1956), in order to interpret measurements of ultrasonic velocities and attenuation in metals. They treated dislocations as mobile strings of length $L$, the distance between pinning points. The elastic energy per unit length in eqn. 3 acts as a line tension $C$. When a stress is applied to the crystal, a dislocation loop experiences a force per unit length $F = \sigma b$, where $\sigma$ is the component of the shear stress in the dislocation's glide plane, in the direction of its Burgers vector. It moves in response to this force, bowing out between pinning points. For a static stress, the average displacement (Granato and Lücke, 1956) of the dislocation is $\xi_0 = (16b/\pi^5 C)\sigma L^2$. Over the area swept out by the dislocation line, $\xi_0 L$, the crystal has slipped a distance $b$. The strain produced by a density $\Lambda$ of dislocations of length $L$ is $\epsilon_{dis} = \Lambda b \xi_0$. The total strain is the sum of this dislocation strain and the elastic strain $\epsilon_{el}$ that would occur in a dislocation-free crystal. The resulting shear modulus, $\mu = \sigma/(\epsilon_{el} + \epsilon_{dis})$ is reduced from its intrinsic value in a perfect crystal, $\mu_0 = \sigma/\epsilon_{el}$, i.e. dislocation motion softens the crystal. Its shear modulus is reduced by a factor proportional to $\Lambda L^2$ so a few long dislocations can have the same effect as many short ones.

To extend this model to the high frequencies used in

ultrasonic measurements, the inertia and damping of dislocations had to be considered. A dislocation gliding through a crystal at speed $v_d$ carries with it a strain field that accelerates nearby atoms, giving the dislocation an effective mass per unit length $\pi\rho b^2$. The moving dislocation is damped, for example by the scattering of thermal phonons, which gives a resistive force (per unit length) proportional to its velocity, $F_d = -Bv_d$. Phonon scattering from a dislocation's static strain field gives a damping $B \propto T^5$. However, the absorption and re-emission of phonons by mobile dislocations is a more effective scattering mechanism at low temperatures. The damping coefficient for this "fluttering" mechanism has been calculated (Ninomiya, 1974) as

$$B = \frac{14.4k_B^3}{\pi^3\hbar^2c^3}T^3 \tag{4}$$

where $c$ is the Debye sound speed of the solid.

The Granato-Lucke equation of motion for the displacement $\xi(x,t)$ at time $t$ and position $x$ along a dislocation line driven by a stress $\sigma(t)$ is

$$A\ddot{\xi} + B\dot{\xi} - C\frac{\partial^2\xi}{\partial x^2} = b\sigma \tag{5}$$

where $A = \pi\rho b^2$ is the effective mass and $C$ is the line tension from eqn. 3. In acoustic applications, the stress is periodic, $\sigma_0 e^{i\omega t}$. For small damping, e.g. at low temperatures, a dislocation loop of length $L$ has a sharp resonance at an angular frequency

$$\omega_0 = 2\pi f_0 = \sqrt{\frac{2}{1-\nu}}\frac{v_t}{L} \tag{6}$$

where $v_t = \sqrt{\mu/\rho}$ is the shear sound speed in the solid. For a 10 $\mu$m long dislocation in solid $^4$He, this occurs at $f_0 \sim 10$ MHz. At acoustic frequencies well below $f_0$, the dislocation motion and associated strain $\epsilon_{dis}$ are in phase with the applied stress, so the shear modulus is reduced from its purely elastic value. At frequencies above $f_0$, the dislocation's inertia dominates and the dislocation strain is out of phase with the applied stress, increasing the shear modulus. If the crossover frequency can be measured, the loop length between pinning points can be determined.

Of course, the Granato-Lucke model of dislocations contains a number of assumptions. It assumes that the dislocations move freely like strings, i.e. that they are not affected by the lattice Peierls potential. This is plausible for dislocations with easy glide directions, e.g. in the basal plane of hcp crystals. It assumes that pinning points are static, but $^3$He impurities are highly mobile in solid $^4$He and may not be very effective pinning centers. It also oversimplifies a number of aspects of the dislocations' response to stresses. Some are easily fixed, e.g. by including an orientation factor $R$ to account for the component of the applied stress in the dislocation's glide plane. Others are more complicated, e.g. writing the dislocation's properties in terms of the crystal's elastic constants $C_{ij}$ rather than using a shear modulus and Poisson ratio for an isotropic medium. However, the effects of including elastic anisotropy are modest compared to other approximations in the model.

An important limitation when using this model to extract dislocation densities from ultrasonic or acoustic data is that dislocation loops in real crystals are not all the same length. Although it may be reasonable to assume an exponential distribution of lengths $L_i$ for random impurity pinning, the dislocation network itself is disordered, with an unknown distribution of network lengths $L_N$. Integrating over an assumed distribution of loop lengths affects the calculated dislocation densities, particularly in the case of short loops that make very little contribution to elastic properties. Also, it is important to remember that not all dislocations are mobile, e.g. edge or screw dislocations in glide planes with large Peierls barriers do not respond to small shear stresses and will not be detected in acoustic measurements.

### D. Grain boundaries and stacking faults

As shown in Fig. 5, freezing can nucleate at more than one location, producing multiple helium crystals with different orientations. Samples grown by rapid injection or using the blocked capillary technique have smaller crystallites and more grain boundaries. These grain boundaries can affect a solid's mechanical behavior, for example by acting as sources and sinks for dislocations and vacancies. They may also include disordered or liquid-like layers where superflow could occur in solid $^4$He samples, as suggested by PIMC studies that identified some grain boundaries in $^4$He as superfluid (Pollet *et al.*, 2007). Close to the melting curve, thicker superfluid films can appear at grain boundaries and superfluid channels appear where three grain boundaries meet, or where grain boundaries meet a wall (Franck *et al.*, 1983; Sasaki *et al.*, 2007).

When crystals with similar orientations meet, the resulting grain boundary is essentially an array of edge dislocations with spacing inversely proportional to the angle between the crystals. Such low angle grain boundaries can be detected via the line broadening ("mosaic spread") they produce in diffraction measurements. Synchrotron x-ray measurements on hcp $^4$He crystals grown at constant pressure (Burns *et al.*, 2008) showed single crystals of cm dimensions, although faster freezing produced multiple crystals with sizes of a few mm. However, the mosaic angle (typically about $6.5\times10^{-4}$ rad) within these large crystals indicated that they contained low angle grain boundaries corresponding to arrays of dislocations separated by about 1500 $b$. At high temperatures (above 0.7 $T_m$), these boundaries were not fixed. Their

motion appeared to be driven by stress gradients and increased with temperature. Earlier neutron diffraction experiments (Pelleg *et al.*, 2006) showed similar motion of low angle boundaries in bcc $^4$He, but not in the hcp phase. Sub-boundaries have been directly imaged in x-ray topography imaging studies on $^4$He single crystals (Iwasa, 2002; Iwasa *et al.*, 1987, 1995), although individual dislocations could not be resolved.

Another type of 2-dimensional defect can be produced during crystal growth or by vacancies and dislocations. A stacking fault (Hull and Bacon, 2011) occurs where the sequence of atomic planes of a perfect crystal is disrupted. For example, an fcc crystal is made up of close-packed planes arranged in an ABCABCABC order, while an hcp crystal consists of the same close-packed atomic planes alternating in an order ABABABAB. If the regular sequence is disrupted, for example a crystal with stacking sequence ABABCBCB, two hcp regions are separated by a stacking fault that is essentially a layer of fcc structure. The hcp and fcc structures have the same coordination number and configuration of nearest neighbors. They differ only in the arrangement of atoms at larger distances so their energies are similar.

In helium, the hcp/fcc energy difference and the corresponding stacking fault energy per unit area, $\gamma$, are very small. For $^4$He, $\gamma$ can be roughly estimated using the measured latent heat for the hcp-fcc transition at 113 MPa (Franck, 1980), which gives a value of about $\gamma \approx 10^{-5}$ J/m$^2$. However, $\gamma$ is expected to be much smaller at pressures around 2.5 MPa where most measurements on solid $^4$He have been made and stacking fault energies $\gamma \sim 2\times10^{-6}$ J/m$^2$ have been computed by Borda *et al.* (2016) using PIMC methods. Stacking fault energies are much larger in conventional materials, typically around 0.1 J/m$^2$, and even for an inert gas crystal like krypton (Keyse and Venables, 1985) they are about three orders of magnitude larger than in solid helium.

Stacking faults can be created during thermal quenching, when vacancies condense and create voids which then collapse, leaving prismatic dislocation loops. They are also created when a perfect dislocation separates into two partial dislocations. Whether a particular dislocation splits, and the spacing $D$ between the partials, depends on the stacking fault energy. The small value of $\gamma$ leads to large splitting of edge dislocations in the basal plane of hcp $^4$He. Borda *et al.* (2016) estimate an elastic splitting of about 43 nm, i.e. more than $100b$. Their PIMC simulations confirmed that these dislocations are split by at least $11b$, a lower limit set by the size of the simulation box.

## IV. ELASTIC PROPERTIES OF SOLID $^4$HE AND $^3$HE

### A. Sound modes and elastic constants $C_{ij}$

Inert gases interact via weak, spherically symmetric Van der Waals potentials and form simple crystal structures at low temperatures, making them an attractive testing ground for calculations of elastic properties. Classical lattice dynamics gives a good description of the heaviest gases, but the behavior of helium is dominated by quantum effects. Nonetheless, sound propagates normally in solid helium crystals and their elastic constants have been determined from ultrasonic and inelastic neutron scattering (INS) measurements of sound speeds.

Single crystals are anisotropic and their full set of elastic constants is needed to calculate sound speeds and polarizations in different crystallographic directions. When appropriately averaged, these give the shear and bulk moduli for polycrystalline samples (Maris and Balibar, 2010). Elastic constants have been measured near the melting temperatures for all three crystallographic phases of $^4$He (bcc, hcp and fcc), but only for the bcc phase of $^3$He. Cubic crystals (e.g. bcc and fcc) have three independent elastic constants ($C_{11}$, $C_{12}$ and $C_{44}$). Under hydrostatic pressure they compress isotropically, with a bulk modulus $B = \frac{1}{3}(C_{11} + 2C_{12})$. Hexagonal crystals (e.g. hcp) have five independent elastic constants ($C_{11}$, $C_{12}$, $C_{13}$, $C_{33}$ and $C_{44}$). Their elastic properties are isotropic about the c-axis, but under hydrostatic pressure the strain parallel to the c-axis can differ from that in perpendicular directions, so the expression for the bulk modulus is more complicated. However, in hcp $^4$He the c/a ratio, which is very close to the 1.633 value for ideal close packing, is known to be essentially independent of pressure (Franck and Wanner, 1970). This implies that $C_{11} + 2C_{12} \approx C_{33} + 2C_{13}$, which gives a simplified expression for hcp $^4$He's bulk modulus $B \approx \frac{1}{3}(C_{33} + 2C_{13})$.

Table I gives measured values of the elastic constants of solid helium. In $^4$He, the bcc phase exists only over a narrow range around a molar volume of 21.0 cm$^3$. This corresponds to the pressure (2.8 MPa) at which its bcc elastic constants are listed in Table I (Greywall, 1976). The ultrasonic measurements (Greywall, 1971, 1977a) for hcp $^4$He extend over a molar volume range from 20.97 to 19.28 cm$^3$/mol (pressures from 2.6 to 5.8 MPa). Recent quantum mechanical calculations of the zero temperature elastic constants of hcp $^4$He (Cazorla *et al.*, 2012; Pessoa *et al.*, 2012) are in good agreement with the experimental values. Inelastic neutron scattering measurements (Eckert *et al.*, 1977, 1978; Reese *et al.*, 1971; Thomlinson *et al.*, 1978) have also provided some information on elastic constants of hcp $^4$He at pressures up to 370 MPa (molar volume 9.41 cm$^3$) and of fcc $^4$He at a pressure of 493 MPa (molar volume 9.03 cm$^3$).

The bcc phase is stable over a wider range in $^3$He, from 24.9 to 18.9 cm$^3$/mol (pressures from 2.93 to 13.7

| isotope (bcc) | $V_m$ (cm$^3$) | P (MPa) | $C_{11}$ (MPa) | $C_{12}$(MPa) | $C_{44}$ (MPa) | $B$ (MPa) | $A$ |
|---|---|---|---|---|---|---|---|
| $^4$He | 21.00 | 2.8 | 31.1±.7 | 28.1±.6 | 21.7±.2 | 29.1±.6 | 14±6 |
| $^3$He | 24.45 | 3.3 | 20.16±.2 | 16.73±.4 | 9.29±.1 | 18.0±.3 | 5.3±1 |
| $^3$He | 21.66 | 6.5 | 38.0±.5 | 34.5±.8 | 19.8±.3 | 35.9±.7 | 11±4 |

| isotope (fcc) | $V_m$ (cm$^3$) | P (MPa) | $C_{11}$ (GPa) | $C_{12}$(GPa) | $C_{44}$ (GPa) | $B$ (GPa) | $A$ |
|---|---|---|---|---|---|---|---|
| $^4$He | 9.97 | 292 | 1.56±.07 | 1.06±.07 | 0.79±.02 | 1.23±.07 | 3.2±1 |
| $^4$He | 9.43 | 380 | 2.17±.02 | 1.62±.03 | 1.00±.02 | 1.80±.03 | 3.6±0.4 |
| $^4$He | 9.03 | 453 | 3.13±.23 | 2.24±.23 | 1.19±.05 | 2.54±.23 | 2.7±1.5 |

| isotope (hcp) | $V_m$ (cm$^3$) | P (MPa) | $C_{11}$ (MPa) | $C_{33}$(MPa) | $C_{12}$ (MPa) | $C_{13}$(MPa) | $C_{44}$ (MPa) |
|---|---|---|---|---|---|---|---|
| $^4$He | 20.97 | 2.6 | 40.5±.4 | 55.4±2 | 21.2±.4 | 10.5±1 | 12.4 ±.2 |
| $^4$He | 20.55 | 3.2 | 46.6±.2 | 60.4±4 | 26.1±.4 | NA | NA |
| $^4$He | 20.32 | 3.6 | 55±2 | 71±3 | 29±1 | 13.1±1 | 14.0 ±1 |
| $^4$He | 19.5 | 5.3 | 64.1±4 | 87.3±6 | 34.9±.3 | NA | NA |
| $^4$He | 19.28 | 5.8 | 76±3 | 98±4 | 42±2 | 19.8±1 | 19.6 ±1 |
| $^4$He | 16.00 | 21.4 | 170±30 | 240±20 | 95±20 | NA | 50 ±10 |
| $^4$He | 11.61 | 160 | 1130±70 | 1260±40 | NA | NA | 240 ±10 |
| $^4$He | 9.41 | 370 | 2820±80 | 3200±60 | NA | NA | 5660±10 |
| $^3$He | 18.77 | 15.0 | [135±14] | [156±16] | [43±4] | [39±4] | [36 ±4] |

TABLE I Elastic constants of solid helium in its different crystallographic phases: bcc (top), fcc (middle) and hcp (lower panel). The first three columns give the isotope ($^4$He or $^3$He), the molar volume and the pressure. For the bcc and fcc phases, the other columns give the three elastic constants of cubic crystals, the bulk modulus $B$ and the anisotropy $A$. For the hcp phases they give the five hexagonal crystal elastic constants. Data are from ultrasonic velocity measurements (Crepeau *et al.*, 1971; Greywall, 1971, 1975, 1976, 1977a) or, for pressures above 20 MPa, from inelastic neutron scattering measurements (Eckert *et al.*, 1978; Reese *et al.*, 1971; Thomlinson *et al.*, 1978). The hcp $^3$He elastic constants (in square brackets) are calculated values (Schoffel and Muser, 2001) since there have been no experimental measurements for the hexagonal $^3$He phase.

MPa), and extends to zero temperature. Its elastic constants have been measured at densities between 21.66 and 24.45 cm$^3$/mol (Greywall, 1975). The elastic constants of hcp $^3$He have not been measured but Table I includes calculated values for a molar volume of 18.77 cm$^3$/mol, computed using path integral techniques (Schoffel and Muser, 2001). These hcp elastic constants are expected to be quite accurate since the corresponding elastic constants computed for the bcc phase of $^3$He agree well with experimental values.

The ultrasonically determined elastic constants in Table I were measured near the crystals' melting points. The neutron scattering measurements were made at temperatures between 4.2 and 10 K (for hcp $^4$He) and between 19 and 22 K (for fcc $^4$He). At pressures below 20 MPa, the variations of the elastic constants with temperature are smaller than their experimental uncertainties. For the highest pressure fcc $^4$He sample, with a melting temperature of 38.5 K, the elastic constants decrease by more than 10% at the melting point.

At low pressures, solid helium has extremely small elastic constants, for example a bulk modulus about 35 and 140 times smaller than those of neon and xenon, respectively (Beamish, 2001). Although some of this difference is attributable to helium's weak interatomic attraction, much of it is the result of its large zero point motion. This expands solid helium's lattice and makes it about 25 times more compressible than a classical crystal with the same interatomic potential. Its large compressibility means that applying the maximum pressure shown in Table I (453 MPa) changed $^4$He's density by a factor of 2.3, which increased its elastic constants by a factor of 100. Helium's small elastic constants also mean that sound propagates very slowly, at speeds as low as 75 m/s for transverse waves at low pressures.

Figures 10 and 11 show the density dependences of the elastic constants of the bcc and hcp phases of helium. The shear elastic constants $C_{44}$ of bcc $^3$He and $^4$He fall on a common curve, in contrast to $C_{11}$, $C_{12}$ and the bulk modulus $B = \frac{1}{3}(C_{11} + 2C_{12})$, which are significantly lower for $^4$He. This is not surprising since the zero point energy is larger for $^3$He, which increases its pressure and bulk modulus compared to $^4$He at the same density. Zero point motion also affects helium's elastic constants in other ways. Compared to crystals of the other inert gases (which have the fcc structure), the anisotropy parameter $A = \frac{2C_{44}}{(C_{11}-C_{12})}$ is unusually large for bcc helium (Beamish, 2001). This results in ultra-

sonic beam deviations as large as 60° and consequent difficulties in observing the transverse modes in some crystallographic directions (Wanner, 1971). In bcc and fcc crystals, where atoms sit at centers of inversion symmetry, the elastic constants should obey the Cauchy relation $C_{12} - P = C_{44} + P$, where $P$ is the pressure, provided that thermal and quantum motion can be neglected. Despite the importance of zero point motion in helium, this relationship holds as well in bcc and fcc helium as in the fcc crystals of the heavier inert gases (Beamish, 2001).

In hcp crystals, atoms do not sit at centers of inversion symmetry so there are no equivalent Cauchy relations. The empirical relation $C_{11} + 2C_{12} \approx C_{33} + 2C_{13}$, which follows from the constant c/a ratio of hcp $^4$He, holds within the uncertainty of the measurements, so the bulk modulus is quite accurately given by $B \approx \frac{1}{3}(C_{33} + 2C_{13})$. This bulk modulus is plotted in Fig. 11 (circles).

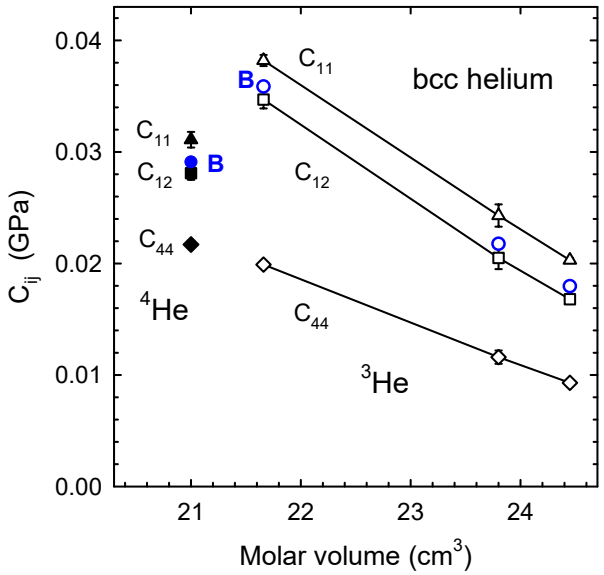


FIG. 10 Elastic constants and bulk modulus of bcc helium from ultrasonic measurements (Greywall, 1971, 1975, 1976). $C_{44}$ (diamonds), $C_{12}$ (squares), $C_{11}$ (triangles) and bulk modulus B (circles) for bcc $^3$He (open symbols) and $^4$He (solid symbols at left).

### B. Intrinsic temperature dependence

Even in defect-free crystals, elastic constants and dissipation depend on temperature because of the anharmonicity of the lattice. The anharmonicity is also responsible for thermal expansion or, in the case of helium crystals that are confined in a rigid cell at constant volume, the temperature dependence of the pressure. This intrinsic temperature dependence is related to $u(T)$, the crystal's internal thermal energy per unit volume, by a Gruneisen equation $P(T) = P_0 + \gamma u(T)$. The Gruneisen

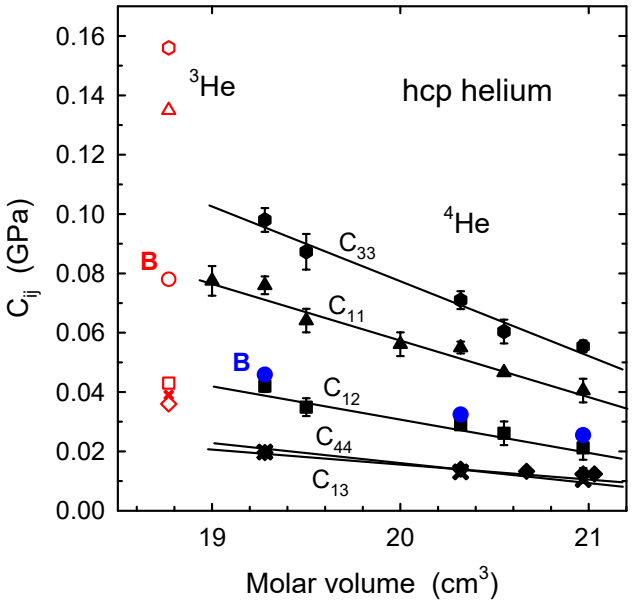


FIG. 11 Elastic constants and bulk modulus of hcp $^4$He (solid symbols) from ultrasonic measurements (Crepeau *et al.*, 1971; Greywall, 1971, 1977a), and of hcp $^3$He (open symbols) from path integral simulations (Schoffel and Muser, 2001). $C_{44}$ (diamonds), $C_{12}$ (squares), $C_{11}$ (triangles) $C_{13}$ (crosses) $C_{33}$ (hexagons) and bulk modulus B (circles).

constant $\gamma$ is often nearly independent of temperature so that at low temperatures the thermodynamic pressure increase in a dielectric crystal (due to thermal phonons) is proportional to $T^4$. The elastic constants $C_{ij}$ have a similar temperature dependence (McGreer and Franck, 1990)

$$C_{ij}(T) = C_{0ij} - \Gamma_{ij} u(T) \qquad (7)$$

where $\Gamma_{ij}$ are related to the crystal's generalized Gruneisen constants. Elastic constants and sound speeds are therefore expected to decrease as the temperature increases, by amounts proportional to $u$. The Debye temperatures of helium crystals are much higher than their melting temperatures (Trickey *et al.*, 1972), so the decreases are expected to be roughly proportional to $T^4$.

Figure 12 shows the transverse mode elastic constant $\hat{C}_0 = \rho v_t^2$ that McGreer and Franck (1990) calculated from ultrasonic measurements of the speed $v_t$ of 3 MHz shear waves in single crystals of hcp $^4$He. This crystal was grown at high pressure (15 MPa) and the measurements were made between 7 and 15 K. As expected, the decrease in this elastic constant was linearly related to the crystal's total thermal energy $u(T)$.

A $T^4$ variation of sound speeds is also seen in helium crystals at lower pressures, at temperatures near melting. However, as described in the next section, dislocations in helium become mobile and make additional contributions

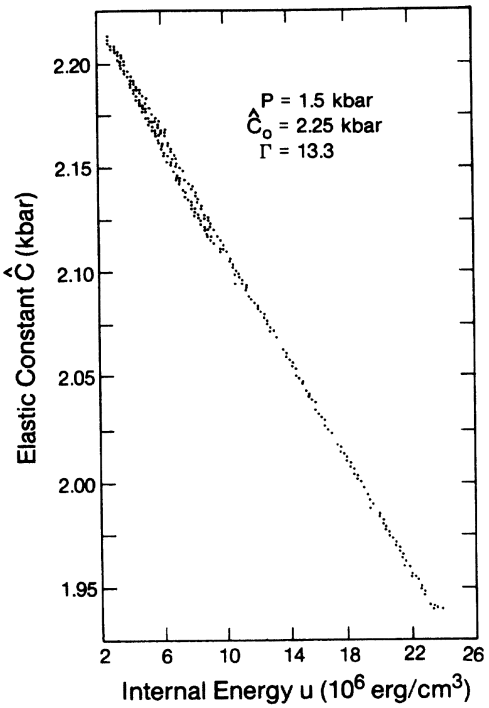


FIG. 12 Effective elastic constant $\hat{C}_0$ for transverse ultrasound in hcp $^4$He at high pressure (15 MPa), plotted vs. total internal energy $u$ (McGreer and Franck, 1990).

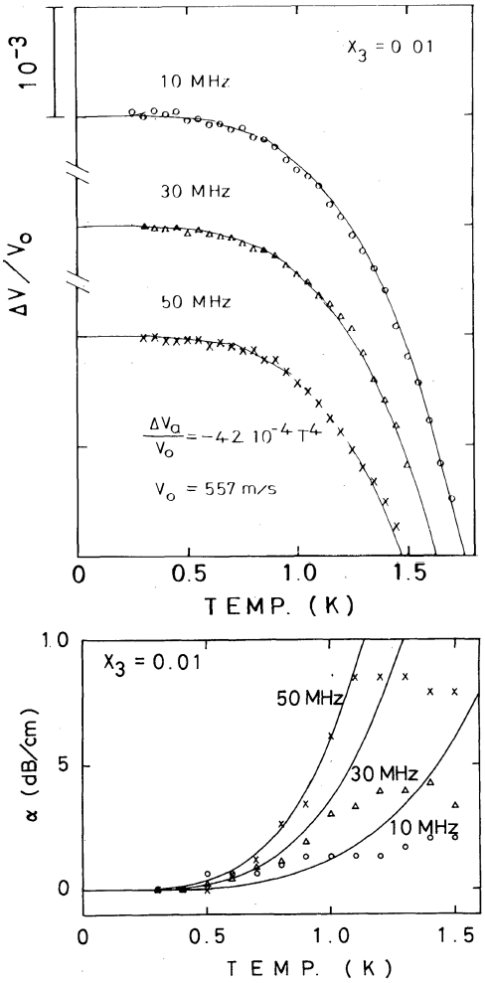


FIG. 13 Longitudinal sound velocity (upper panel) and attenuation (lower panel) in an hcp $^4$He single crystal containing 1% of $^3$He (Iwasa and Suzuki, 1980). The sound frequencies are 10 MHz (circles), 30 MHz (triangles) and 50 MHz (crosses). Solid lines are fits of the velocity data to the expected thermal phonon dependence $V_0 - AT^4$ and of the attenuation to the $\omega T^4$ dependence expected for "zero sound" at low temperature (Maris, 1971).

to the sound speeds at low temperatures. These dislocations can be pinned by impurities, immobilizing them and restoring the crystal's intrinsic temperature dependence. The expected frequency independent $T^4$ variation was seen in longitudinal sound velocity measurements on hcp $^4$He crystals containing 1% of $^3$He impurities (Iwasa and Suzuki, 1980). The top panel of Fig. 13 shows data at 10, 30 and 50 MHz; the solid lines are the expected $T^4$ dependence. Similar behavior has been seen in $^3$He crystals (Beamish and Franck, 1983). Figure 14 shows the variation of the longitudinal sound speed in an hcp $^3$He crystal containing 0.5% $^4$He, with the expected dependence due to thermal phonons.

Note that the intrinsic sound velocity changes in the hcp crystals of Figs. 13 and 14 are small, corresponding to elastic constant decreases of less than 1% at the melting temperature. In low density bcc $^3$He crystals, the changes are even smaller, but include contributions from thermally excited vacancies as well as phonons (Iwasa and Suzuki, 1982). The 12% changes in the high pressure $^4$He crystal of Fig. 12 reflect the much higher temperatures in those measurements. The maximum temperature in the measurements of Fig. 12 correspond to about 15% of the crystal's Debye temperature, $\Theta \approx 100$ K (Trickey *et al.*, 1972). This can be compared to the maximum temperatures in Figs. 13 and 14, which are only about 6% of the crystals' Debye temperatures (around 30 and 40 K, respectively), with correspondingly smaller changes in elastic constants. For comparison, the elastic constants of the heavier inert gas crystals (Ar, Kr, Xe) decrease by more than 30% at their melting temperatures (Beamish, 2001).

The lower panel of Fig. 13 shows the ultrasonic attenuation at 10, 30 and 50 MHz. It is roughly proportional to $\omega T^4$ below 1 K, the attenuation expected from three-phonon scattering processes in dielectric crystals (Maris, 1971). At high temperatures, the phonon scattering time $\tau$ decreases, giving approximately constant attenuations in the regime above 1 K where $\omega\tau < 1$. A $T^4$ dependence was also observed at GHz frequencies in Brillouin scattering measurements on hcp $^4$He crystals (Berberich *et al.*,

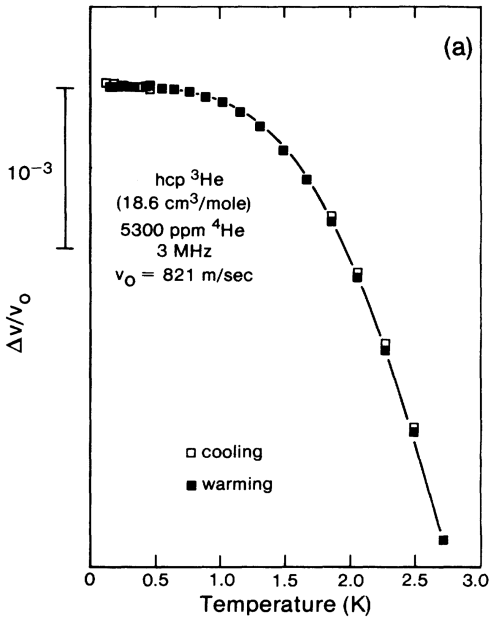


FIG. 14 Temperature dependence of the longitudinal sound speed in an hcp $^3$He single crystal containing 0.53% $^4$He impurities. The solid line is a fit to the intrinsic thermal phonon dependence (Beamish and Franck, 1983).

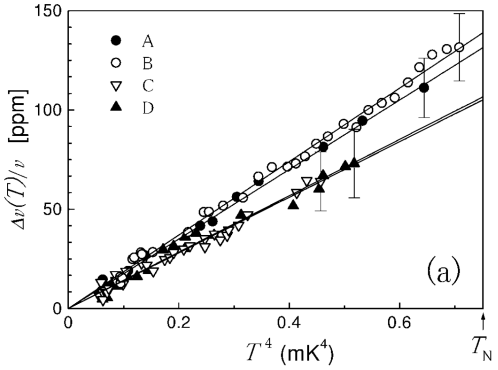


FIG. 15 Sound velocity (11 MHz longitudinal ultrasound) in magnetically ordered bcc $^3$He single crystals in coexistence with liquid $^3$He along the melting curve (3.44 MPa). The different symbols correspond to crystals with different orientations (Nomura *et al.*, 2000).

1975). In purer crystals, dislocations are mobile at low temperatures and add to the attenuation, overwhelming this intrinsic behavior.

At temperatures below 100 mK, the heat capacity of low density $^3$He is dominated by spin exchange, and the internal energy has the $1/T$ dependence characteristic of a paramagnet. The corresponding low temperature decrease in sound speed has been observed by Fartash and Goodkind (1986), who made measurements on a 24.1 cm$^3$/mol bcc $^3$He crystal at temperatures as low as 12 mK, which is still well above bcc $^3$He's magnetic ordering temperature $T_N$=0.93 mK. In the magnetically ordered state below $T_N$, the thermal excitations are spin waves with very low velocities (7.8 cm/s), so the spin wave energy $u(T) = \frac{\pi^2\hbar}{15c^3}(\frac{k_BT}{\hbar})^4$ and corresponding sound velocity changes are large. Remarkably, this large $T^4$ dependence has been measured in bcc $^3$He crystals at temperatures below 1 mK (Nomura *et al.*, 2000), as shown in Fig. 15. The velocity change below 0.93 mK is more than 0.01%, comparable to the total velocity changes below 1 K in Figs. 13 and 14.

### C. Dislocation effects

Dislocations affect the elastic properties and sound speeds if they move in response to stresses. This occurs in helium crystals, where mobile dislocations often dominate the temperature dependence of sound velocities. This first became clear when ultrasonic measurements on hcp $^4$He single crystals were extended to low temperatures. Figure 16 shows data for five different single crystals (curves A to E) grown at the same pressure. Below about half the melting temperature ($T_M \approx$1.9 K), the longitudinal sound speeds deviated from the intrinsic $T^4$ dependence that described the data at higher temperatures (Wanner *et al.*, 1976). The deviations were smooth, with magnitudes as large as 0.3%, comparable to the intrinsic velocity changes. The size and sign of the velocity anomaly varied from crystal to crystal, consistent with the random variations expected for dislocation networks produced during crystal growth.

Surprisingly, since dislocations are usually thought of as softening crystals, the velocity anomalies in Fig. 16 were positive in more than half the samples. As discussed in Section III C, mobile dislocations act as vibrating strings, pinned at nodes where they intersect with other dislocations. If the damping is not too large, these strings have a resonance at a frequency $f_0$ given by eqn. 6. For sound frequencies below $f_0$, dislocations move in phase with the applied sound stress and the dislocation strain adds to the elastic strain, softening the crystal and reducing the ultrasound velocity. At frequencies above the dislocation loops' resonance resonant frequency, however, the dislocation motion is out of phase with the sound stress, stiffening the crystal and increasing the sound speed. In Fig. 16, the longitudinal sound speeds were measured at 8 MHz for crystals D and E, which showed negative velocity deviations at low temperatures, and at 12 MHz for the other three crystals, which showed positive deviations. This suggests that the anomalies were due to dislocation loops with resonance frequencies around 10 MHz, corresponding to lengths between pinning points of about 10 $\mu$m. The authors noted that real crystals would have a distribution of loop lengths and showed that the velocity anomalies could be

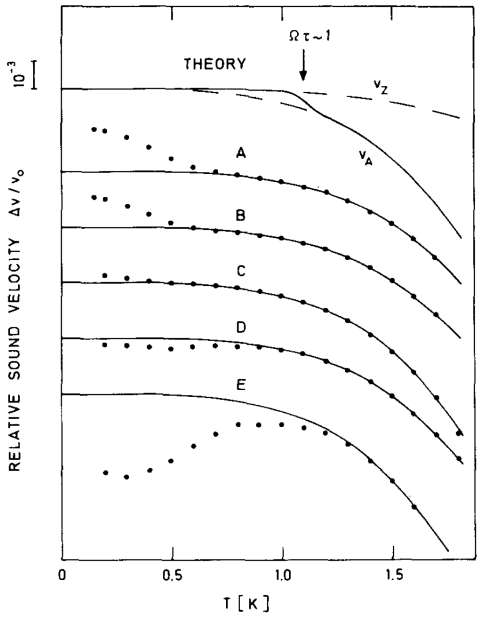


FIG. 16 Ultrasonic velocities in hcp $^4$He single crystals at 3.6 MPa (Wanner *et al.*, 1976). The curves labeled A (top) through E (bottom) correspond to different crystals grown under the same conditions. Solid lines are fits to the high temperature intrinsic behavior.

explained by considering just two different loop lengths.

Although the Granato-Lucke model could describe the velocity at a single frequency, the dislocation densities derived from the fits varied from crystal to crystal, from $0.7\times10^5/\text{cm}^2$ to $4.3\times10^5/\text{cm}^2$, and the average loop lengths varied between 6 and 11 $\mu$m. A more stringent test of the model requires measurements at multiple frequencies. Such measurements were first made by Iwasa *et al.* (1979). Figure 17 shows longitudinal sound speeds at frequencies of 10, 30 and 50 MHz in an hcp $^4$He crystal grown from natural purity helium gas (less than 1 ppm of $^3$He impurities). The velocity anomaly was positive and, as expected, depended strongly on frequency, confirming the resonant nature of the dislocation interaction. Similar measurements were soon made on hcp and bcc single crystals of $^3$He (Beamish and Franck, 1982). The velocity anomalies, after subtracting the high temperature intrinsic dependence, are shown in Fig. 18. By using lower frequencies, these measurements unambiguously showed the crossover from low frequency softening at 3 MHz to high frequency stiffening at 9 MHz, convincing evidence of a resonance between 3 and 9 MHz. This is consistent with the $^4$He measurements of Fig. 17, where the positive anomaly indicates a dislocation resonance frequency below 10 MHz.

To describe the frequency and temperature dependence of the sound velocities, and of the accompanying sound attenuation (shown in the lower panels of Figs. 17 and 18), a distribution of dislocation loop lengths was

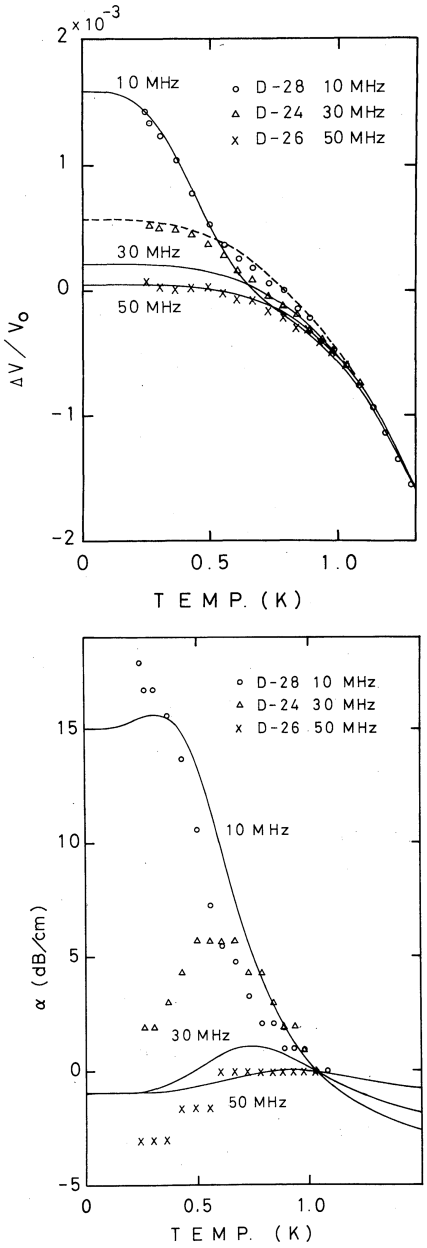


FIG. 17 Dislocation fit of the frequency dependent longitudinal sound velocity (upper panel) and attenuation (lower panel) in hcp $^4$He (Iwasa *et al.*, 1979). The sound frequencies are 10 MHz (circles), 30 MHz (triangles) and 50 MHz (crosses). ©(1977) The Physical Society of Japan.

needed. In the Granato-Lucke model, the contributions to the sound velocity and attenuation from a unit density of loops with length $l$ (resonance frequency $\omega_0$) are

$$\frac{\Delta v(l)}{v_0} = -\frac{4v_0^2}{\pi^3}\frac{\omega_0^2-\omega^2}{(\omega_0^2-\omega^2)^2+(B\omega/A)^2} \tag{8}$$

and

$$\alpha(l) = -\frac{4v_0}{\pi^3}\frac{\omega_0^2 B/A}{(\omega_0^2-\omega^2)^2+(B\omega/A)^2}. \tag{9}$$

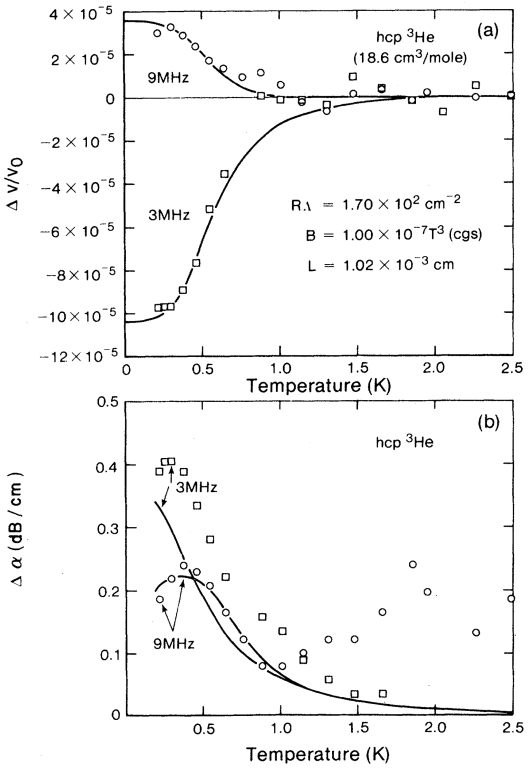


FIG. 18 Dislocation fit of the frequency dependent longitudinal sound velocity (upper panel) and attenuation (lower panel) in hcp $^3$He (Beamish and Franck, 1982). The sound frequencies are 3 MHz (squares) and 9 MHz (circles).

For a distribution of loop lengths $N(l)$, the total velocity change and attenuation are

$$\frac{\Delta v}{v_0} = R \int \frac{\Delta v(l)}{v_0} l N(l) \mathrm{d}l \tag{10}$$

and

$$\alpha = R \int \alpha(l) l N(l) \mathrm{d}l \tag{11}$$

where $R$ is a numerical factor, of order 0.1, that depends on the orientation of the crystal with respect to the sound polarization. Since the crystal orientations were not known in these ultrasonic experiments, only the combination $R\Lambda$ could be determined for each crystal, not the dislocation density $\Lambda$ itself. Both Iwasa *et al.* (1979) and Beamish and Franck (1982) assumed exponential distributions of loop lengths with average length $L$ and dislocation density $\Lambda$

$$N(l) = \frac{\Lambda}{L^2} e^{-l/L}. \tag{12}$$

The temperature dependence in these equations comes from the damping parameter $B$. In an insulating crystal like helium, the main damping source is thermal phonons, via the fluttering mechanism described by Ninomiya (1974). This has a characteristic $B = gT^3$ temperature dependence, with $g$ given in eqn. 4. At the MHz frequencies of ultrasonic measurements, the damping term $B\omega/A$ in eqns. 8 and 9 is large near melting. At high temperatures the dislocations' motion is heavily damped and their contributions to the sound velocity and attenuation are small, as seen in Figs. 17 and 18. This means that elastic constants measured near samples' melting points, such as those listed in Table I, are the intrinsic values.

Dislocation parameters extracted from fits to the ultrasound velocities and attenuations were similar in hcp $^4$He and $^3$He, and in bcc $^3$He. In most crystals the average loop lengths $L$ were between 3 and 12 $\mu$m, while the dislocation densities $\Lambda$ (assuming $R$ =0.1) ranged from $2\times10^3$ to $10^6$ per cm$^2$. Lengua and Goodkind (1990) found similar dislocation densities in hcp $^4$He crystals grown at low pressures, but with longer loops. A range of dislocation densities and lengths in different experiments is expected, given the inevitable variations in crystal quality. Higher dislocation densities would be expected in, for example, polycrystals grown with the blocked capillary technique. However, the large sound scattering and attenuation makes ultrasonic measurements difficult in polycrystals, and there have been no comparable measurements of their dislocation parameters.

Although dislocation effects are small at high temperatures, Tsuruoka and Hiki (1979) tried to extract dislocation densities from ultrasonic attenuation measurements in hcp $^4$He crystals near their melting temperatures. Their calculated dislocation densities were orders of magnitude larger than in other ultrasonic measurements, up to $6\times10^9$/cm$^2$. However, they used a very different method to analyze their attenuation data and subsequent reanalysis (Paalanen *et al.*, 1981) showed that their attenuation values were consistent with the much smaller dislocation densities found in other experiments.

Although the temperature dependence of the sound velocity and attenuation anomalies is due to the thermal damping of dislocation motion, the resonance and strong frequency dependence at ultrasonic frequencies makes it impossible to confirm the phonon fluttering prediction of Ninomiya (1974) by directly measuring the temperature dependence of the damping $B$. However, it is clear from the ultrasonic measurements that the damping increases with temperature and the temperature dependence is consistent with a temperature dependence $B = gT^n$, with $n$ between 2 and 4, and with a value of $g$ similar that predicted by eqn. 4.

When high concentrations of isotopic impurities were added to helium crystals, as in Figs. 13 and 14, the dislocation anomalies were eliminated since impurities bind to edge dislocations at low temperatures, pinning them and eliminating their contributions to the ultrasound velocity and attenuation (Beamish and Franck, 1983; Iwasa

and Suzuki, 1980). As expected, the effects of impurities were strongly amplitude dependent, since stress-induced breakaway from impurity pinning sites allows dislocations to move at large ultrasonic amplitudes. Analysis of the amplitude and temperature dependence of this unpinning provided estimates (Iwasa and Suzuki, 1980) of the impurity binding energies (∼0.3 K) and the forces required to detach such an impurity from a dislocation (∼$10^{-14}$ N). Given their weak binding to dislocations, isotopic impurity atoms are effective pinning sites only at low temperatures and for small stress amplitudes.

The impurity concentrations for the crystals of Figs. 17 and 18 (<1 ppm $^3$He and 1.35 ppm $^4$He, respectively) were not sufficient to pin the dislocations, even at the lowest temperatures of these measurements. However, recent ultrasonic measurements did observe pinning below 200 mK in hcp $^4$He crystals containing 0.3 ppm of $^3$He mK (Iwasa and Kojima, 2017). As described in the next sections, measurements at low frequencies show qualitatively similar behavior, but the modulus changes are much larger and imply longer dislocations loops and stronger $^3$He impurity binding. Recent low frequency measurements like those on single crystals described in Section V.C. are much more direct and straightforward to interpret, and allow dislocation parameters to be determined more reliably than from the ultrasonic measurements.

## V. LOW FREQUENCY ELASTIC MODULUS AND DISSIPATION

The effects of dislocations on ultrasound propagation are complicated, since dislocations' inertia, string tension and damping are all important at MHz frequencies. Measuring the resulting frequency dependence is difficult, since most ultrasonic measurements are limited to a few frequencies, multiples of the fundamental resonance of the transducers. Also, crystals are anisotropic, with longitudinal and transverse modes, so the directions of the stresses acting on dislocations are often unknown. Even if a crystal's orientation is independently determined, ultrasonic stress amplitudes are difficult to estimate and are seldom accurately known.

At low frequencies, well below the resonance frequency of eqn. 6, dislocation effects are much simpler to interpret. The inertial term in eqn. 5 can be neglected, and the damping term is small. The elastic changes due to dislocations can be much larger than at ultrasonic frequencies, since all the dislocations move in phase with the applied stress and contribute to the softening of the crystal. In the static (zero frequency) limit, the dislocations reduce the intrinsic shear modulus $\mu_0$ by an amount

$$\frac{\delta\mu}{\mu_0} = \frac{\alpha\Lambda L^2}{1+\alpha\Lambda L^2}. \qquad (13)$$

Here $\alpha$ is a numerical factor (∼0.05) that includes the orientation factor $R$, to account for the component of the stress in the dislocations' glide directions and the logarithmic term in eqn. 3, which depends on the dislocations' core size and separation. Long dislocations have a larger effect than short ones, but the dislocation density $\Lambda$ and the pinning length $L$ cannot be separately determined from eqn. 13. Only the combination $\Lambda L^2$, which reflects the geometry of the dislocation network, can be found from low frequency modulus measurements. For example, a simple cubic network of dislocations with $\Lambda L^2 = 3$, would reduce the low frequency shear modulus by more than 10%. Additional pinning, e.g. by impurities or jogs, reduces the effective dislocation loop length and consequently the magnitude of shear modulus softening.

At finite frequencies, dislocation damping produces elastic dissipation. For frequencies $\omega$ well below the dislocation lines' resonance, the inertial term in eqn. 5 can still be neglected, but the damping term introduces a relaxation time $\tau = BL^2/\pi^2 C$. For $\omega\tau \ll 1$, the shear modulus is still given by eqn. 13, but the dissipation becomes

$$\frac{1}{Q} = \frac{\delta\mu}{\mu_0}\omega\tau = \frac{\delta\mu}{\mu_0}\omega\frac{BL^2}{\pi^2 C}. \qquad (14)$$

The dissipation $1/Q$ depends on $L$ more strongly than the modulus change. If both can be measured, and the damping coefficient $B$ is known, then $L$ and $\Lambda$ can be separately determined.

### A. Early measurements

A number of experiments used frequencies in the kHz range to study the elastic modulus and dissipation in helium crystals. Tsymbalenko (1978, 1979, 1984, 1986) used quartz resonators embedded in solid helium to measure its shear modulus and internal friction. Typical results, measured at 80 kHz, are shown in Fig. 19 for four different hcp $^4$He single crystals grown at 3.5 MPa (dotted and dashed curves labeled 1, 3, 4 and 5). Dislocations are the only defects that can explain the large shear modulus changes, up to 30%, which correspond to $\Lambda L^2 \sim 5$. The solid lines in Fig. 19 are a fit of the dislocation model described by eqns. 8 to 11 to the data for crystal 4. The measured modulus changes are orders of magnitude larger the changes observed in ultrasonic measurements so longer loops, $L$ ∼100 $\mu$m, were needed to fit the modulus and dissipation data. The shear modulus (left panel) and the decrement (right panel) both decreased below 1 K, confirming that dislocations were more mobile and less damped at low temperatures. The temperature dependence was consistent with a damping $B = gT^n$, with an exponent $n$ close to 3, but to get satisfactory fits it was necessary to include the inertial term in eqn. 5.

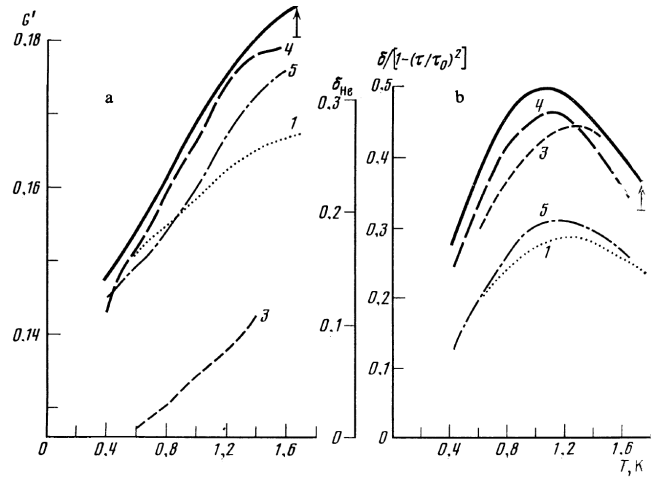


FIG. 19 Shear modulus $G$ (left panel) and decrement $\delta_{He} \propto 1/Q$ (right panel) for hcp $^4$He single crystals grown at 3.5 MPa. The dotted and dashed curves (labeled 1, 3, 4, and 5) are data for four different crystals grown under the same conditions. The solid curves are dislocation fits to the data of crystal 4. Reproduced from Tsymbalenko (1984), with the permission of AIP Publishing

Paalanen *et al.* (1981) studied helium's elastic properties at an even lower frequency (331 Hz), using a torsional oscillator technique. In contrast to torsional oscillators used to search for supersolidity, this oscillator's inertial element did not contain helium. The torsion rod, however, was filled with solid helium, whose shear modulus and dissipation were determined from the frequency and quality factor of the torsional oscillator. As shown in the top panel of Fig. 20, the shear modulus changed by up to 40% when the solid was cooled, from which the authors inferred that $\Lambda L^2 = 2$. However, the modulus *increased* at low temperatures, implying that dislocations were less mobile at low temperatures, in contrast to the 30% *decrease* in the 80 kHz measurements of Tsymbalenko (1984). The changes in shear modulus were accompanied by dissipation peaks (lower panel). Both the modulus and dissipation depended strongly on the strain amplitude and on the $^3$He concentration. The low temperature stiffening in Fig. 20 is consistent with impurity pinning, with an amplitude dependence and hysteresis due to stress-induced breakaway of dislocations. From the temperature dependence of the breakaway amplitude, Paalanen *et al.* (1981) deduced an impurity binding energy $E_B$=0.7 K.

There was some uncertainty in the $^3$He impurity concentration in the sample of Fig. 20. It was described as "commercial $^4$He", but its unpinning temperatures were higher than in other samples, suggesting larger impurity concentrations. The authors described it as having $^3$He concentrations "probably less than 3 ppm", about ten times larger than is usually found in commercial helium gas. In their samples with very low $^3$He concentrations ($x_3 = 2.4\times10^{-9}$) the shear modulus, shown in the upper panel of Fig. 21, was independent of temperature, as expected if there is no impurity pinning. The dissipation in the isotopically pure samples, shown in the lower panel of Fig. 21, was relatively small, without the impurity breakaway peaks of Fig. 20. In the sample whose data are shown as solid symbols, the shear modulus was small, indicating that the dislocations were mobile. The corresponding dissipation increased roughly as $T^2$, weaker than the $T^3$ dependence noted by Tsymbalenko, but the fits to the dissipation were made over different temperature ranges. The other high purity sample, corresponding to the open symbols, had a larger shear modulus and negligible dissipation, indicating that dislocation effects were much smaller in this sample, likely because of its orientation. Paalanen *et al.* (1981) showed that their high temperature dissipation values at 331 Hz were consistent with those from earlier work by Tsymbalenko (1978) at 15 kHz and of Tsuruoka and Hiki (1979) at MHz ultrasonics frequencies, with no need for the large dislocation densities assumed in the latter paper.

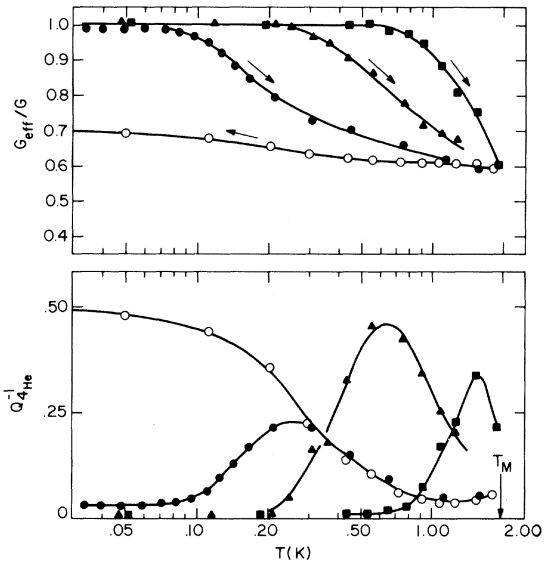


FIG. 20 Torsional oscillator measurements of the normalized shear modulus (upper panel) and dissipation (lower panel) in an hcp $^4$He polycrystal at 3.7 MPa. The measurement frequency was 331 Hz and the data were taken at strain amplitudes $\epsilon = 10^{-7}$ (squares), $\epsilon = 6\times10^{-7}$ (triangles) and $\epsilon = 10^{-5}$ (circles) (Paalanen *et al.*, 1981).

The low frequency measurements were consistent with many features observed in ultrasonic experiments. They confirm that dislocations can soften the shear modulus, are thermally damped at high frequencies and temperatures, and are pinned by $^3$He impurities at low temperatures and stresses. There are, however, significant differences between the low and high frequency results. Mod-

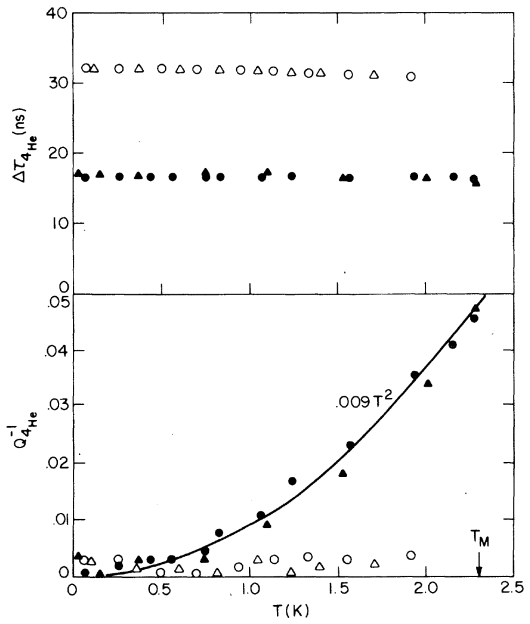


FIG. 21 Torsional oscillator measurements of the period shift, proportional to the shear modulus change, (upper panel) and dissipation (lower panel) for isotopically pure ($x_3$ =2.4 ppb) hcp $^4$He crytals at 4.8 MPa. Open and closed symbols correspond to two samples with different orientations. The measurement frequency was 331 Hz and the data were taken at strain amplitudes $\epsilon = 6\times10^{-7}$ (triangles) and $\epsilon = 10^{-5}$ (circles) (Paalanen *et al.*, 1981).

ulus changes are much larger in the low frequency measurements, up to 40%, compared to less than 1% in ultrasonic measurements. Some of this difference is due to the inertial effects that limit dislocation motion at MHz frequencies. However, the values extracted for the dislocation network parameter $\Lambda L^2$ were much smaller in the ultrasonic measurements (between ∼0.001 and 0.1) than in the low frequency measurements of Paalanen *et al.* (1981) and Tsymbalenko (1984) (between ∼2 and 6). The extracted dislocation densities $\Lambda$ were comparable in the ultrasonic measurements and the 80 kHz measurements of Tsymbalenko (1984) (∼$10^4$ to $10^5$/cm$^2$ and ∼$10^4$/cm$^2$, respectively) but the pinning lengths were very different, ∼5 $\mu$m in the ultrasonic measurements vs. ∼100 $\mu$m in the measurements of Tsymbalenko (1984). Some discrepancies are expected since the crystal qualities may be different in the various experiments, but the large differences in $\Lambda L^2$ and $L$ are puzzling. Also, although the thermal damping in all the experiments appeared to be proportional to $T^n$, with $n$ between 2 and 4, the magnitude of the damping $B$ was about two orders of magnitude larger in the measurements of Tsymbalenko (1984). This is surprising, since $B$ is an intrinsic property of individual dislocations and should not depend on their density or lengths. More direct and detailed recent measurements of damping in single crystals, described in Section V.C., show similar large modulus changes, but are not consistent with the $B$ values of Tsymbalenko (1984), instead confirming the expected phonon scattering damping $B$.

This torsional oscillator technique has also been used to study dislocation effects in bcc $^3$He. Miura *et al.* (2000a,b, 1998) observed a dissipation proportional to $T^3$, and shear modulus decreases as large as 60% at high temperature, suggesting that $\Lambda L^2$ was at least as large as in hcp $^4$He. However, they were not able to determine the dislocation densities or lengths separately.

### B. Shear modulus measurements in polycrystals

To resolve discrepancies between the dislocation parameters determined by the high and low frequency measurements, unambiguous measurements of the thermal damping coefficient $B$ were needed. As noted by Tsymbalenko (1978), this requires measurements over a wide range of frequencies. However, this is not practical with resonant techniques like torsional oscillators and quartz resonators, nor with ultrasonic methods. Non-resonant techniques allow the frequency to be varied continuously but are usually less sensitive. However, with modern electronics that takes advantage of the reduced noise levels at low temperatures, extremely sensitive non-resonant measurements can be made on solid helium.

The low frequency shear modulus of polycrystalline hcp $^4$He has been measured by Day and Beamish (2007b) using such techniques. Helium crystals were grown in a narrow gap ($D$ =180 $\mu$m) between two parallel shear piezoelectric transducers. A voltage $V$ applied to one transducer generated a shear displacement $\delta x$ and a uniform shear strain $\epsilon = \delta x/D$ in the helium. This produced a shear stress $\sigma$ and a corresponding charge $q$ on the opposite transducer, allowing the shear modulus of the solid helium, $\mu = \sigma/\epsilon$ to be calculated. To determine absolute rather than relative values, the transducers were calibrated at the low temperatures of the measurements (Bukhari *et al.*, 2014; Islam and Beamish, 2018). For *ac* measurements, a lock-in amplifier also gave the dissipation in the helium, which is related to the measured phase lag $\phi$ between the stress and strain, $1/Q = \tan\phi$. With this technique, the measurement frequency could be varied continuously up to 16 kHz, limited only by mechanical resonances of the pressure cell and acoustic resonances of the solid helium inside it. The lower frequency limit, of order one Hz, was set by noise in the stress measurements. Using this technique, which had a stress resolution of $2\times10^{-6}$ Pa at the highest frequencies, solid helium's shear modulus was measured at frequencies from 0.5 Hz to 16 kHz (Haziot *et al.*, 2013b; Syshchenko *et al.*, 2010), and at strains as low as $2\times10^{-11}$ (Haziot *et al.*, 2013c).

Figure 22 (a) shows the changes in the shear modulus of an hcp $^4$He sample with a nominal $^3$He impurity con-

centration of 300 ppb ($300 \times 10^{-9}$). The polycrystalline solid was grown using the blocked capillary technique, with a final pressure of 3.33 MPa (Day and Beamish, 2007b). The shear modulus was essentially constant between the melting temperature (1.86 K) and 200 mK, then increased at lower temperatures, reaching the solid's intrinsic value at the lowest temperatures (Day *et al.*, 2009). The total change, about 8%, is somewhat smaller than the dislocation softening seen in some earlier low frequency measurements on helium single crystals and corresponds to a network with $\alpha \Lambda L^2 \approx 0.09$ (eqn. 13). The temperature at which the softening occurred depended on the measurement frequency, as shown in Fig. 22 (a) for frequencies of 20, 200 and 2000 Hz. It was also very sensitive to the $^3$He impurity concentration, as shown in Fig. 22 (b) for 3.3 MPa crystals with $x_3$=1, 85 and 300 ppb. The measurements in Figs. 22 (a) and (b) were made at very small shear strains ($\epsilon = 3\times10^{-9}$, corresponding to stress $\sigma \approx 0.05$ Pa). As shown in Fig. 22 (c), the low temperature shear stiffening was reduced at strains above $2\times10^{-8}$. However, the shear modulus above 200 mK was essentially independent of the strain amplitude.

This is the behavior expected for a network of dislocations that are pinned by weakly bound $^3$He impurities at low temperatures. For a binding energy $E_B$, the equilibrium concentration of $^3$He atoms along the dislocation is $x_3^{dis} = x_3\ e^{\frac{E_B}{k_B T}}$. At high temperature, the $^3$He atoms unbind and the impurity pinning length $L_i$, which is inversely proportional $x_3^{dis}$, increases. When $L_i$ becomes comparable to the network length $L_N$, the dislocations are able to move and reduce the crystal's intrinsic shear modulus. In Fig. 22 (a) this occurs around 200 mK, but the pinning length, and hence the softening temperature, depends on the sample's $^3$He concentration, as shown in Fig. 22 (b). Assuming the three samples had similar network lengths, this allows the $^3$He binding energy to be estimated as $E_B \approx 0.7$ K, consistent with the value from Paalanen *et al.* (1981). The amplitude dependence in Fig. 22 (c) reflects dislocations breaking away from $^3$He pinning sites when the force exerted by the applied stress exceeds a threshold. In the high temperature regime, where impurity pinning can be neglected, the shear modulus is independent of the stress amplitude, because the network pinning is much stronger.

The frequency dependence of the softening shown in Fig. 22 (a) can be well described by a thermally activated relaxation process. The activation energy, 0.7 K, is essentially the same as expected if, for example, the dislocation unpinning rate is controlled by thermally activated unbinding of impurities. Alternatively, bound impurities might move with dislocations and produce a damping force proportional to their density, giving the same activation energy.

The behavior is similar in $^3$He (West *et al.*, 2009). Figure 23 shows the normalized shear modulus for an hcp $^3$He polycrystal at a pressure of 11.9 MPa. The temperature at which the modulus softens was higher than in hcp $^4$He, which is expected given the larger impurity concentration in the $^3$He sample ($x_4$=1.35 ppm). As for $^4$He, the stiffening shifted to lower temperature and disappeared at large strains, with a similar threshold for breakaway. Neither the dependence on frequency nor on impurity concentration was measured in these experiments, so the $^4$He impurity binding energy could not be determined, but ultrasonic experiments extracted similar isotopic impurity binding energies in hcp $^3$He and $^4$He crystals. For the bcc phase of $^3$He, dislocation effects were not obvious but were seen more clearly in subsequent experiments (Cheng *et al.*, 2016).

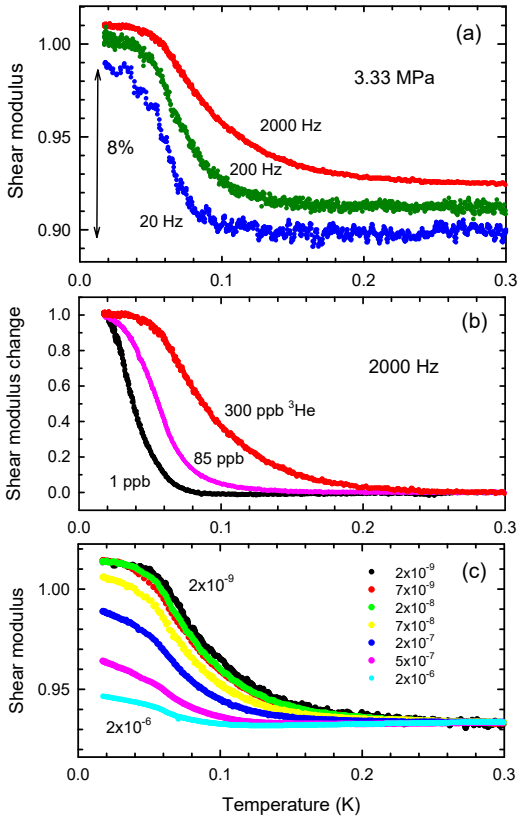


FIG. 22 Shear modulus in a hcp $^4$He polycrystal at 3.33 MPa. (a) normalized modulus at low strain $\epsilon = 3\times10^{-9}$ for frequencies of 20, 200 and 2000 Hz (b) shear modulus changes at low strain for samples with different $^3$He impurity concentrations, normalized to the total changes from low to high temperature for each sample (c) amplitude dependence of the shear modulus at 2000 Hz for strains (from top to bottom) between $2\times10^{-9}$ (top curve, black symbols) and $2\times10^{-6}$ (bottom curve, cyan symbols).

The origin of the modulus changes in solid helium was confirmed by the effects of annealing, which is expected

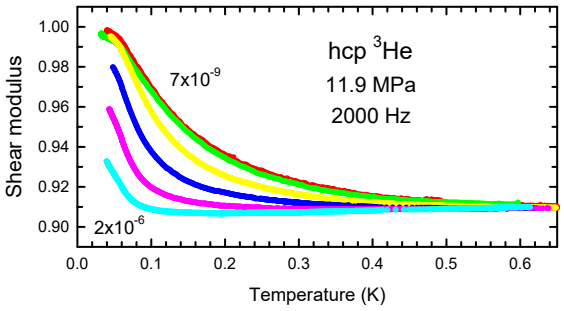


FIG. 23 Amplitude dependence of the shear modulus in a hcp $^3$He polycrystal at 11.9 MPa measured at 2000 Hz. The modulus is normalized to the value at the lowest temperature and strain. Strain amplitudes for the different curves vary (from top to bottom) from $7\times10^{-9}$ (top curve, red symbols) to $2\times10^{-6}$ (bottom curve, cyan symbols) with the same strain values as the corresponding curves in Fig. 22.

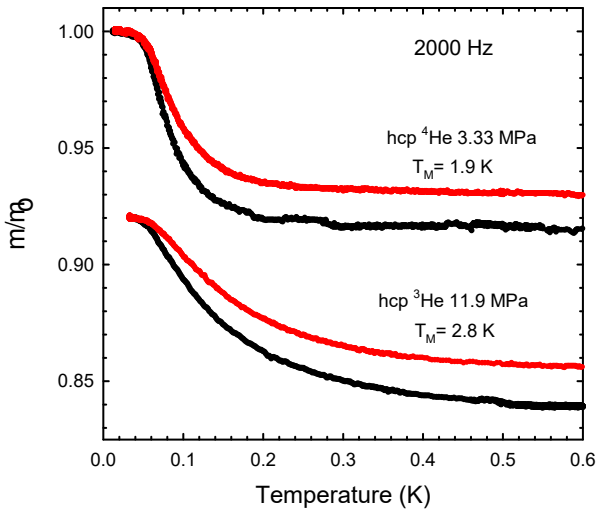


FIG. 24 Effect of annealing on the shear modulus softening in helium polycrystals (Day *et al.*, 2009). The upper pair of curves shows the normalized modulus at 2000 Hz for hcp $^4$He containing 0.3 ppm $^3$He impurities at a pressure of 3.33 MPa (33.3 bar). The lower pair of curves are for hcp $^3$He containing 1.35 ppm $^4$He impurities at 11.9 MPa (119 bar). For each sample, the lower (black) set of data is before annealing; the upper (red) data is after annealing.

to reduce the density of defects like dislocations. Figure 24 shows the shear modulus changes for hcp $^4$He (upper pair of curves) and hcp $^3$He (lower pair of curves). Samples were frozen using the blocked capillary technique, which produces samples with many grain boundaries and dislocations. The lower (black) set of data in each pair of curves in Fig. 24 was measured when the samples were first cooled, immediately after freezing. The modulus changes were similar in the 3.33 MPa $^4$He sample and the 11.9 MPa $^3$He sample, about 8% in each case (Day *et al.*, 2009). When the samples were annealed for several hours near their melting temperatures, their shear moduli increased by 1 or 2 percent. However, when an annealed sample was subsequently cooled (upper red set of data in each pair of curves), its shear modulus returned to the pre-annealing value at the lowest temperature, as expected when dislocations are completely pinned by impurities. This confirmed that the values at the lowest temperatures reflect the intrinsic shear moduli of perfect crystals, unaffected by the now immobile dislocations. The changes in the dislocation network during annealing reduced the high temperature softening by about 20%. However, this is not a direct measure of dislocation densities since the modulus change is proportional to $\Lambda L^2$. A decrease in density $\Lambda$ is usually accompanied by an increase in the network length $L$, which reduces the modulus change due to annealing, or can even change its sign (Day *et al.*, 2009).

Large stresses can also change the dislocation network (Cheng and Beamish, 2018b; Day *et al.*, 2009). Figure 25 compares the shear moduli of hcp $^4$He samples with $^3$He impurity concentrations of 300 ppb (upper pair of curves) and 1 ppb (lower set of three curves). As for the helium crystals of Fig. 24, the initial shear modulus of the high purity (1 ppb $^3$He) sample (lowest curve, black symbols) increased after annealing (middle of the three curves, red symbols), but returned to the same intrinsic value at the lowest temperature. When large acoustic strains ($\epsilon \sim10^{-4}$) were applied to the annealed sample at low temperatures, the shear modulus did not change. However, when the stressed sample was then warmed (uppermost of the three curves, blue symbols) the modulus behavior was different - it was clear that the large stresses had affected the dislocation network. The upper pair of curves show the same effect in a sample with a higher $^3$He concentration. Counterintuitively, applying the large stresses reduced the softening due to dislocations. This suggests that the effect of the low temperature stresses was to partially pin existing dislocations, rather than creating new ones. Warming above 0.5 K reversed the effects of the acoustic stress and repeating the process gave reproducible hysteresis loops. The ease with which the stress effects were annealed suggests that the new pinning sites may be jogs, which can be removed by dislocation climb when thermal vacancies are available (Hull and Bacon, 2011).

Even at lower stresses, where new dislocations and jogs are not created, stress-induced breakaway from impurity pinning sites leads to hysteresis when the strain amplitude is cycled (Granato and Lücke, 1981). Fig. 26 shows a hysteresis loop for hcp $^4$He at 36 mK (Day *et al.*, 2010). The open symbols show the increase in normalized shear modulus when the strain amplitude $\epsilon$ was reduced from $4\times10^{-6}$ (where dislocations have broken away from $^3$He

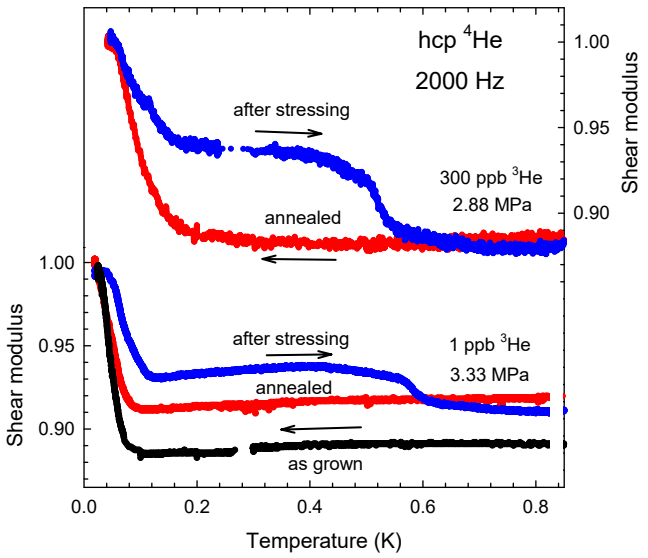


FIG. 25 Effects of stressing and annealing on the shear modulus of hcp $^4$He with 300 ppb $^3$He (2.88 MPa, upper pair of curves) and with 1 ppb $^3$He (3.33 MPa, lower set of three curves). For each sample, the modulus is normalized to the value at the lowest temperature. The various curves are discussed in the text (Day *et al.*, 2009).

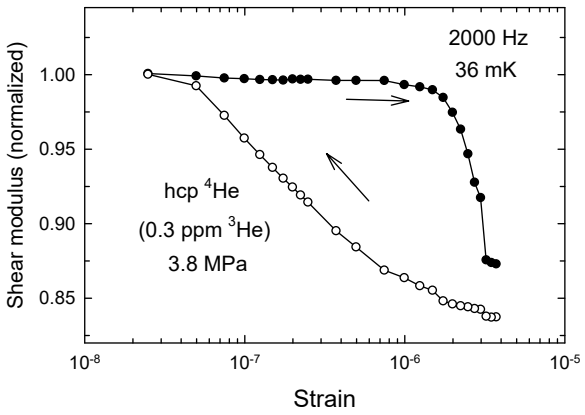


FIG. 26 Low temperature hysteresis due to impurity pinning and unpinning in hcp $^4$He at 3.8 MPa (Day *et al.*, 2010). Open symbols show the shear modulus measured while decreasing the strain; solid symbols are data taken while increasing the strain.

impurities) to $2\times10^{-8}$ (where they are pinned). When the strain amplitude was then increased (solid symbols), the shear modulus remained at its large intrinsic value up to strains of about $10^{-6}$, then dropped rapidly. This type of hysteresis arises because the force pulling a dislocation away from an impurity increases with the distance between pinning points, as well as with the applied stress (Iwasa, 2013; Kang *et al.*, 2015). At sufficiently high stress, dislocations are free of bound $^3$He so this loop length is that between nodes of the dislocation network. If the stress amplitude is gradually reduced below the critical value, $^3$He atoms can bind to dislocations, beginning with the shortest loops. This reduces the distance between pinning sites, which allows more $^3$He atoms to bind and quickly immobilizes this dislocation loop. As the strain amplitude is reduced, successively longer loops are pinned and the distribution of network lengths can be inferred from the amplitude dependence of the shear modulus (the open circles in Fig. 26). The hysteresis arises because when one begins at low strain, the bound impurities are closely spaced and do not break away unless much larger stresses are applied. A lower limit on the time required to pin dislocations at low temperature can be inferred from the fact that the impurities do not pin the dislocations during the part of the ac cycle when the stress goes through zero. The pinning time must be longer than this millisecond scale.

At higher temperatures, where the unpinning from impurities is thermally assisted (Lücke *et al.*, 1968), Kang *et al.* (2013) showed that the hysteresis decreased rapidly, disappearing around 70 mK. The combination of amplitude and temperature dependence produces complicated elastic behavior that Kang *et al.* (2013) summarized in the stress-temperature "hysteresis map" for polycrystalline hcp $^4$He shown in Fig. 27.

Similar behavior was seen in torsional oscillator measurements (Pratt *et al.*, 2011), where the amplitude dependence was interpreted as a velocity dependence, rather than a stress dependence. However, it is now clear that these and other torsional oscillator experiments were actually probing the shear modulus of solid helium, not inertial effects that might signal supersolidity (Beamish *et al.*, 2012). The connection between a torsional oscillator's frequency and damping and helium's elastic properties has been directly confirmed in experiments in which the solid helium's shear modulus was measured simultaneously using piezoelectric transducers inside the torsional oscillator (Kim *et al.*, 2011; Shin *et al.*, 2016).

The frequency dependence of the shear modulus seen in Fig. 22 (a) is mirrored in the corresponding dissipation $1/Q$. Figure 28 shows the low amplitude shear modulus and dissipation for an hcp $^4$He polycrystal, measured at frequencies between 2 and 2000 Hz (Syshchenko *et al.*, 2010). The open circles in Fig. 28 mark the midpoints of the modulus change and the positions of the accompanying dissipation peaks. The dissipation peaks coincide with the midpoints of the modulus softening, as expected for a Debye relaxation process. They shift to higher temperatures with increasing frequency, suggesting that the relaxation process is thermally activated. This is confirmed by the Arrhenius plots of Fig. 29, where the softening midpoint and dissipation peak positions are shown

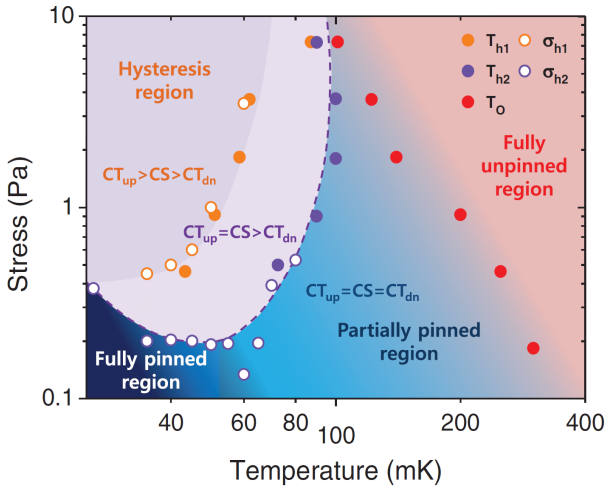


FIG. 27 Stress-temperature map of solid $^4$He from shear modulus measurement (Kang *et al.*, 2013).

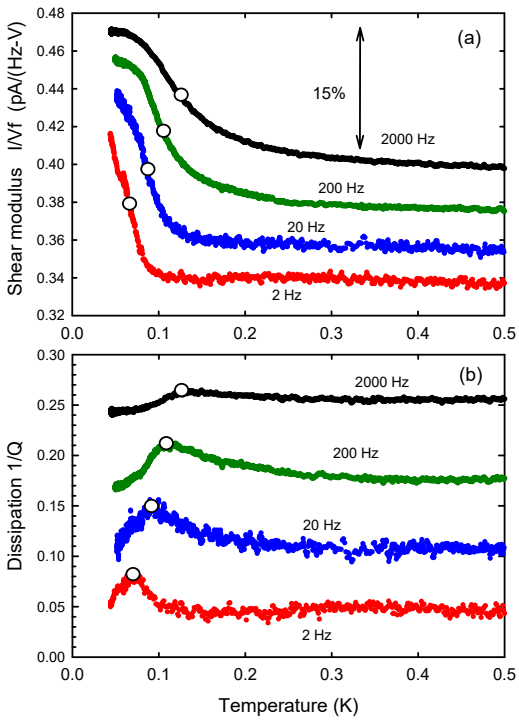


FIG. 28 (a) Shear modulus in an hcp $^4$He polycrystal at 3.8 MPa, for frequencies between 2 and 2000 Hz. Circles mark the midpoints of the modulus softening. (b) Corresponding dissipation, with circles marking the peak values. Curves have been vertically shifted for clarity. (Syshchenko *et al.*, 2010)

for the samples of Fig. 22 (a) and Fig. 28. The slopes, shown by solid lines, correspond to activation energies of approximately 0.7 K, consistent with the binding energy estimated from the $^3$He impurity concentration dependence.

For a Debye process with relaxation time $\tau$ and a small relaxation strength $\frac{\delta\mu}{\mu_0} \ll 1$, the modulus and dissipation are given by (Nowick and Berry, 1972)

$$\frac{\mu}{\mu_0} = 1 - \frac{\delta\mu}{\mu_0}\frac{1}{1+(\omega\tau)^2} \tag{15}$$

$$\frac{1}{Q} = \frac{\delta\mu}{\mu_0}\frac{\omega\tau}{1+(\omega\tau)^2} \tag{16}$$

where $\mu_0$ is the "unrelaxed modulus" ($\omega\tau \gg 1$) and $\mu_0 - \delta\mu$ is the "relaxed modulus" ($\omega\tau \ll 1$). For dislocations the relaxation time could, for example, be the one associated with their damping by thermal phonons, $\tau = BL^2/\pi^2 C$. Other relaxation processes could be thermally activated, with $\tau(E) = \tau_0 e^{E/T}$ where $E$ is the activation energy. The midpoint of the modulus crossover and the dissipation maximum occur at the temperature where $\omega\tau = 1$. However, a Debye relaxation with a single activation energy (0.73 K) and an attempt time $\tau_0$ (25 ns), the values suggested by Fig. 29, gives a shear modulus crossover and dissipation peak (dashed blue lines) much narrower than were observed, as shown in Fig. 30 (Syshchenko *et al.*, 2010). The measured dissipation peak was also much smaller than the expected Debye value $(1/Q)_{peak} = \frac{1}{2}\delta\mu/\mu_0$. However, the broadening of the shear modulus crossover and dissipation could be explained if the relaxation process involved a distribution of activation energies rather than a single value. The solid red lines in Fig. 30 show a fit to the data with a distribution of activation energies with width $W = 0.45$ around an average value of 0.73 K. Mukharsky and Penzev (2012) and Mukharsky *et al.* (2009) observed similar behavior in measurements of uniaxial compression of polycrystalline $^4$He between 10 Hz and 4 kHz. The temperature and frequency dependences were similar to those of the shear modulus, as were the activation parameters ($E \approx 0.62$ K, $W \approx 0.71$). This is expected since uniaxial compression involves shear deformations and so is affected by dislocation motion in the same way.

Kang *et al.* (2015) have shown that the complete temperature and stress dependence, including the hysteresis when the stress amplitude is cycled, could be quantitatively reproduced with a Granato-Lucke dislocation model that included impurity pinning and a distribution of network lengths. The lower panels of Fig. 31 show their measured shear modulus and dissipation in hcp $^4$He at a frequency of 1000 Hz. The calculated values shown in the upper panels (for a dislocation density $R\Lambda = 2\times10^{-6}$ cm$^{-2}$ and network length $L = 5$ $\mu$m) agreed very well with the data. The $^3$He binding energy used to fit the data, $E = 0.3$ K, was smaller than inferred from the frequency dependence in Figs. 22 and 29, but was based on data at a single frequency. Their model did not include a distribution of activation energies, which broadens the modulus crossover and the dissipation peak, mimicking

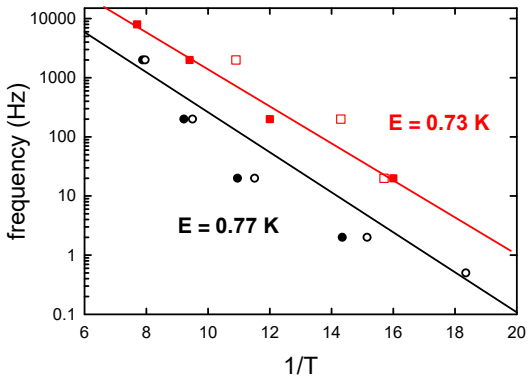


FIG. 29 Arrhenius plot of the crossover temperatures for the 3.8 MPa sample of Fig. 28 (lower black symbols and line) and the 3.3 MPa sample of Fig. 22 (a) (upper red symbols and line). Open symbols are the midpoints of the shear modulus softening; solid symbols are the dissipation peak maxima (Syshchenko *et al.*, 2010).

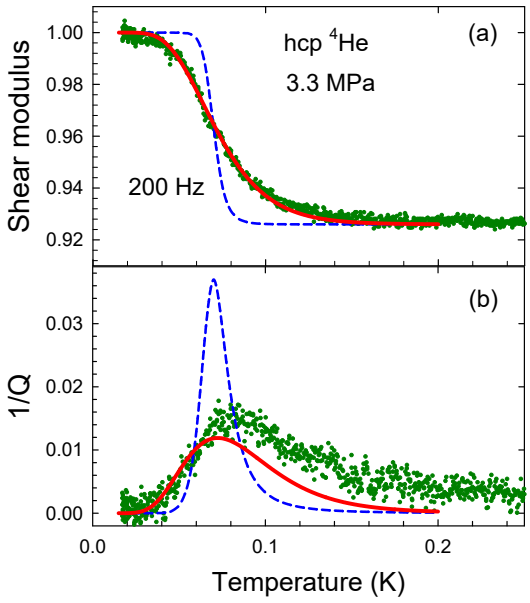


FIG. 30 Debye relaxation fits of (a) the normalized shear modulus and (b) the dissipation at 200 Hz in the 3.3 MPa $^4$He sample of Fig. 29 .Dashed blue line is the fit for a single activation energy $E_B$ =0.73 K. Solid red line is a fit using a distribution of activation energies.

a smaller activation energy.

As shown in Figs. 22 to 24, the shear modulus changes are similar in the hcp phases of $^3$He and $^4$He. However, the dynamics of dislocation motion were significantly different in hcp $^3$He (Cheng and Beamish, 2017). In contrast to $^4$He, the shear softening in hcp $^3$He was independent of frequency, as shown in Fig. 32 (a). This suggests

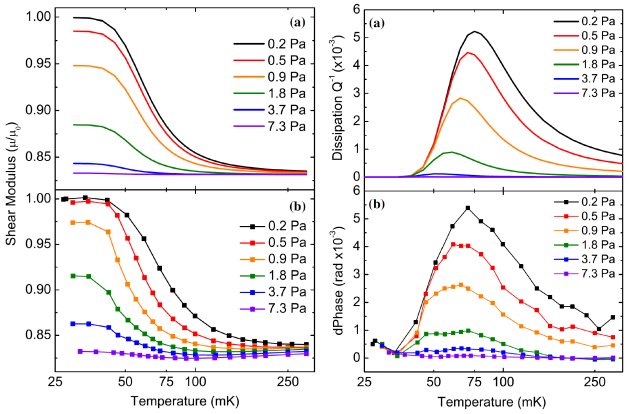


FIG. 31 Shear modulus (left panel) and dissipation (right panel) for an hcp $^4$He polycrystal at 3.9 MPa, measured at 1000 Hz and stresses between 0.2 and 7.3 Pa. Upper panels (a) are values calculated using an impurity binding energy distribution as described in the text. Lower panels (b) are measured values (Kang *et al.*, 2015). Curves are ordered top to bottom as in the corresponding legends for each panel. ©(1977) The Physical Society of Japan.

that in hcp $^3$He, the $^4$He impurities act as static pinning sites over the full frequency range, 22 to 5402 Hz. This is different from the dynamic impurity behavior in hcp $^4$He, where $^3$He impurities appear to move with dislocations, damping their motion and producing the strong frequency dependence seen in the shear modulus and dissipation of Fig. 32 (b). However, the shear modulus in hcp $^4$He single crystals is also frequency independent at high frequencies, when dislocation speeds exceed about 45 $\mu$m/s (Haziot *et al.*, 2013b) and the $^3$He impurities cannot move fast enough to follow the dislocations. The essentially static nature of impurity pinning in hcp $^3$He at frequencies as low as 22 Hz is consistent with the lower mobility of impurities in hcp $^3$He, where disorder in the $^3$He spins prevents impurities from propagating ballistically. At sufficiently low frequencies and strains, diffusive motion of $^4$He impurities should allow them to move with the dislocations in solid $^3$He, like the dragging of the Cottrell atmosphere of impurities around dislocations in classical crystals (Takeuchi and Argon, 1979). The expected frequency dependence would occur in a regime below that shown in Fig. 32 (a).

The dissipation in hcp $^3$He, shown in Fig. 32 (b) was also quite different from that in hcp $^4$He. As expected for static pinning, the thermally activated dissipation peak associated with impurity unpinning in hcp $^4$He was absent in hcp $^3$He, or at least greatly reduced. Instead, the dissipation in $^3$He extended over a broad temperature region. When the frequency was lowered, the magnitude of the dissipation increased rapidly and its broad maximum shifted to higher temperatures, the opposite direction to that of thermally activated relaxation peaks

like those in hcp $^4$He. This behavior suggests that the dissipation in hcp $^3$He is not due to a damping force proportional to the dislocation speed, as in the Granato-Lucke equation 5. Instead, Cheng and Beamish (2017) proposed that the dissipation may be due to a velocity-independent, friction-like energy loss associated with rearrangements of spin configurations when a dislocation moves through $^3$He. However, initial measurements on bcc $^3$He polycrystals (Cheng *et al.*, 2016) show frequency dependent shear modulus changes and dissipation peaks that resemble those in hcp $^4$He. This suggests that $^4$He impurities are much more mobile in the bcc phase, despite the much larger spin exchange energies in bcc $^3$He (Ceperley and Jacucci, 1987). However, dislocation structures and mobilities in bcc structures are very different from those of hcp crystals, e.g. they are usually not split into partials and often have significant Peierls barriers to gliding. Unfortunately, the narrow temperature range for the bcc phase of $^4$He means that there is no way to directly compare the low temperature behavior of dislocations in bcc $^3$He to that in bcc $^3$He.

Although many features of dislocation motion in helium are clear from these experiments on polycrystals, more detailed and quantitative information can be obtained from similar measurements on single crystals.

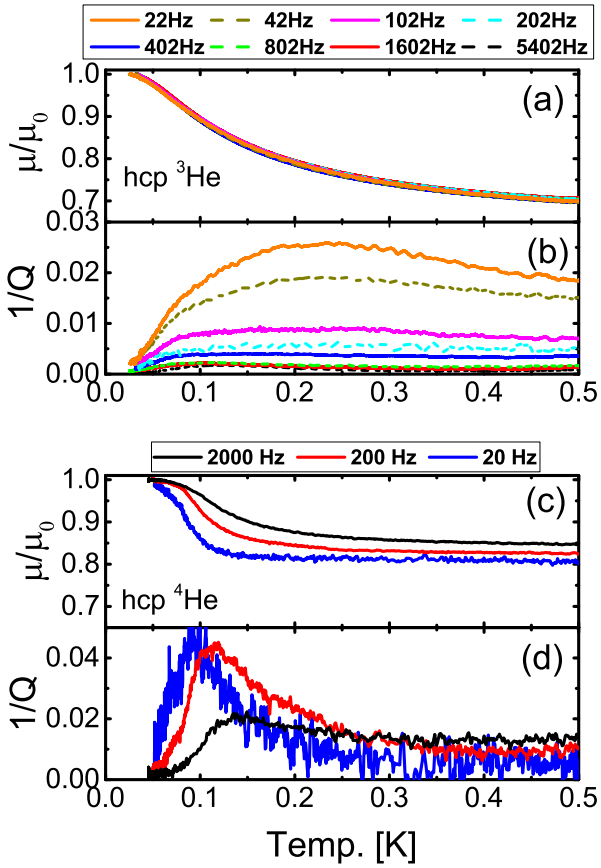


FIG. 32 Frequency dependence of the normalized shear modulus $\mu/\mu_0$ and dissipation $1/Q$ in helium polycrystals. Upper panels (a) and (b): hcp $^3$He at 11.9 MPa. The magnitude of the dissipation in hcp $^3$He decreases monotonically as the frequency increases from 22 Hz (upper orange curve) to 5402 Hz (lowest dashed black curve). Lower panels (c) and (d): hcp $^4$He at 3.8 MPa. The shear modulus crossover and the corresponding dissipation peak in hcp $^4$He shifts to higher temperatures as the frequency increases from 20 to 2000 Hz. (Cheng and Beamish, 2017)

### C. Dislocations and giant plasticity in single crystals

The low frequency experiments described in the previous section involved polycrystalline samples grown using the blocked capillary technique. There was little control of sample quality and the measured shear moduli were averages over different crystallite orientations. Although dislocation behavior has been studied in ultrasonic and elastic experiments on single crystals grown at constant pressure, the crystal quality varied and their orientations were not known. Measurements on oriented single crystals can provide information on individual elastic constants. If the sample cell and refrigerator have windows for optical access, crystal orientations can be determined from the facets seen during growth, and there can be more control of crystal growth and quality, e.g. by melting and regrowing from small seed crystals. Rojas *et al.* (2010) used an acoustic resonance technique in such an cell to study the elastic behavior of oriented single crystals of hcp $^4$He. However, measurements were limited to the solid helium's acoustic resonance around 18 kHz, and depended in a complicated way on all the crystal's elastic constants.

To measure the shear modulus of $^4$He single crystals, Haziot *et al.* (2013c) used the transparent cell shown in Fig. 33. It was made from a copper plate with an approximately hexagonal hole in which the helium crystals were grown, closed by two sapphire windows. The cell was attached to a dilution refrigerator whose base temperature was 15 mK, even with the windows that provided the optical access for the external camera used to record crystals' growth shapes (Balibar *et al.*, 2005; Haziot *et al.*, 2013c; Sasaki and Balibar, 2008). The cell contained two parallel, transversely polarized PZT transducers, mounted with their piezoelectric shear axes vertical. Oriented single crystals of $^4$He were grown in a 0.7 mm wide vertical slit between the two transducers and their shear modulus was measured using the same technique as described in the previous section. The sensitivity and the stability of this setup allowed measurements to be made for strains $\epsilon$ in the range $10^{-10}$ to $10^{-6}$ and for stresses as small as $10^{-9}$ bar. The transducers were carefully calibrated to give an absolute measurement of the shear modulus in the crystallographic direction perpendicular to the transducer polarization. Using a lock-in

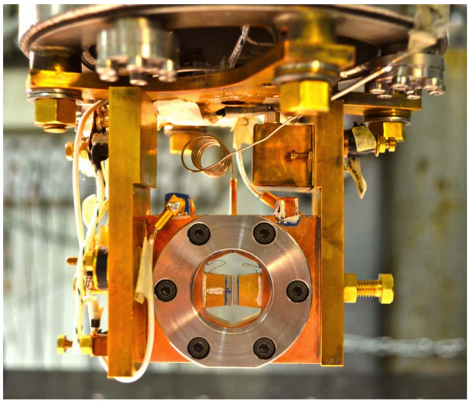

FIG. 33 The experimental cell used to measure mechanical properties of $^4$He crystals at ENS (Paris) (Balibar *et al.*, 2016). Single crystals were grown from the bottom up, inside the 0.7 mm slit between two vertical transducers in the center of the cell. Crystal orientations were obtained from photographs of facets when they began growing in the bottom part of the cell (see Fig. 35).

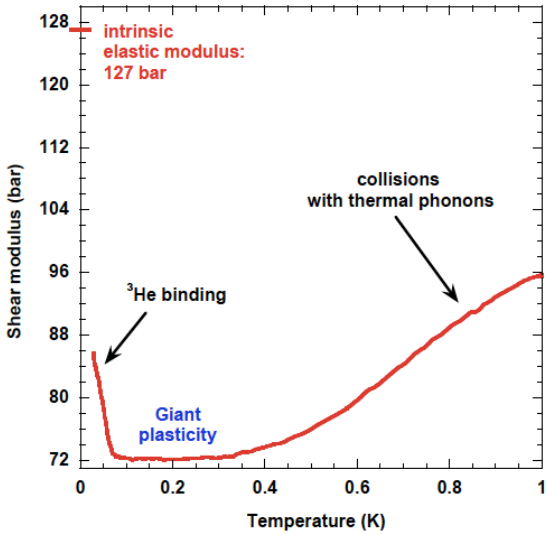


FIG. 34 In a temperature domain around 0.2 K, this isotopically pure crystal shows "giant plasticity": its shear modulus is highly reduced with respect to its intrinsic value (127 bar, indicated by the red bar on the vertical axis).

amplifier, both the amplitude of the shear modulus and the dissipation could be measured at frequencies between 1 Hz and 20 kHz.

### 1. Elastic constants and basal glide of dislocations

Figure 34 shows measurements by Haziot *et al.* (2013c) of the shear modulus for a crystal oriented with its sixfold symmetry axis (the "c" axis of the hcp structure) nearly vertical. This particular crystal was grown using isotopically purified $^4$He with a $^3$He concentration of 0.4 ppb. Around 0.2 K, dislocation motion reduced the elastic modulus by 43% from its intrinsic value of 127 bar (calculated from the ultrasonically measured high temperature elastic constants in Table I). The large shear modulus reductions like that seen around 0.2 K were referred to as "giant plasticity" but, despite their dislocation origin, they had most of the features of elasticity. The softening occurred at strains as small as $\epsilon \sim 2\times10^{-11}$ (corresponding to stress $\sigma \sim$ nbar) and the response was essentially linear and reversible. This indicates that the Peierls barrier for dislocation motion is extremely small, perhaps zero, for the dislocations responsible for shear softening in hcp $^4$He. The modulus increase below 0.1 K was due to $^3$He impurities binding to dislocations and limiting their motion. Above 0.3 K, dislocation motion was damped by collisions with thermal phonons. These processes introduce frequency dependence and dissipation into the crystal's mechanical response, behavior that is sometimes referred to as "anelasticity" (Nowick and Berry, 1972). The macroscopic irreversibility and hysteresis that are commonly associated with plasticity occur at much larger strains where new dislocations are created.

This behavior can be compared to that of classical crystals, where dislocations move only at high enough temperature and under sufficiently large stress. This is because dislocation lines can overcome the periodic lattice's Peierls barriers only by thermal activation of point defects (kinks or jogs) or at large stresses which reduce the barrier height. Dislocation motion in classical crystals induces only a small softening that is highly dependent on temperature and stress amplitude, in contrast to $^4$He where the softening is large and, in the absence of impurities, independent of temperature below 0.3 K.

Figure 35 shows the measured shear modulus for a number of crystals with different orientations. Crystal X15 was grown from the same isotopically purified $^4$He ($x_3$ =0.4 ppb) as the crystal in Fig. 34, but the others were grown from commercial $^4$He gas with a $^3$He concentration of 25 ppb. In the isotopically purified crystals, the remaining 0.4 ppb of $^3$He impurities was not sufficient to completely pin the dislocations, even at the lowest temperature of 15 mK. For the other crystals, there were enough $^3$He impurities to immobilize all the dislocations and recover the crystal's intrinsic elastic modulus below 60 mK. The intrinsic shear modulus depends strongly on the crystal orientation, since it is a function of all the elastic constants $C_{ij}$, but it could be calculated explicitly since the crystal's orientation with respect to the deformation direction was known from the growth facets shown at the right of Fig. 35. The colored ticks on the left vertical axis indicate these intrinsic values, which agree

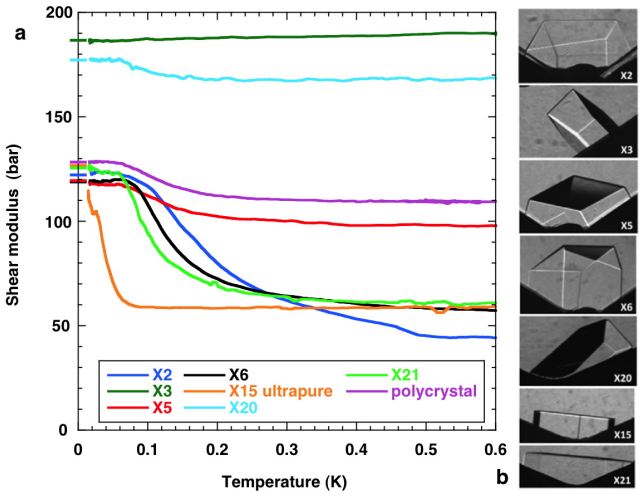


FIG. 35 Shear modulus for hcp $^4$He single crystals. The photographs on the right show the orientations (from top to bottom) of crystals X2, X3, X5, X6, X20, X15 and X21. The top green curve that shows no softening is for crystal X3. Data from crystal X20 lies directly below this (light blue line) and shows a small softening. The next curve below (purple line) is for a polycrystalline sample and shows similar softening to the polycrystal and to crystal X5 immediately below it (red line). Crystal X2 (dark blue line) has the largest high temperature softening. Two other crystals, X6 (black) and X21 (green) have intermediate, nearly identical softening. The final curve, for which softening occurs at much lower temperature, is for crystal X15, which was grown from $^4$He with a $^3$He concentration of $4\times10^{-10}$. The other crystals were all grown from natural $^4$He gas containing $2.5\times10^{-8}$ of $^3$He impurities. (Haziot *et al.*, 2013c)

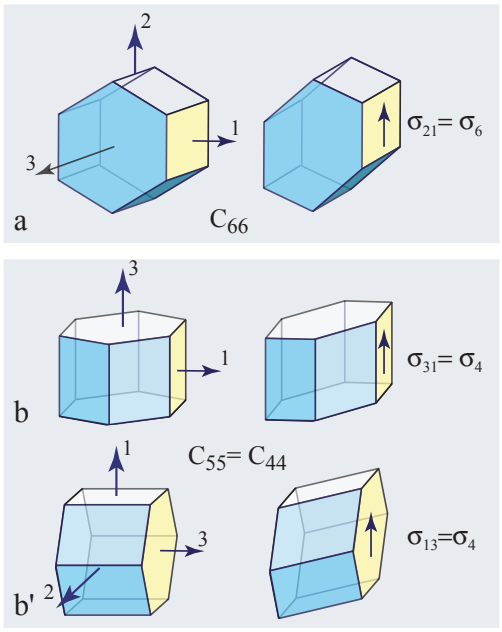


FIG. 36 Stresses and strains for shear deformations in hexagonal crystals. The case (a) in the top panel involves a deformation of the hexagons in the basal planes, with stress $\sigma$ given by the corresponding elastic constant $C_{66}$. The two cases (b) and (b′) in the lower panel occur when the hexagonal basal planes slide past each other, with stress given by the elastic constant $C_{44}$ (Balibar *et al.*, 2016).

with the low temperature values for the crystals grown from commercial $^4$He gas, confirming that 25 ppb of $^3$He is sufficient to completely pin the dislocations. Note that the crystal X3, whose $c$ axis was tilted by 45 degrees from the vertical, had the intrinsic shear modulus value with no measurable temperature dependence, and was used by Haziot *et al.* (2013c) to calibrate their transducers.

The elasticity tensor of hexagonal crystals like hcp $^4$He contains 5 independent elastic coefficients. Among these, the coefficient $C_{66}$ is associated with deformations of the hexagonal symmetry in these basal planes (shown in case (a) of Fig. 36), while the coefficient $C_{44}$ relates the shear stress and strain associated with basal planes gliding past each other (the deformations shown in cases (b) and (b′) of Fig. 36). For crystals like X3 that are oriented at 45 degrees, the measured shear modulus is essentially independent of both $C_{44}$ and $C_{66}$, so the temperature independent modulus shown in Fig. 35 suggests that one of these coefficients is responsible for the softening seen in other crystals. By analyzing the shear modulus changes for other crystal orientations, Haziot *et al.* (2013c) showed that it is $C_{44}$, not $C_{66}$, that changes. The data for all the single crystals was consistent with $C_{44}$ softening by approximately 60%, as shown in Fig. 37, and all other elastic constants remaining constant. This behavior was attributed to the fact that dislocations have preferential glide directions. A reduction in $C_{44}$ means that the dislocations responsible for the softening must glide either parallel to the basal planes, or along the prismatic planes parallel to the $c$ axis. In close-packed hexagonal materials, dislocations usually glide most easily in the basal plane (Hull and Bacon, 2011). Legrand (1984) explained that this is due to the splitting of edge dislocations into two partial dislocations because the stacking fault energy is very small for the close-packed basal planes. Such split dislocations are really "atomic ribbons" rather than 1D-lines, and glide easily parallel to the ribbon plane. This easy basal glide is observed in many hexagonal metals (e.g. Be, Mg, Co, Zn), although in some others (Zr, Ti) glide occurs along prismatic planes. Such conventional crystals do show behavior associated with dislocation glide at high temperatures, but dislocation effects are complicated by many other phenomena. The elastic changes due to dislocations are much clearer in $^4$He crystals. The softening can be very large - Souris *et al.* (2015) observed reductions in $C_{44}$ up to 90% in some cases.

Another unique feature of solid helium is the possi-

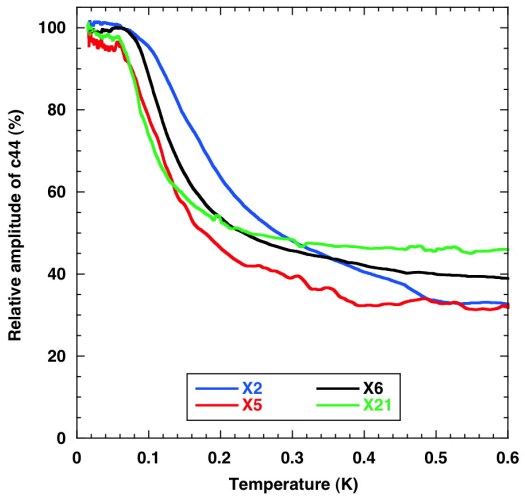


FIG. 37 Variation of $C_{44}$ for four of the single crystals whose shear modulus is shown in Fig. 35, calculated from the data using the known crystal orientations and assuming all other elastic constants remain constant.

bility of removing all impurities from $^4$He crystals. Even isotopic impurities ($^3$He) can be removed using a method reminiscent of the classical "zone melting" used to purify metals and semiconductors. It is based on the fact that impurities are usually more soluble in the liquid than in the solid, where the strain field around each impurity adds elastic energy. In the case of $^4$He, the difference in potential energy between the liquid and the solid has been calculated as -1.359 K per $^3$He atom (Edwards and Balibar, 1989; Pantalei *et al.*, 2010) so in equilibrium all the $^3$He impurities are trapped in the liquid phase if the temperature is low enough. During cooling, gently shaking the dislocations by applying an oscillating stress helps prevent $^3$He impurities from binding to dislocations so they are free to diffuse out of the solid. Figure 38 shows that when impurities were initially bound to dislocations at low temperature (crystals X2, X5 and X6), applying an oscillating strain larger than a few microbars detached the impurities, allowing dislocations to move and reducing the shear modulus. This stress threshold is larger when increasing the stress than when decreasing it, leading to hysteresis when the stress amplitude was cycled. For crystal X4 where the impurities were detached before cooling, the shear modulus was reduced by 80% from its intrinsic value and stayed at this low value when the applied stress was cycled. Figure 39 shows the linear stress vs. strain curve for this impurity free crystal, with a slope corresponding to the reduced shear modulus with high mobility dislocations. This contrasts with the non-linear plastic behavior of classical crystals, which retain their intrinsic defect-free elasticity at low stresses, and have a reduced modulus when the stress exceeds the Peierls stress for dislocation motion.

The low temperature softening of crystal X4 in Figs. 38 and 39 shows that, in the absence of $^3$He imurity pinning, dislocations glide freely in the basal plane down to the lowest applied shear strains ($\sim 3\times10^{-11}$). This corresponds to an extraordinarily small Peierls stress (the minimum shear stress for dislocation glide at zero temperature) of less than $\sim$0.3 mPa. Small yield stresses are often observed in hcp and fcc metals, where they are due to dissociated dislocations gliding in close-packed directions (Suzuki *et al.*, 2013). However, only upper limits could be placed on the Peierls stresses in those materials since impurity pinning immobilized the dislocations at low temperatures. The smallest observed yield stress (in copper crystals) was 0.28 MPa, corresponding to $\sigma_P/\mu < 7\times10^{-6}$ (Kamimura *et al.*, 2013), although some dislocation motion, often referred to as "pre-yield microplasticity", was seen at slightly lower stresses (Suzuki *et al.*, 2013). For the high purity hcp $^4$He crystal X4, the measurements put an upper limit on the Peierls stress that is nine orders of magnitude smaller than the experimental limits for metals. Part of the difference is due to helium's smaller elastic constants, but even when the Peierls stress is scaled by the shear modulus, $\sigma_P/\mu$ is still less than $2\times10^{-11}$ for hcp $^4$He, more than 5 orders of magnitude smaller than the corresponding upper limit for metals.

PIMC simulations (Borda *et al.*, 2016) confirm that the dislocations that glide in the basal plane of hcp $^4$He split into partials with rather large core widths (about 4 lattice spacings for the edge dislocation partials). They found that both the edge and screw dislocations glide easily but the simulations involved much larger effective stresses than those shown in Figs. 38 and 39 so could not confirm the extraordinarily small Peierls stresses extracted from shear modulus experiments. The measured Peierls stress limit of 0.3 mPa corresponds to an energy barrier (Peierls energy per unit length) $E_P = \frac{b^2}{2\pi}\sigma_P \approx 5\times10^{-24}$ J/m (Hull and Bacon, 2011). This suggests that a 100 $\mu$m long dislocation segment would be thermally excited over the Peierls barrier even at $\mu$K temperatures. Of course, glide is expected to occur via motion of geometric or thermally excited kinks along the dislocation, not by moving an entire dislocation over the Peierls barrier. The observed mobility of dislocations at low stresses presumably corresponds to the much smaller Peierls barrier for kink motion. Since the experimental values of the Peierls stress in solid helium are only upper limits, it is possible that quantum effects completely delocalize kinks and dislocations, i.e. reduce the Peierls barrier to zero.

### 2. Phonon damping, dislocation lengths and impurity motion

In order to better understand the dislocation motion, Haziot *et al.* (2013b,c), Fefferman *et al.* (2014) and Souris *et al.* (2015) measured the dissipation $1/Q$ of hcp $^4$He

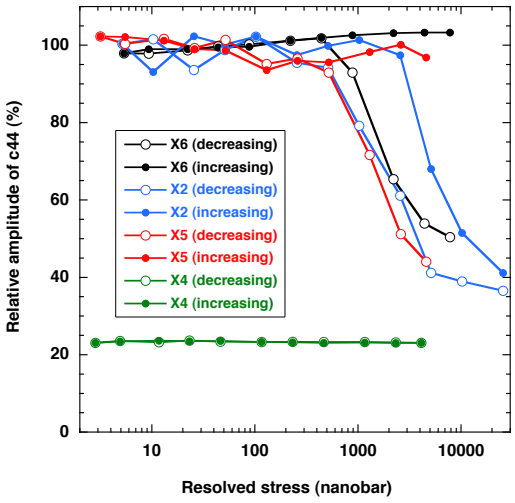


FIG. 38 Normalized shear elastic constant $C_{44}$ for four single crystals at 20 mK, as a function of the resolved stress projected on the basal plane. Above a threshold stress of a few $\mu$bar, dislocations break away from $^3$He impurities. Crystal X4 (the lowest green curves) was free of $^3$He impurities, since they were detached prior to cooling, and so remained soft over the entire range of stress, with no hysteresis (Haziot *et al.*, 2013c).

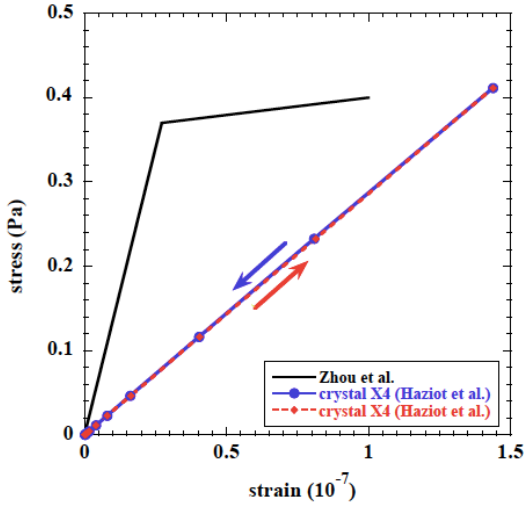


FIG. 39 Stress-strain diagram for crystal X4 (the same data as in Fig. 38), showing reversible linear behavior with a slope corresponding to a shear modulus reduced by 80%. Black line illustrates the non-linear elastic/plastic behavior expected for classical crystals (Haziot *et al.*, 2013d).

crystals as functions of temperature, frequency and strain amplitude. The shear modulus increase seen in Fig. 34 at temperatures above 0.3 K was attributed to damping of dislocations due to scattering of thermal phonons, which introduces a dislocation relaxation time $\tau = BL^2/\pi^2 C$ in the expressions for both the modulus and the dissipation, eqns. 15 and 16. The dominant fluttering mechanism for phonon scattering gives a damping force $B = gT^3$ so for the elastic constant $C_{44}$, the low frequency shear modulus expression of eqn. 13 is

$$\frac{\delta C_{44}}{C_{44}^0} = \frac{\alpha \Lambda L^2}{1 + \alpha \Lambda L^2} \tag{17}$$

and the corresponding dissipation of eqn. 14 becomes

$$\frac{1}{Q} = \frac{\alpha \Lambda L^2}{1 + \alpha \Lambda L^2} BL^2 \omega T^3 \tag{18}$$

As usual, $\Lambda$ is the density of dislocation lines per unit volume and $L$ is a typical length between nodes in the dislocation network, while $\alpha = 0.019$ and $B$= 905 s.m$^{-2}$K$^{-3}$ are the calculated values for hcp $^4$He at low densities (Souris *et al.*, 2014).

Figure 40 shows the measured dissipation in an hcp $^4$He crystal at temperatures above 0.3 K and frequencies of 1.5, 3 and 9 kHz (Haziot *et al.*, 2013a). The measurements were made at relatively large strains ($\epsilon$ =$10^{-7}$) to suppress the effects of $^3$He impurity pinning. The initial slopes agreed remarkably well with the predicted $\omega T^3$ behavior, clear confirmation of the phonon scattering mechanism for dislocation damping in helium. Deviations from linear behavior, like those above $\omega T^3 \gtrsim 10^4$ K$^4$ rad/s, just reflect the breakdown of the low frequency approximation $\omega\tau \ll 1$. Fefferman *et al.* (2014) were able to fit the entire dissipation and shear modulus curves by using the full expressions, eqns. 15 and 16, and integrating over a distribution of dislocation lengths $L$. However, even assuming a single dislocation length $L$, the initial linear region gave important information about the dislocation network. Because the modulus softening and the dissipation have different dependences on the dislocation length ($L^2$ and $L^4$, respectively) and the phonon damping is known, the dislocation network's density $\Lambda$ and length $L$ could be determined separately, something not possible from low frequency modulus measurements alone. Haziot *et al.* (2013a,b), Fefferman *et al.* (2014) and Souris *et al.* (2015) found dislocation densities $\Lambda$ between $10^4$ and $10^6$ per cm$^2$, rather small values that confirm the high quality of their single crystals. Their dislocation lengths $L$ were very large, between 63 and 230 $\mu$m. These values are nearly macroscopic and, most interestingly, are much larger than would be expected for a simple 3-dimensional network of dislocations. For example, if dislocations formed a regular cubic lattice, $\Lambda$ and $L$ would be related by the simple relation $\Lambda L^2 = 3$. For any three dimensional lattice of dislocations, the dislocation density $\Lambda$ should be of order $1/L^2$. The experiments of Haziot, Fefferman, Souris *et al.* found that this is not the case. In the 2013 experiment of Haziot *et al.* (2013b) the product $\Lambda L^2$ ranged from 17 to 57. When Souris

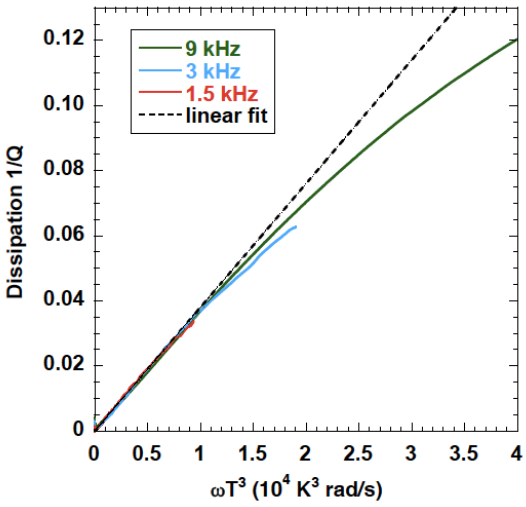


FIG. 40 Dissipation $1/Q$ in hcp $^4$He, at a strain $\epsilon = 10^{-7}$, plotted vs. $\omega T^3$. The frequency independent linear region for small $\omega T^3$ is the expected behavior for dislocation damping by scattering of thermal phonons via the fluttering mechanism; the dashed black line is a linear fit to the small $\omega T^3$ data. The 9 kHz data (green line) extends over the full range of the graph; the 3 kHz (blue line) and 1.5 kHz (red line) extend to about 2 and $0.9\times10^4$ K$^3$ rad/s, respectively.

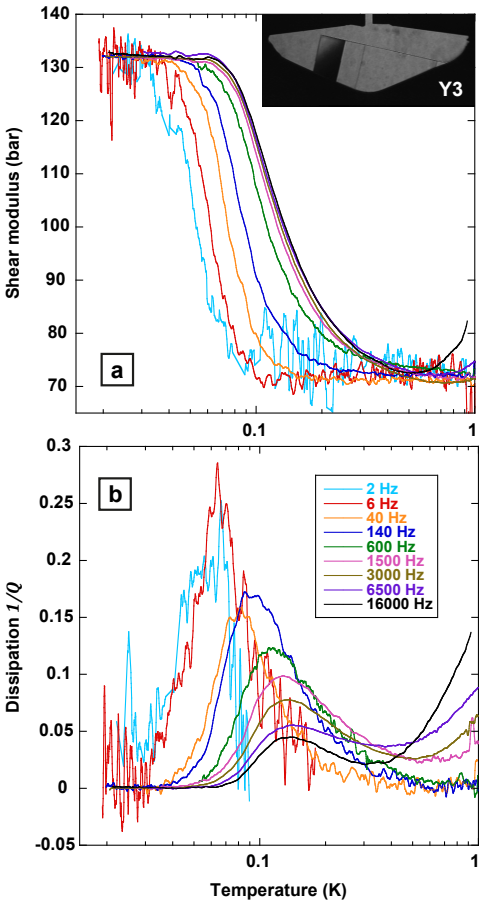


FIG. 41 Temperature variation of the low amplitude shear modulus (a) and dissipation (b) in hcp $^4$He, at the frequencies from 2 Hz to 16 kHz indicated in the legend (Haziot *et al.*, 2013b). The transition from stiff (at low T) to soft (at higher T) and the accompanying dissipation peaks are associated with binding of $^3$He impurities to dislocations. The shear softening and the associated dissipation peaks shift monotonically to higher temperatures as the frequency increases.

*et al.* (2015) tried to grow even better quality crystals, they found $\Lambda L^2$ values up to 471.

These very large values of $\Lambda L^2$ imply that the dislocations do not form a simple 3D-network. They must avoid intersections, e.g. by forming 2D arrays of parallel lines called "sub-boundaries". Friedel (1964) explained that the formation of such sub-boundaries can produce a very large softening since the aligned dislocations in sub-boundaries can glide in the basal planes in a cooperative way. For 3D dislocation networks, on the other hand, the maximum softening is about ∼10%, much smaller than the 90% changes seen by Souris *et al.* (2015).

The shear softening in the direction parallel to the hcp basal planes is analogous to that of a stack of sheets of paper, which is easy to deform in directions where the sheets slide past each other, but stiff in other directions in which the individual sheets would have to deform. Of course, in hcp crystals the whole atomic planes do not slide, but rather the movement occurs near dislocations. Furthermore, between paper sheets or in classical crystals, there is friction so that the deformation in response to stress is non-linear but, as shown in Fig. 40, in the absence of impurities the dissipation associated with the shear deformation in $^4$He approaches zero at low temperature. One possible explanation of this non-classical behavior is that quantum fluctuations make the kink energy vanish so that dislocation lines can move freely despite the periodic lattice potential. Another possibility is that kinks have a non-zero energy but the grown-in "geometric kinks" move along dislocations by quantum tunneling through a very small Peierls barriers. It would be hard to distinguish experimentally between the two possibilities.

The above paragraphs discussed the dissipation above 0.3 K, where it is a consequence of dislocations' interactions with thermal phonons. Below 0.2 K, a different dissipation mechanism becomes important when $^3$He impurities are present. These progressively bind to dislocations as the temperature decreases. In single crystals, there is a clear dissipation associated with $^3$He, as shown in Fig. 41 (Haziot *et al.*, 2013b). When impurities started binding, the dislocation motion decreased, stiffening the crystal, and the dissipation increased. It reached a peak at a temperature $T_p$ near the midpoint of the modulus

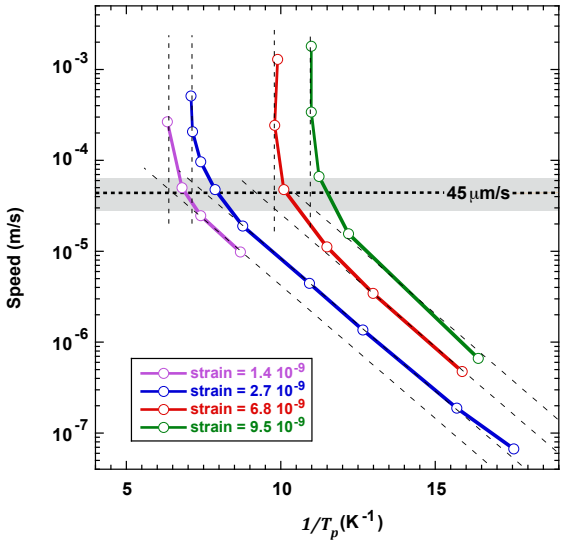


FIG. 42 Maximum dislocation speeds for dislocations, calculated from the length between nodes of their network and the strain amplitude and frequency (Haziot *et al.*, 2013b). From left to right, the curves correspond to strains of $1.4\times10^{-9}$ (purple), $2.7\times10^{-9}$ (blue), $6.8\times10^{-9}$ (red), and $9.5\times10^{-9}$ (green). Two regimes appear: below 45 $\mu$m/s, the bound $^3$He impurities move with the dislocations; above this critical speed, $^3$He impurities cannot follow the dislocations and act as static pinning sites (see text).

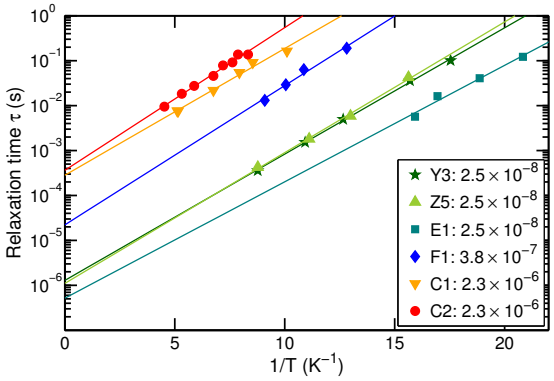


FIG. 43 Arrhenius semilog plot of the relaxation time $\tau$ of dislocations vs. the inverse temperature $1/T$ for crystals with different orientations and with the impurity concentrations indicated in the legend. Slight variations in slope show that there is a narrow distribution in the binding energy $E_B$ of $^3$He impurities to dislocations (see text).

stiffening, and vanished at lower temperatures where the dislocations were fully immobilized.

Knowing the density and typical length of dislocations in their crystals, Haziot *et al.* (2013b) could determine the dislocations' displacements and maximum speeds at their midpoints, for a given strain amplitude and frequency. The semi-log plot of Fig. 42 shows the maximum speeds vs. the inverse of the dissipation peak temperatures $T_p$. There were two different regimes. At high speeds, the peak temperature was independent of speed, behavior that was also seen at high frequencies in the shear modulus data of Fig. 41. This is the expected behavior if impurities act as static pinning points: they cannot move fast enough to follow dislocations' motion so they anchor the dislocations, giving a frequency independent shear modulus softening and a reduced dissipation peak. However, at low speeds, below 45 $\mu$m/s, the constant slope on this Arrhenius plot reflected a thermally activated regime in which the dislocation motion decreased exponentially as impurities bind at low temperatures. This means that $^3$He atoms are dragged along with dislocations but the motion of the dislocations dressed with impurities is damped. Assuming that this damping force is proportional to the density of bound $^3$He, the slopes of the semi-log plots of Fig. 42 give the binding energy $E_B$ of $^3$He impurities to the dislocation lines, $E_B = 0.67$ K for this particular crystal. The same binding energy was found in subsequent measurements by Fefferman *et al.* (2014). In a more detailed study, Souris *et al.* (2014) confirmed that the dissipation was proportional to the $^3$He concentration by comparing the behavior of crystals grown from $^4$He gas with three different impurity concentrations, $x_3$ respectively equal to $2.5\times10^{-8}$, $3.8\times10^{-7}$ and $2.32\times10^{-6}$. Figure 43 shows the relaxation times determined at the dissipation peak temperatures, where $\omega\tau = \sqrt{1+\alpha\Lambda L^2}$ (Fefferman *et al.*, 2014). The $^3$He binding energies from the slopes for different crystals varied from 0.6 to 0.71 K, consistent with previous values. The $\sim$0.1 K scatter in the slopes that can be seen in Fig. 43 is within the width of the binding energy distribution found in experiments on polycrystalline $^4$He (Mukharsky and Penzev, 2012; Syshchenko *et al.*, 2010).

Fefferman *et al.* (2014) determined the distribution of network lengths in a single crystal by measuring the strain dependence of the shear modulus at low temperature. By applying a large oscillating strain ($\epsilon = 10^{-6}$) while cooling from 0.5 K, the $^3$He impurities were prevented from binding to dislocations. When the strain amplitude was then reduced at 25 mK, $^3$He impurities began to bind, increasing the shear modulus as shown in Fig. 44. If there were a single network pinning length, there would be a precise value of the applied strain at which all dislocations would get pinned and the shear modulus would suddenly increase to the intrinsic value. However, short dislocations move less than long ones and their breakaway stress is larger, so $^3$He impurities progressively bind to and pin dislocations as the driving strain is reduced, beginning with the shortest ones. The smooth transition from soft to stiff that one sees in Fig. 44 is evidence that there is a distribution of lengths. From the shape of the transition Fefferman *et al.* (2014) found a broad distribu-

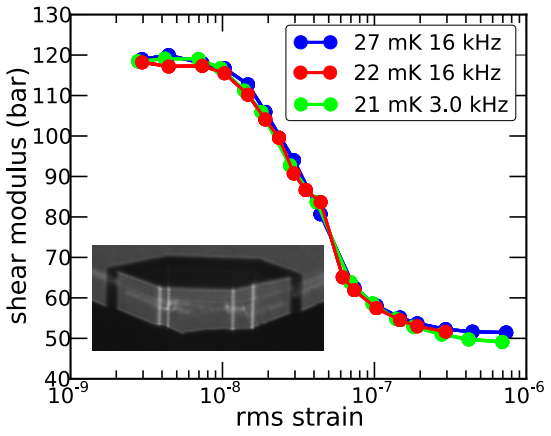


FIG. 44 Shear modulus of an hcp $^4$He single crystal near 25 mK, measured while decreasing the driving strain. The distribution of dislocation lengths between nodes of the network was determined by analysis of the transition between the unpinned soft state at large strain and the stiff intrinsic state at low strain (Fefferman *et al.*, 2014).

tion of network lengths, extending at least from 20 to 300 $\mu$m in this particular crystal. However, since a dislocation's contribution to the shear modulus is proportional to $L^2$, elastic measurements are not sensitive to shorter dislocations and there may be significant numbers of dislocations shorter than 20 $\mu$m.

When Fefferman *et al.* (2014) tried to fit low amplitude modulus and dissipation data sets like those shown in Fig. 41, using their measured distribution of network lengths, they found that they also had to include a distribution of $^3$He binding energies. To achieve good fits, they needed a width of order 0.1 K around the average value (about 0.7 K), consistent with the distribution of binding energies from Fig. 43 (Souris *et al.*, 2014). A distribution of binding energies is expected because dislocations rarely have purely edge or purely screw character. Depending on their orientation in the lattice, they can have a mixed character and the binding energy can vary between the value for an edge dislocation and that for a screw dislocation, which is expected to be smaller.

## VI. PLASTIC DEFORMATION AND FLOW

The shear modulus behavior described above occurred at very small stresses and strains, where conventional solids normally deform elastically, but it involved the motion of dislocations, which are normally associated with plastic deformation. Although the large modulus changes were described as "giant plasticity", the dislocation strain was proportional to the applied stress and returned to zero when the stress was removed. Such linear reversible behavior is more typical of elastic deformations. However, dislocation damping and pinning affected the dislocations' mobility and introduced dissipation and frequency dependence in the response. Such behavior is sometimes referred to as "anelastic", reserving the term "plastic deformation" for much larger deformations above the solid's yield point, where the crystal does not return to its original configuration when the stress is removed. This irreversible behavior involves the creation, multiplication and interaction of dislocations, not just the dislocation glide used to describe the shear modulus softening (giant plasticity) in solid helium. Zhou *et al.* (2013) have recently included these features in a model for solid helium to describe its plastic deformation in this regime. There can also be an intermediate region below the macroscopic yield point, often referred to as "microplasticity" (Maass and Derlet, 2018) in which the existing dislocations move but not reversibly, for example because they intersect with nearby dislocations and create jogs or other pinning points, without creation of significant numbers of new dislocations. In this section, we describe experiments on plastic deformation and flow of solid helium at large strains.

Dislocation glide and plastic deformation are responses to shear stresses. Purely hydrostatic pressure changes do not produce shear strains and therefore do not result in plastic deformation. The measurements on single crystals described in the previous section involved uniform simple shear but shear deformations are also generated by pressure gradients, by tensile strains in Young's modulus measurements, or by uniaxial compression in longitudinal sound waves. For solid helium confined at constant density in a rigid cell, thermal expansion increases the pressure when a sample is heated but if the thermal expansion is isotropic, as in cubic crystals, the pressure change is hydrostatic and no plastic deformation is expected. In hexagonal crystals, the thermal expansion coefficients parallel and perpendicular to the c-axis are different, so warming or cooling a confined hcp helium crystal will produce shear stresses which can plastically deform it. These stresses will be small in hcp $^4$He since its $c/a$ ratio is nearly independent of pressure, i.e. its thermal expansion is nearly isotropic (Franck and Wanner, 1970). However, in imperfect crystals there are microscopic regions of shear stress around defects and, even in cubic crystals, temperature changes can create prismatic dislocation loops if thermal vacancies precipitate into platelets (Hull and Bacon, 2011).

The first attempt to observe macroscopic plastic flow in solid helium involved growing an hcp $^4$He crystal around a magnetically levitated metal sphere (Andreev *et al.*, 1969), which was then subjected to a magnetic force of up to 250 times its weight. The ball's position was measured using an optical technique with a resolution of 20 $\mu$m. At 0.5 K no displacement was seen, putting an upper limit of 2 nm/s on the ball's velocity. Subsequent measurements using larger forces and more sensitive dis-

placement measurements succeeded in detecting the plastic deformation of solid helium. Beginning in the 1970s, several groups applied metallurgists' standard techniques (stress-strain curves, hysteresis loops, yield stresses and rate-dependent creep) to study the plastic deformation and flow of solid helium at higher temperatures.

### A. High temperature plastic flow and creep

Suzuki (1973, 1977) made the first systematic measurements of plastic deformation of solid helium. A ball or cylinder was embedded in the helium and an attached wire was used to pull it through the helium while measuring the displacement and applied force. Figure 45 shows typical force-displacement curves for hcp $^4$He. The corresponding shear stresses and strains can be roughly estimated from the geometry of the cell. The force (stress) initially increased, with a slope corresponding to elastic deformation of the helium, then dropped by as much as 40% above the helium's yield point. The solid then continued to deform at lower stress. The yield stress and the magnitude of the yield drop were smaller at higher temperatures and for smaller strain rates $\dot{\epsilon}$. At a shear strain rate $\dot{\epsilon} \sim 2{\times}10^{-3}$/s (corresponding to displacing the cylinder at 0.005 mm/s) and a temperature of 1.5 K, yield began at a shear stress (strain) $\sigma$ ∼13 kPa ($\epsilon \sim 0.04$). Above its yield point, the helium continued to deform, at roughly constant flow stress ($\sigma \sim 10$ kPa at $T$ =1.5 K for $\dot{\epsilon} \sim 2{\times}10^{-3}$/s), with no indication of work hardening even when the helium was deformed by 100%. This suggested that the steady flow involved dislocations being created, piling up at grain boundaries and walls and then being annihilated via climb. Suzuki found that the creep rate at small stresses was thermally activated, as expected since this process, known as Weertman creep, is controlled by the vacancy diffusion required for dislocation climb (Poirier, 1985; Weertman, 1955). For samples at 3.2 MPa (molar volume 20.5 cm$^3$), Suzuki found an activation energy of 19.5 K, consistent with activation energies for vacancy diffusion in hcp $^4$He measured with other techniques (Fraass *et al.*, 1989). The pronounced yield drops were attributed to high Peierls stresses for dislocations with Burgers vectors not lying in the hcp basal plane. Plastic deformation in complex geometries, or in polycrystalline samples, requires slip in multiple directions and is controlled by the slip system with the largest Peierls stress.

The same technique was used to study plastic deformation in bcc $^3$He (Sakai *et al.*, 1979). Flow stresses were smaller in low density crystals, e.g. $\sigma \sim 1$ kPa at $T = 0.6$ K for $\dot{\epsilon} \sim 2{\times}10^{-3}$ in crystals at pressures around 3.5 MPa. This is consistent with the smaller vacancy activation energies in bcc $^3$He. Also, plastic flow around an embedded object should be easier for bcc crystals, since dislocations can move in multiple slip planes, in contrast to hcp crystals where slip is confined to the basal plane.

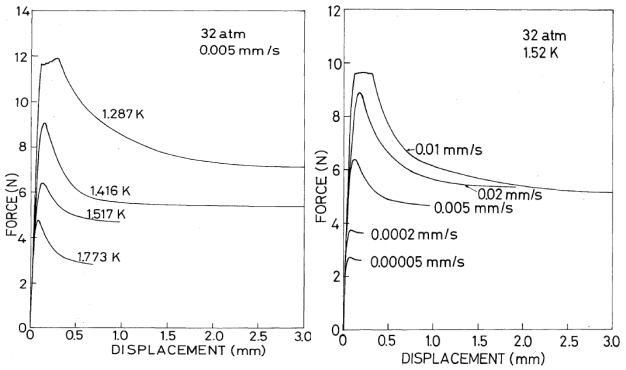


FIG. 45 Stress-strain (force-displacement) curves for hcp $^4$He at a pressure of 3.2 MPa (Suzuki, 1977). Left panel shows the temperature dependence at a shear strain rate $\dot{\epsilon} \sim 2{\times}10^{-3}$/s. Right panel shows the strain rate dependence at a temperature of 1.52 K. ©(1977) The Physical Society of Japan.

Sanders *et al.* (1977) used a somewhat different technique in which a piston driven by a pressurized bellows was used to compress and deform single crystals of solid $^4$He. A thin surface layer could be melted, largely eliminating the need for multiple slip systems since such unconstrained crystals were free to shear at the cell walls. Figure 46 shows stress-strain curves for an hcp $^4$He crystal at a compressional strain rate $\dot{\epsilon}$ =$10^{-4}$/s. For the unconstrained crystal (solid circles), the flow stress was too small to measure, less than 5 kPa. For the constrained crystal (open circles), flow occurred at a uniaxial stress of about 60 kPa. In contrast to the measurements of Suzuki (1973, 1977), these experiments showed no evidence of a yield drop. After the deformation ended, the stress relaxed (open triangles) but a residual stress of about 20 kPa remained for at least 20 minutes. Given the complicated deformation geometry, which involved compression of the solid as well as complex flow around the piston, it is difficult to convert these uniaxial stresses to the corresponding shear stresses relevant for plastic deformation. The experimental cell included ultrasonic transducers, which allowed Sanders *et al.* (1977) to monitor the density of dislocations via their contribution to the sound attenuation. In both the constrained and unconstrained crystals, the attenuation increased rapidly when deformation began, indicating that plastic deformation was accompanied by the expected dislocation multiplication.

Experiments on bcc $^4$He crystals (Sanders *et al.*, 1978) showed somewhat different behavior. The deformation of constrained samples was similar to that for hcp $^4$He,

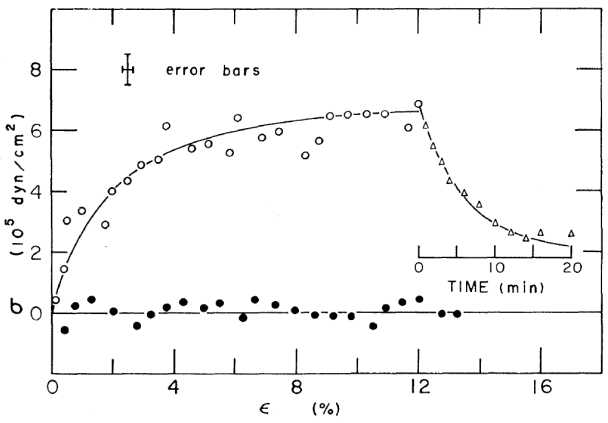


FIG. 46 Stress-strain curves for constrained (open circles) and unconstrained (solid circles) crystals of hcp $^4$He at a pressure of 3.2 MPa and temperature of 1.8 K. Open triangles show the stress relaxation when the strain is held constant (Sanders *et al.*, 1977).

although the flow stresses were several times smaller. For unconstrained samples the flow stress was again too small to measure. However, there was essentially no increase in ultrasonic attenuation associated with deformation of bcc crystals. This suggested either that bcc crystals deform via mechanisms that do not involve dislocation multiplication, or that any dislocations created do not contribute to ultrasonic attenuation. The difference between hcp and bcc crystals was confirmed in measurements on bcc $^3$He (Manning *et al.*, 1986), which also deformed easily, without significant sound attenuation changes in most of the crystal.

Plastic deformation has also been studied by electromagnetically pulling a 80 $\mu$m diameter superconducting wire through bcc $^4$He (Berent and Polturak, 1998). For stresses below about 0.6 kPa, the wire's velocity was linear in applied stress and its temperature dependence was consistent with the activation energy of thermal vacancies. This suggests that the flow was due to vacancy diffusion (Nabarro-Herring creep). For larger forces, the velocity depended non-linearly on stress and appeared to involve dislocation motion controlled by thermally activated climb. This technique has recently been extended to temperatures as low as 10 mK, but the stresses were not large enough to generate motion below 1 K (Ahlstrom *et al.*, 2014). In hcp $^4$He above 1 K, the 55 $\mu$m diameter wire moved in a series of apparently random jumps. These involved large displacements ($\sim$0.1 mm) at speeds up to $\sim$1 mm/s. In the bcc phase at high temperature, the wire moved much more slowly ($\sim$nm/s), but smoothly, as in the earlier experiments of Sanders *et al.* (1978).

The plastic deformation measurements described above were made near samples' melting points, where thermal processes control plastic deformation. Recent experiments (Cheng and Beamish, 2018b) have extended the piezoelectric techniques developed for low frequency shear modulus measurements to much larger strains. The large strains required for plastic deformation were achieved by using a stack of 18 transducers and increasing the drive voltage from millivolts to hundreds of volts. Uniform shear strains up to 0.4% could be produced, at constant strain rates generated by applying a linear voltage ramp to the transducer stack. The shear stress in the helium was measured *in situ* with a piezoelectric transducer, giving a sensitivity orders of magnitude higher than was possible with the mechanical systems used in earlier plastic deformation experiments. The uniform shear strains in this simple geometry allowed stress-strain curves to be quantitatively interpreted and the method could be used at much lower temperatures, so plastic deformation of solid helium could be studied in the non-thermal regime.

Figure 47 shows measured stress-strain loops for polycrystalline hcp $^4$He at 3.4 MPa, at temperatures of 25 mK (solid lines) and 900 mK (dashed lines). Starting at zero deformation, the strain was ramped at a constant rate $\dot{\epsilon} = 8{\times}10^{-6}$ s$^{-1}$ to a maximum value $\epsilon = 0.065\%$. It was then ramped in the opposite direction at the same rate, to $\epsilon =$ -0.065%, and finally back to zero. At 25 mK (solid lines), the stress-strain response was essentially linear and reversible, and the stress returned to zero, the behavior of an elastic solid. At 900 mK (dashed lines), the stress deviated from the elastic value for strains larger than 0.01% and followed a different path when the strain was ramped down. The resulting stress-strain loop did not close at its starting point, the irreversible and hysteretic behavior that characterizes plastic flow.

Figure 48 gives an overview of high temperature plastic flow (creep) in a polycrystalline hcp $^4$He sample. Panel (a) shows the helium's differential shear modulus $\mu_{diff} = \frac{d\sigma}{d\epsilon}$ at temperatures of 0.5 K and 0.9 K. Integrating $\mu_{diff}$ gives the corresponding stress $\sigma$ shown in the panel (b). Panels (c) and (d) show the corresponding behavior at 1.2 K. For small strains, the stress is proportional to the strain so $\mu_{diff}$ is constant. At 0.5 K, the elastic regime extends to $\epsilon \approx 0.08\%$, where the helium begins to deform plastically. At 0.9 K, plastic flow begins at smaller strains, around 0.02%, and the flow stresses are much smaller. The flow stresses increase with strain $\epsilon$, and with strain rate $\dot{\epsilon}$. At 1.2 K, the flow stresses are essentially constant and are much smaller, less than 0.4 kPa at the lowest strain rate $\dot{\epsilon} = 8{\times}10^{-6}$ s$^{-1}$. Extrapolating to the sample's melting point, 1.55 K, gives flow stresses of less than 100 Pa. This is about four orders of magnitude smaller than the yield stress of a very ductile metal like indium near its melting point. It is also much smaller than the flow stresses in earlier measurements on

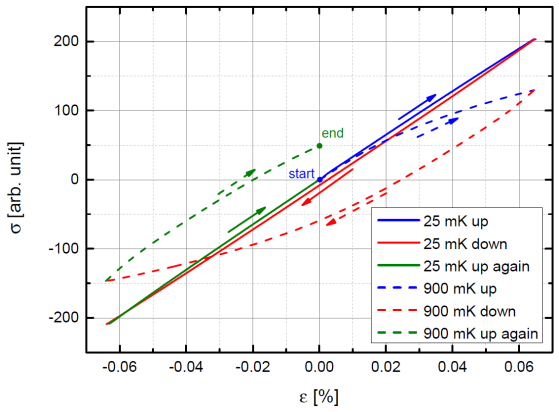


FIG. 47 Stress-strain loops for polycrystalline hcp $^4$He at 3.4 MPa and temperatures of 25 mK (solid lines) and 900 mK (dashed lines). The corresponding solid and dashed arrows show the directions of increasing or decreasing strain, starting and ending at zero strain (Cheng and Beamish, 2018b).

hcp $^4$He at similar temperatures, e.g. those shown in Figs. 45 and 46 (Sanders *et al.*, 1977; Suzuki, 1977). The differences may be due to the larger strain rates used in those experiments, their crystals' higher pressures (3.2 MPa vs. 2.64 MPa), and their complex flow geometries requiring multiple slip systems.

The variation of flow stress with strain rate depends on the creep mechanism, but is often described by a power law $\dot{\epsilon} \propto \sigma^n$. Vacancy diffusion gives a creep rate proportional to the pressure gradient and resulting stress, $\dot{\epsilon} \propto \sigma$, i.e. $n$= 1, but the creep rates in Fig. 48 (d) depend much more strongly on stress, with $n \approx 3.4$, as shown in the inset. Previous measurements gave similar exponents, with $n$ ranging from 3 to 5 in hcp $^4$He (Suzuki, 1977; Tsymbalenko, 1976), ∼3.5 in bcc $^4$He (Berent and Polturak, 1998) and ∼4 in bcc $^3$He (Manning *et al.*, 1986; Sakai *et al.*, 1979)). Exponents between 3 and 4 are characteristic of dislocation mechanisms like Weertman creep (Poirier, 1985; Weertman, 1955) where creep rates are controlled by depinning of dislocations via vacancy diffusion and climb.

### B. Low temperature slip and dislocation avalanches

The plasticity described above involved measurements above about half the samples' melting temperatures. Plastic deformation is quite different at low temperatures where thermally activated processes freeze out. This regime is particularly interesting in a quantum solid like helium where zero point motion dominates, tunneling allows defects like vacancies and impurities to propagate ballistically, and dislocations can move freely. To study non-thermally activated deformation mechanisms, much lower temperatures were required. Although there

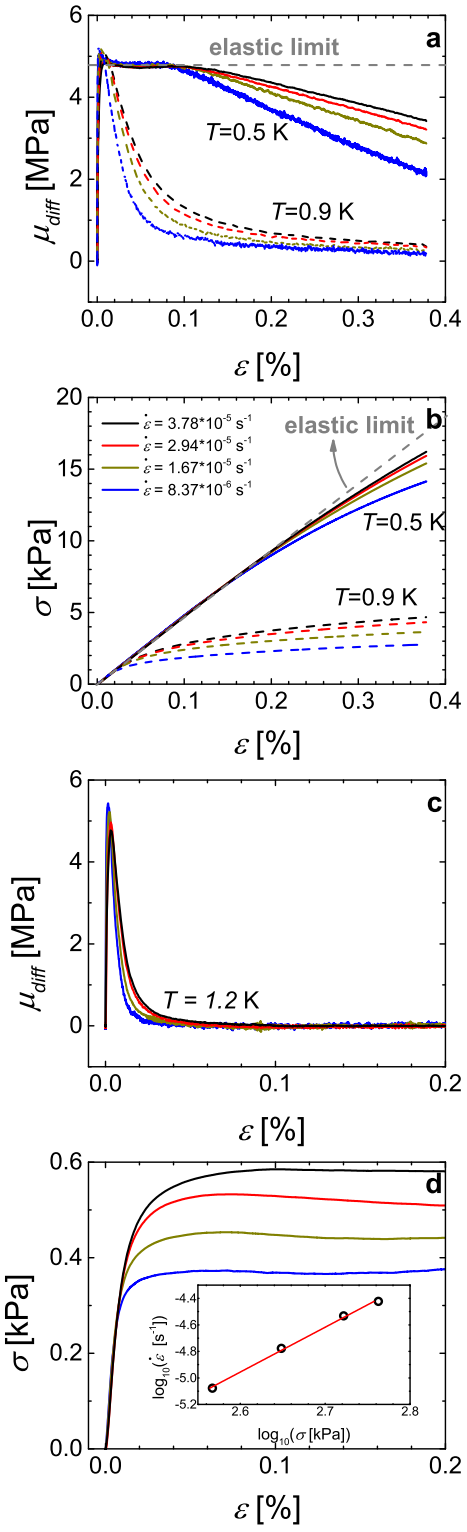


FIG. 48 Plastic creep in a 2.64 MPa hcp $^4$He sample (Cheng and Beamish, 2018b). Differential shear modulus (panel (a)) and corresponding stress (panel (b)) measured for different strain rates, at temperatures of 0.5 and 0.9 K. Panels (c) and (d) show the corresponing data at 1.2 K. The strain rates are given in the legend of panel (b). In each panel, the lowest (blue) curve corresponds to the lowest strain rate, 8.37 $\times 10^{-6}$ s$^{-1}$, and the higher curves to successively larger strain rates. Inset in (d) shows the relationship between shear stress $\sigma$ and strain rate $\dot{\epsilon}$.

were a few early experiments below 0.5 K (Levchenko and Mezhov-Deglin, 1982, 1984), their plastic deformation measurements were indirect. Crystals of hcp $^4$He were grown in a 1 mm diameter capillary and deformed by bending the capillary, at temperatures as low as 0.45 K. This reduced the crystals' thermal conductivity, an effect that was attributed to scattering of thermal phonons from dislocations created during deformation.

The stress-strain measurements of Fig. 48 were extended to temperatures below 400 mK, where thermal creep is negligible. Figure 49 shows $\mu_{diff}$ (upper panel) and $\sigma$ (lower panel) for the same sample at 16 mK, for a strain rate $\dot{\epsilon} = 3.8\times10^{-5}$ s$^{-1}$. The linear elastic region extended to $\epsilon \approx 0.3\%$, much higher than the 0.08% strain at which plastic deformation began at 0.5 K. At higher strains, plastic deformation involved abrupt stress drops of as much as 5%.

The time over which the stress dropped appeared to be about 2.5 seconds, but this was essentially the response time of the current amplifier, so faster amplifiers and data acquistion were used to resolve slip events. A typical strain ramp is shown in Fig. 50 (a), with the corresponding stress current $i$ (proportional to $\mu_{diff}$) shown in panel (b). A typical slip event, which was much faster than the stress drops in Fig. 49, is shown on expanded time scales in Figs. 49 (c) and (d). The event consisted of a negative current pulse, followed by a 10 kHz oscillation which decayed over about 40 ms. The oscillation was an acoustic resonance (Day and Beamish, 2012) of the solid helium filling the cell, triggered by the sudden stress release in the helium. The actual slip corresponded to the initial negative current, with a duration of about 25 $\mu$s.

Similar behavior has been seen in metals, where the slip events were identified as dislocation avalanches, which begin when dislocations break away from pinning sites, then move and multiply. A dislocation's motion is driven by the force $b\sigma$ proportional to the shear stress, and is opposed by the damping force $B$ proportional to its speed. This limits the dislocation's speed to $v_f = b\sigma/B$. In metals, the damping is due to electrons and limits $v_f$ to ~10 m/s for MPa applied stresses (Gorman *et al.*, 1969; Schaarwachter and Ebener, 1990). Even at the extremely high strain rates in shock experiments, typical dislocation speeds are much less than the sound speed (Lebyodkin *et al.*, 2009; Richeton *et al.*, 2005; Shashkov *et al.*, 2012). In contrast, dislocations in helium move freely at low temperatures, since the only damping is due to thermal phonons, with $B \approx 1.5\times10^{-8}\ T^3$ Pa·s (Haziot *et al.*, 2013a). For a shear stress of 15 kPa, this would limit dislocation speeds in $^4$He to about 30 m/s near the melting temperature ($T_m = 1.55$ K). At 16 mK, however, the phonon damping force would be negligible, even for dislocations moving at the speed of sound ($v_t \approx 200$ m/s). Even though solid helium has sound speeds an order of magnitude slower than typical metals, its dislocations can move and avalanches can propagate much faster, at close to the speed of sound.

Dislocation avalanches are usually detected from the sound waves generated by the sudden slip. In the helium deformation experiments, this acoustic emission could be captured with a digital oscilloscope, even for events much faster than that shown in Fig. 50 (d). A typical example is shown in Fig. 51 (a). The entire event occurred in less than a microsecond and generated a sound pulse with the spectrum shown in Fig. 51 (b), centered around 20 MHz. Since elastic deformations (including dislocations) cannot move faster than the speed of sound, the acoustic emission frequencies provide an upper limit on the size of slip events. This is less than 5 $\mu$m for the event in Fig. 51, much smaller than the dimensions of the solid helium sample (which was grown in a 170 $\mu$m gap between the transducers). Dislocation avalanches can occur inside the helium, away from the walls. The event in Fig. 49 was much larger, involving at least 5% of the gap area, so must have had dimensions of several millimeters. The size of the slip regions in these low temperature deformation experiments spanned many orders of magnitude.

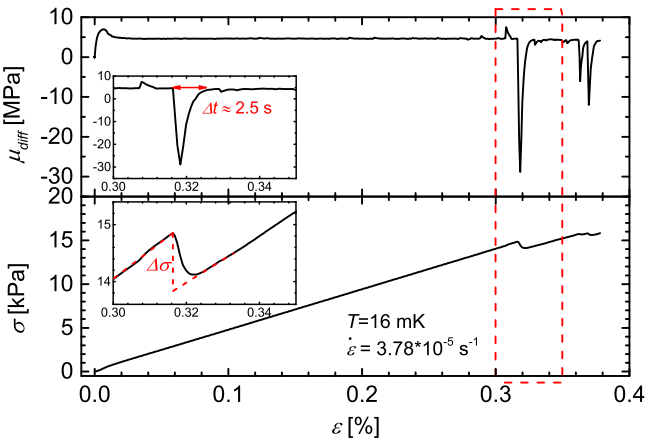


FIG. 49 Differential shear modulus and stress in hcp $^4$He at 16 mK. Insets show the large slip event at $\epsilon$= 0.32% on expanded scales.

### C. Pressure gradients, yield stress and annealing

In many applications the use of materials is determined by their yield stress $\sigma_c$, the threshold at which plastic deformation begins. In solid helium, the yield stress limits the pressure differences that can be maintained within solid helium, for example during freezing of helium using the blocked capillary method. Although helium's yield stress is small, in some geometries the pressure differences can be large. For example, a pressure difference $\Delta P$ between the ends of a cylindrical cell (of length $L$ and radius $R$) generates a net force $\pi R^2 \Delta P$ on the helium, which must be balanced by the force exerted by the

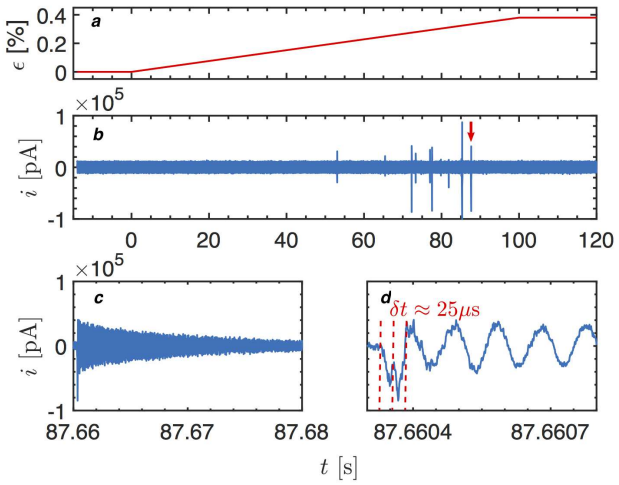


FIG. 50 Dislocation avalanches and acoustic ringing in hcp $^4$He at 16 mK: (a) strain (b) measured current (proportional to stress) (c) acoustic ringing over 20 ms following a typical slip event (d) first 3 ms of the slip event showing the initial negative stress change.

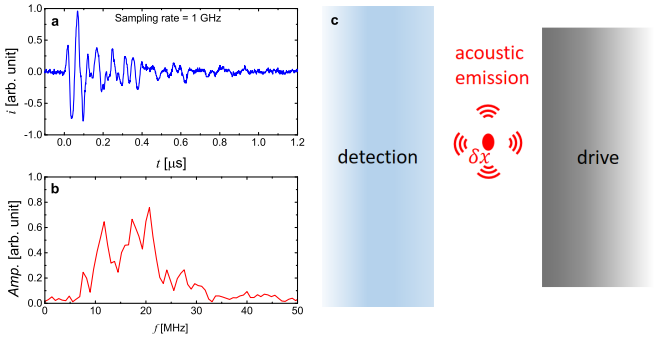


FIG. 51 Acoustic emission from a localized slip event in hcp $^4$He at 16 mK: (a) acoustic signal (b) frequency spectrum of acoustic signal and (c) schematic showing the localized event in the gap containing solid helium and the acoustic emission that is detected by the piezoelectric transducer.

side walls, $2\pi RL\sigma_w$. If the shear stress at the wall, $\sigma_w$, exceeds the yield stress, the helium will deform plastically and flow, as in the extrusion process used to make wires. The pressure at which this begins, $\Delta P_{max} = 2\sigma_c L/R$, depends on the aspect ratio $L/R$ of the cylinder. For solid helium with a low temperature yield strength $\sigma_c \approx$ 15 kPa, a cylinder with an $L/R$ ratio of 250 (e.g. a 3 mm long channel with a diameter of 25 $\mu$m, or a 5 cm long capillary with inner diameter 0.4 mm) could sustain pressure differences up to 7.5 MPa (75 bar) before slipping. This is the basis of the standard blocked capillary technique for freezing helium. Note that large pressure differences can occur not just in blocked capillaries, but in any cell with a large aspect ratio (Suhel and Beamish, 2011). Examples include long cylinders (Ray and Hallock, 2008), thin disks (Degtyarev *et al.*, 2010; Rittner and Reppy, 2009; Tsymbalenko, 1977), and narrow annular gaps (Rittner and Reppy, 2007).

At high temperatures, or in open cells with $L/R \sim 1$, pressure differences are much smaller but may still be significant. For example, Suhel and Beamish (2011) used rapid thermal quenching to generate pressure gradients in a cylindrical cell with length 30 mm and radius 15 mm ($L/R = 4$). A short current pulse was applied to a heater embedded near one end of a solid $^4$He sample at 50 mK, partially melting it. The helium refroze and cooled rapidly, reaching temperatures below 400 mK in as little as 20 seconds. This produced pressure differences as large as 35 kPa between *in situ* gauges at opposite ends of the cell. This corresponds to $\sigma_c \approx 4.4$ kPa, smaller than the 15 kPa yield stress from Fig. 49, which suggests that some of the initial pressure gradients relaxed at the higher temperatures during the initial thermal quench. Similar pressure differences have been observed in other helium experiments using cells with multiple pressure gauges (Birchenko *et al.*, 2018; Ray and Hallock, 2009).

Annealing at high temperatures can remove some defects and reduce internal stresses in crystals, as shown in the experiments by Suhel and Beamish (2011). For a 3.1 MPa polycrystalline hcp $^4$He sample (melting temperature of 1.79 K), the initial pressure difference between opposite ends of the cell ($\approx$ 26 kPa) was stable at temperatures below 400 mK. When the temperature was raised above 500 mK, the pressure difference decreased at a rate that increased with temperature. The data were consistent with a thermally activated annealing process with an activation energy of about 5 K. However, annealing above 500 mK did not completely eliminate pressure differences. When the temperature was held constant at 0.9 K, the pressure difference stabilized at 4.3 kPa after 9 hours. This corresponds to a static shear stress of $\sim$0.5 kPa, similar to the yield stress ($\sim$1 kPa) at which creep began at 0.9 K in Fig. 48. When the sample was warmed above 0.9 K, the pressure difference decreased further, to less than 1 kPa at 1.5 K. This is consistent with the decrease in yield stress at high temperatures (e.g. to $\sim$300 Pa at 1.2 K in Fig. 48).

It is clear that solid helium can support significant pressure differences, which can only be eliminated by warming the sample close to its melting temperature.

## D. Flow in solid helium

### 1. Vacancy diffusion flow

Vacancies enable dislocations to climb and so play an important role in plastic deformation by allowing dislocations to move around obstacles or to annihilate. At high temperatures, vacancies can also eliminate stresses via

Nabarro-Herring vacancy creep, which transports mass directly, as discussed in Section III A. In contrast to dislocations, which move in response to shear stresses, vacancies diffuse in pressure gradients but do not respond directly to shear deformations. The equilibrium vacancy concentration given by eqn. 2 is proportional to $e^{-(\frac{E_v+Pv_v}{k_BT})}$, so at temperatures high enough to create thermal vacancies, a gradient in the pressure $P$ creates a gradient in the vacancy concentration gradient $x_v$. Vacancies diffusing from low to high pressure regions produce a mass flow that reduces the pressure gradient.

However, the time scale for diffusive processes scales with the square of the sample dimension, so pressure relaxation via vacancy diffusion is very slow over large distances. For example, the blocked capillary technique relies on the flow of solid helium being negligible under the pressure gradients along the capillary. An early experiment searching for supersolidity in hcp $^4$He (Greywall, 1977b) detected no flow and established very low limits on pressure-induced flow at temperatures down to 30 mK. Diffusive vacancy flow is much more important in small samples and at high temperatures. For helium confined in the nanoscale pores of Vycor glass, ultrasonic measurements (Beamish *et al.*, 1991) showed that vacancy diffusion relaxed stresses within a pore on microsecond time scales at temperatures above 1 K. When external pressure was applied to a Vycor sample containing solid helium (Day *et al.*, 2005), mass flowed macroscopic distances into the pores at high temperatures, but no flow was seen below 500 mK. In a similar experiment in which a pressure difference of about 10 kPa was applied across solid $^4$He in 3 mm long, 25 $\mu$m diameter channels, mass flow through the channels equilibrated the pressures at temperatures near melting (Day and Beamish, 2007a). Below 1 K there was no evidence of flow (Day and Beamish, 2006), which is not surprising, given helium's yield stress and the channels' large aspect ratio ($L/R = 240$).

One experiment involving hcp $^4$He in a high aspect ratio cell (a disk-shaped chamber of thickness 0.1 mm, radius 8.6 mm) did detect a very slow pressure relaxation at temperatures as low as 19 mK (Rittner and Reppy, 2009). The relaxation rate was compatible with a thermal activation process but the activation energy, ∼28 mK, was very small and the flow mechanism was not clear.

The absence of non-activated flow at low temperatures is consistent with the consensus that there are no zero point vacancies in hcp $^4$He. However, thermal vacancies cannot simply vanish when a solid is cooled. To disappear, they must diffuse to a vacancy sink, i.e. to a crystal surface or to internal defects like dislocations and grain boundaries. Vacancies in helium might also phase separate into clusters (Boninsegni *et al.*, 2006a), in which case they would collapse to create prismatic dislocation loops (Hull and Bacon, 2011). If thermal quenching is fast enough, larger non-equilibrium vacancy concentrations might survive. Unusual features in experiments involving solid helium flow through a nozzle have been interpreted in terms of flow of vacancies at large non-equilibrium concentrations (Benedek *et al.*, 2016).

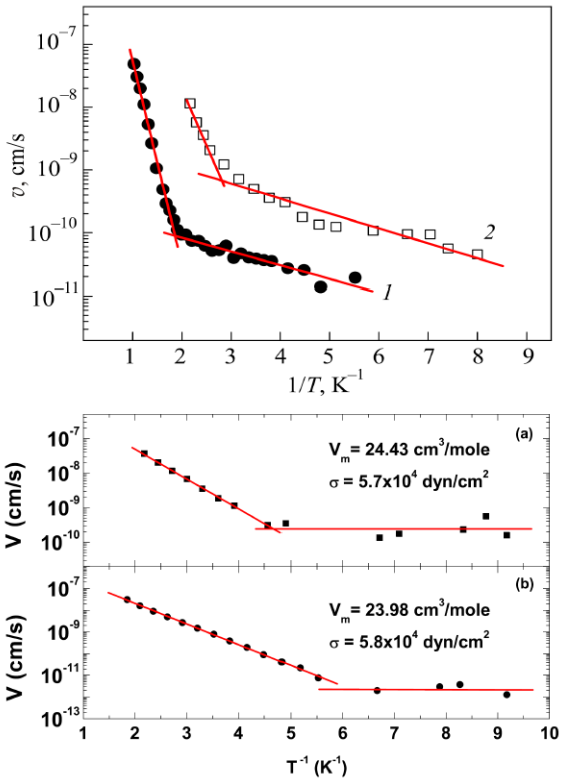


FIG. 52 Flow velocity for solid helium in 6 to 8 $\mu$m diameter channels through a membrane. Upper panel: data for two polycrystalline hcp $^4$He samples (labeled "1" and "2") with molar volume 21.05 cm$^3$/mol (Zhuchkov *et al.*, 2015). Lower panel: data for polycrystalline bcc $^3$He at samples with molar volumes (a) 24.43 and (b) 23.98 cm$^3$/mol (Lisunov *et al.*, 2015).

Since the vacancy flow rate is directly proportional to the pressure gradient, more sensitive measurements can be made by applying pressure differences across shorter channels. Zhuchkov *et al.* (2015) used a capacitative technique in which a pressure difference was generated across 6-8 $\mu$m diameter channels through a 10 $\mu$m thick polymer membrane ($L/R$ ∼3) embedded in solid $^4$He. Flow velocities through the channels, determined from the displacement of the membrane, are shown in the upper panel of Fig. 52. At high temperatures they observed thermally activated flow with activation energies between 6.5 and 13.9 K, consistent with vacancy activation energies in $^4$He. Below 500 mK the temperature dependence was much weaker, corresponding to activation energies ∼0.5 - 0.7 K. They attributed the high temperature flow to thermally activated vacancy diffusion, but the origin

of the very slow creep at low temperatures was unclear, although it might involve motion of dislocation kinks.

Lisunov *et al.* (2015, 2016) made similar measurements on bcc $^3$He, shown in the lower panels of Fig. 52. Above 200 mK they saw thermally activated flow, with activation energies between 2.3 and 3.1 K. These energies are smaller than for hcp $^4$He, but are similar to vacancy energies in bcc $^3$He (e.g. 4.25 K at 35 bar (Heald *et al.*, 1984)). However, the flow rate for $^3$He did not continue to drop below 200 mK, but instead approached a constant value at the lowest temperature (100 mK). The authors suggested that the high temperature flow involved motion of dislocations via thermally activated creation of kink pairs. The temperature-independent flow below 200 mK indicated a quantum mechanism of mass transport, but the mechanism was unclear.

A recent experiment on bcc $^3$He confined in a much larger channel (3 mm diameter, with $L/R \approx 6$) gave similar results, shown in Fig. 53 (Cheng and Beamish, 2018a). A pressure difference applied between the ends of the channel generated flow which was thermally activated above 100 mK, but approached a constant rate at the lowest temperature (30 mK). However, the activation energy was smaller (∼0.85 K) and the flow rates were much larger than in the experiments of Lisunov *et al.* (2015, 2016). This suggests that both the thermally activated and the temperature-independent flow shown in Fig. 53 involved dislocations, which would be more mobile in this bulk geometry than in the small channels of Lisunov et al., where they are expected to be pinned at the walls.

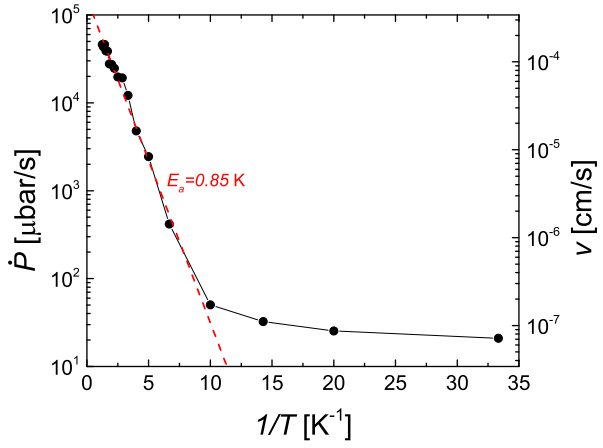


FIG. 53 Flow velocity (right axis) and rate of pressure change (left axis) for polycrystalline bcc $^3$He in a 3 mm diameter channel, at a pressure of 3.6 MPa (Cheng and Beamish, 2018a). Dashed line corresponds to a thermally activated process with activation energy 0.85 K

### 2. Low temperature superflow in solid $^4$He

In addition to the creep and plastic flow described above, recent experiments have shown intriguing low temperature mass flow through cells filled with hcp $^4$He (Hallock, 2015, 2019; Ray and Hallock, 2008). This flow appeared below 0.6 K, with flow rates that were nearly independent of the pressure difference across the solid, and increased at lower temperatures. These features are clearly not associated with thermally activated flows like those described above, but are typical of superfluids. The low temperature flow was very sensitive to $^3$He impurities, with concentrations $x_3$ as small as $10^{-6}$ blocking the flow below 100 mK (Cheng and Beamish, 2016; Vekhov *et al.*, 2014). This suggests that the flow occurs along low dimensional channels, for example superflow in a network of 1-dimensional dislocations (Shin *et al.*, 2017; Vekhov and Hallock, 2012), a possibility raised by PIMC simulations (Boninsegni *et al.*, 2007) that indicated that some types of dislocations in hcp $^4$He have superfluid cores. This topic has recently been reviewed by Hallock (2019).

## VII. OPEN QUESTIONS AND FUTURE DIRECTIONS

The work reviewed in this paper makes it clear that defects like vacancies, impurities and dislocations have dramatic but well-understood effects on the mechanical behavior of quantum solids like helium. However, it is important to note that essentially all the experiments upon which this understanding is based involve mobile dislocations, primarily those gliding in the basal plane of hcp $^4$He. There is no direct experimental evidence of the properties (or even the existence) of other types of dislocations in helium, despite their importance in plastic deformation and flow. This contrasts with the situation in metals and other conventional materials, where TEM and x-ray techniques have been used to directly confirm the properties of different types of dislocations, and to determine their densities and network structures.

Although the high pressures required to grow helium crystals rule out TEM imaging, it is possible that modern synchrotron x-ray sources and techniques could provide microscopic information about the structure of dislocations, stacking faults and grain boundaries. It might also be possible to take advantage of advances in "matrix isolation" spectroscopy of atoms embedded in solid helium to image or probe extended defects, in analogy to the impurity decoration techniques that have been used to image vortices in superfluid droplets (Gessner and Vilesov, 2019; Gomez *et al.*, 2014).

In the absence of direct imaging of dislocations, experiments can only determine average properties associated with networks having unknown distributions of orientations and loop lengths. The recent low frequency shear modulus measurements on optically oriented single crys-

tals have provided detailed and consistent information about dislocation networks in hcp $^4$He. However, there are significant discrepancies with, for example, the dislocation densities and lengths inferred less directly from high frequency ultrasonic measurements.

One possible approach to extract information about specific dislocations would be to probe mechanical properties on a microscopic scale. Given the low dislocation densities ($\Lambda \sim 10^4/\mathrm{cm}^2$) and the loop lengths ($L \sim 100\ \mu$m) inferred from shear modulus measurements in high quality $^4$He crystals, it seems likely that there are dislocation-free regions with dimensions of tens of micrometers. There have been a few experiments involving solid helium confined on this scale, including flow measurements across an 8 micron gap (Shin *et al.*, 2017) or along 25 micron cylindrical channels (Day and Beamish, 2006), and shear modulus measurements on helium in an 11 micron gap (Aoki *et al.*, 2016). The smallest avalanches detected in hcp $^4$He polycrystals (Cheng and Beamish, 2018b) at low temperatures were of comparable sizes and may have initiated at a single dislocation. Submicron cavities have been used to probe superfluid helium (Souris *et al.*, 2017) and it may be possible to apply micromechanical or optomechanical techniques to study solid helium on samples small enough be free of dislocations or other defects. Such measurements could, for example, test predictions (Borda *et al.*, 2014) of the ultimate shear strength of perfect helium crystals, or allow dislocations to be introduced into perfect crystals to test dislocation models of superflow.

Numerical simulations have provided a great deal of information about dislocations and their networks in conventional solids. In quantum solids, PIMC simulations have made remarkable advances, but they are still limited to relatively small numbers of atoms, so cannot provide the same level of detailed information about extended defects and dislocation networks in helium crystals.

Neither PIMC simulations nor experiments provide evidence for the existence of equilibrium zero point vacancies in solid helium, but they may exist in regions of large elastic strain (Pollet *et al.*, 2008). It is also possible that nonequilibrium vacancies could be introduced into solid helium by rapid deformation or flow (Benedek *et al.*, 2016). Rapid thermal quenching could also produce a finite concentration of vacancies at low temperatures, given the large equilibrium vacancy concentration ($\sim$0.3%) near melting. Since these vacancies can only disappear by migrating to a surface or a defect like an edge dislocation, or by phase separating, a finite concentration might survive rapid cooling to low temperatures, particularly in $^3$He where they are expected to be less mobile than in $^4$He.

One of the most intriguing phenomena in solid $^4$He is the low temperature flow that appears around 0.6 K in low pressure crystals (Hallock, 2019). The flow increases upon cooling, but is blocked around 100 mK by very small concentrations of $^3$He impurities. It has characteristics of superflow but the nature and the location of the flow channels are not yet certain (Cheng and Beamish, 2016). However, very recent experiments with partially blocked channels do not appear to be consistent with flow in 2D films (Rubanskyi and Hallock, 2019; Shin and Chan, 2019). One dimensional flow along superfluid dislocation cores, as predicted in PIMC simulations, is an exciting possibility but experiments have not yet provided a "smoking gun" to confirm this scenario. This is largely because there is no direct experimental evidence for the types of dislocations that are predicted to have superfluid cores (screw dislocations aligned along the hcp $c$-axis; edge dislocations lying in the basal plane and Burgers vectors along the hcp $c$-axis). The superfluidity predicted for these dislocations appears to be due to the fact that they do not disassociate into partials and so have large strains near their cores. This also results in large Peierls barriers, which immobilizes them. The mobile dislocations that can be detected in elastic measurements (edge or screw dislocations gliding in the basal plane) have essentially the opposite properties. They dissociate into widely separated partials with small strains and have no measurable Peierls barrier to their motion.

A number of experiments have recently been proposed to more clearly distinguish the flow or superclimb associated with superfluid dislocations from other possible deformation or flow mechanisms (Kuklov, 2019). However, clear confirmation of superfluid dislocations would require oriented single crystals which can be compressed or sheared in specific crystallographic directions. Although challenging, this could be done using the optical orientation and crystal growth techniques that were used so successfully in the low frequency shear modulus experiments to provide detailed information on the properties of mobile basal dislocations in $^4$He. Measurements with optically oriented single crystals would have similar advantages for many other measurements, including plastic deformation experiments.

The recent plastic deformation experiments by Cheng and Beamish (2018b) showed that, at temperatures below 0.4 K, large scale deformation in hcp $^4$He occurs via dislocation avalanches. The avalanches had a wide range of sizes and their accompanying acoustic emission provides opportunities to study the scaling laws that have been observed in conventional solids, but in non-thermal and quantum regimes. Similar experiments on bcc crystals, with their different dislocation structures, multiple slip systems and expected Peierls barriers, would be valuable. Although elastic measurements on bcc $^4$He and $^3$He have shown some signatures of mobile dislocations, there is presently much less information about their properties than in the hcp phases of helium.

Vacancies appear to play a more important role in the bcc phase of $^4$He, where plastic deformation occurs smoothly (Ahlstrom *et al.*, 2014) and does not seem to

involve the creation of dislocations (Sanders *et al.*, 1977). To better understand the role of vacancies and dislocations in deformation of bcc helium, measurements should be made over a wide range, extending to low temperatures where vacancies freeze out. This is not possible in $^4$He since the bcc phase does not exist below 1.5 K, but can be done in the bcc phase of $^3$He, which is even more quantum mechanical than the more thoroughly studied hcp $^4$He.

Solid $^3$He also provides a unique opportunity to study the effects of spin on dislocation motion. Low frequency shear modulus measurements on hcp $^3$He (Cheng and Beamish, 2017) were interpreted in terms of a new "spin friction" mechanism of dislocation damping, an addition to the known phonon and electron damping mechanisms in other materials. Measurements at lower temperatures, particularly in the spin-ordered magnetic phases below 1 mK, would confirm this and might provide insight into dislocation motion in conventional magnetic solids.

## ACKNOWLEDGMENTS

This work was supported by grants from the Natural Sciences and Engineering Council of Canada (NSERC), the University of Alberta, and ERC (AdG 247258-SUPERSOLID). The authors would like to express their appreciation to their students, post-doctoral fellows and collaborators on work described in this review, and to Pawel Pieranski for providing Fig. 36. They would also like to thank their colleagues in the field of helium solids, who have generously shared their expertise and ideas over many years.

## REFERENCES

Abel, WR, AC Anderson, and JC Wheatley (1961), "Propagation of sound in $^3$He," Physical Review Letters **7** (8), 299.

Adams, E Dwight (2004), "Solid helium-3," Journal of Low Temperature Physics **135** (5-6), 695–721.

Adams, ED, YH Tang, K Uhlig, and GE Haas (1987), "Thermodynamics of freezing and melting of $^4$He in Vycor," Journal of Low Temperature Physics **66** (1-2), 85–98.

Adams, MA, J Mayers, O Kirichek, and RBE Down (2007), "Measurement of the kinetic energy and lattice constant in hcp solid helium at temperatures 0.07–0.4 K," Physical Review Letters **98** (8), 085301.

Ahlstrom, SL, DI Bradley, M Človečko, SN Fisher, AM Guenault, Edward Ashley Guise, RP Haley, Mukesh Kumar, Peter VE McClintock, GR Pickett, *et al.* (2014), "Plastic properties of solid $^4$He probed by a moving wire: Viscoelastic and stochastic behavior under high stress," Journal of Low Temperature Physics **175** (1-2), 147–153.

Alers, GA, and JE Zimmerman (1965), "Dislocation mobility in fcc metals below 1 K," Physical Review **139** (2A), A414.

Allen, Alastair Robert, MG Richards, and J Schratter (1982), "Anomalous temperature dependence of d and $T_2$ for dilute solutions of $^3$He in solid $^4$He," Journal of Low Temperature Physics **47** (3-4), 289–320.

Alles, H, V. Tsepelin, A. Babkin, R. Jochemsen, A. Ya. Parshin, and I. Todoschenko (2001), "Observations on faceting of $^3$He crystals at T=0.55 mK," Journal of Low Temperature Physics **124**, 189–196.

Amidon, William H, and Kenneth A Farley (2010), "Mass spectrometric $^3$He measurement in $^4$He-rich phases: Techniques and limitations for cosmogenic $^3$He dating of zircon, apatite, and titanite," Geochemistry, Geophysics, Geosystems **11** (10).

Andreev, AF (1982), "Quantum crystals," Progress in Low Temperature Physics **8**, 67–131.

Andreev, AF, L Keshishev, L Mezhov-Deglin, and A Shal'nikov (1969), "Attempt at observing vacancions in $^4$He crystals," Zhur Eksper Teoret Fiziki Pis ma Redaktsiiu **9** (9), 507–510.

Andreev, AF, and IM Lifshits (1969), "Quantum theory of defects in crystals," Zhur Eksper Teoret Fiziki **56** (6), 2057–2068.

Andreev, Aleksandr F (1976), "Diffusion in quantum crystals," Soviet Physics Uspekhi **19** (2), 137.

Andreeva, OA, and KO Keshishev (1991), "Solid-superfluid $^4$He interface," Physica Scripta **1991** (T39), 352.

Andreeva, OA, KO Keshishev, and S Yu Osip'yan (1989), "Anisotropy of growth coefficient and surface hardness of the $^4$He crystals," Journal of Experimental and Theoretical Physics **49**, 759.

Andronikashivili, EL (1946), "A direct observation of two kinds of motion in helium II," Zhur Eksper Teoret Fiziki **16**, 780.

Aoki, Yuki, Izumi Iwasa, Takeru Miura, Akira Yamaguchi, and Yuichi Okuda (2016), "Shear modulus of solid helium-4 confined in a 10 $\mu$m gap," Physica B: Condensed Matter **482**, 19–23.

Arms, DA, RS Shah, and RO Simmons (2003), "X-ray Debye-Waller factor measurements of solid $^3$He and $^4$He," Physical Review B **67** (9), 094303.

Babkin, AV, H Alles, Pertti J Hakonen, A Ya Parshin, JP Ruutu, and JP Saramaki (1995), "Observation of a new surface state on $^4$He crystal interfaces," Physical Review Letters **75** (18), 3324.

Balibar, S, and B Castaing (1985), "Helium: Solid-liquid interfaces," Surface Science Reports **5** (3), 87–143.

Balibar, S, B. Castaing, and C. Laroche (1980), "Nucleation and orientation of $^4$He crystals," Journal de Physique Lettres **41** (12), 283–285.

Balibar, S, DO Edwards, and C Laroche (1979), "Surface tension of solid $^4$He," Physical Review Letters **42** (12), 782.

Balibar, S, T. Mizusaki, and Y. Sasaki (2000), "Comments on heterogeneous nucleation in helium," Journal of Low Temperature Physics **120**, 293–314.

Balibar, S, and P Nozières (1994), "Helium crystals as a probe in materials science," Solid State Communications **92** (1-2), 19–29.

Balibar, Sébastien, Harry Alles, and Alexander Ya. Parshin (2005), "The surface of helium crystals," Reviews of Modern Physics **77**, 317–370.

Balibar, Sébastien, John Beamish, Andrew Fefferman, Ariel Haziot, Xavier Rojas, and Fabien Souris (2016), "Dislocations in a quantum crystal: Solid helium: A model and an exception," Comptes Rendus Physique **17** (3-4), 264–275.

Bauer, Charles L, and Robert B Gordon (1962), "Mechanism for dislocation pinning in the alkali halides," Journal of

Applied Physics **33** (2), 672–682.
Beamish, JR (2001), "Elastic properties of solid inert gases," Handbook of Elastic Properties of Solids, Liquids, and Gases **2**, 77.
Beamish, JR (2019), "Plastic deformation and creep in solid helium," Journal of Low Temperature Physics **197**, 187–207.
Beamish, JR, AD Fefferman, A Haziot, X Rojas, and S Balibar (2012), "Elastic effects in torsional oscillators containing solid helium," Physical Review B **85** (18), 180501.
Beamish, JR, and JP Franck (1982), "Sound propagation at frequencies from 3 to 21 MHz in hcp and bcc $^3$He and its interaction with dislocations," Physical Review B **26** (11), 6104.
Beamish, JR, and JP Franck (1983), "Pinning of dislocations in hcp and bcc $^3$He by stress waves and by $^4$He impurities," Physical Review B **28** (3), 1419.
Beamish, JR, A Hikata, L Tell, and C Elbaum (1983), "Solidification and superfluidity of $^4$He in porous Vycor glass," Physical Review Letters **50** (6), 425.
Beamish, JR, N Mulders, A Hikata, and C Elbaum (1991), "Vacancy diffusion and stress relaxation in $^4$He freezing in porous Vycor," Physical Review B **44** (17), 9314.
Benedek, Giorgio, Anton Kalinin, Pablo Nieto, and J Peter Toennies (2016), "Vacancy-induced flow of solid helium," Physical Review B **93** (10), 104505.
Bennemann, Karl Heinz, and John Boyd Ketterson (1976), "Physics of liquid and solid helium. part I," .
Berberich, P, P Leiderer, and S Hunklinger (1975), "Investigation of the lifetime of longitudinal phonons at GHz frequencies in liquid and solid $^4$He," Journal of Low Temperature Physics **22** (1), 61–84.
Berent, Inon, and Emil Polturak (1998), "Critical behavior of the shear resistance of solid $^4$He near a structural phase transition," Physical Review Letters **81** (4), 846.
Bernier, ME, and JH Hetherington (1989), "Vacancies in solid $^3$He," Physical Review B **39** (16), 11285.
Bernu, B, and DM Ceperley (2005), "Path integral calculations of exchange in solid $^4$He," Journal of Physics and Chemistry of Solids **66** (8-9), 1462–1466.
Birchenko, AP, NP Mikhin, E Ya Rudavskii, SN Smirnov, and Ya Yu Fysun (2018), "Pressure relaxation and diffusion of vacancies in rapidly grown helium crystals," Low Temperature Physics **44** (4), 304–316.
Blackburn, E, JM Goodkind, SK Sinha, J Hudis, C Broholm, J van Duijn, CD Frost, O Kirichek, and RBE Down (2007), "Absence of a low-temperature anomaly in the Debye-Waller factor of solid $^4$He down to 140 mK," Physical Review B **76** (2), 024523.
Bodensohn, Joachim, Klaus Nicolai, and Paul Leiderer (1986), "The growth of atomically rough $^4$He crystals," Zeitschrift für Physik B Condensed Matter **64** (1), 55–64.
Bonfait, G, H Godfrin, and B Castaing (1989), "Solid $^4$He: search for superfluidity," Journal de Physique **50** (15), 1997–2002.
Boninsegni, M, AB Kuklov, L Pollet, NV Prokof'ev, BV Svistunov, and M Troyer (2007), "Luttinger liquid in the core of a screw dislocation in helium-4," Physical Review Letters **99** (3), 035301.
Boninsegni, Massimo, AB Kuklov, Lode Pollet, NV Prokof'ev, BV Svistunov, and Matthias Troyer (2006a), "Fate of vacancy-induced supersolidity in $^4$He," Physical Review Letters **97** (8), 080401.
Boninsegni, Massimo, Nikolay Prokof'ev, and Boris Svistunov (2006b), "Worm algorithm for continuous-space path integral monte carlo simulations," Physical Review Letters **96** (7), 070601.
Borda, Edgar Josué Landinez, Wei Cai, and Maurice de Koning (2014), "Ideal shear strength of a quantum crystal," Physical Review Letters **112** (15), 155303.
Borda, Edgar Josué Landinez, Wei Cai, and Maurice de Koning (2016), "Dislocation structure and mobility in hcp $^4$He," Physical Review Letters **117** (4), 045301.
Bukhari, Syed, Md Islam, Ariel Haziot, and John Beamish (2014), "Shear piezoelectric coefficients of PZT, $LiNbO_3$ and PMN-PT at cryogenic temperatures," in *Journal of Physics: Conference Series*, Vol. 568 (IOP Publishing) p. 032004.
Burns, CA, N Mulders, L Lurio, MHW Chan, A Said, CN Kodituwakku, and PM Platzman (2008), "X-ray studies of low-temperature solid $^4$He," Physical Review B **78** (22), 224305.
Burns, Clement A, and John M Goodkind (1994), "Vacancies in solid $^4$He: Conflicting experimental evidence," Journal of Low Temperature Physics **95** (5-6), 695–714.
Cai, Wei, and William D Nix (2016), *Imperfections in crystalline solids* (Cambridge University Press).
Cazorla, C, Y Lutsyshyn, and J Boronat (2012), "Elastic constants of solid $^4$He under pressure: Diffusion monte carlo study," Physical Review B **85** (2), 024101.
Ceperley, David M (1995), "Path integrals in the theory of condensed helium," Reviews of Modern Physics **67** (2), 279.
Ceperley, David M, and EL Pollock (1986), "Path-integral computation of the low-temperature properties of liquid $^4$He," Physical Review Letters **56** (4), 351.
Ceperley, DM, and G Jacucci (1987), "Calculation of exchange frequencies in bcc $^3$He with the path-integral monte carlo method," Physical Review Letters **58** (16), 1648.
Cheng, Zhi Gang, and John Beamish (2016), "Compression-driven mass flow in bulk solid $^4$He," Physical Review Letters **117** (2), 025301.
Cheng, Zhi Gang, and John Beamish (2017), "Defect motion in a quantum solid with spin: hcp $^3$He," Physical Review B **95** (18), 180103.
Cheng, Zhi Gang, and John Beamish (2018a), "Mass flow through solid $^3$He in the bcc phase," Physical Review Letters **121**, 225304.
Cheng, Zhi Gang, and John Beamish (2018b), "Plastic deformation in a quantum solid: Dislocation avalanches and creep in helium," Physical Review Letters **121** (5), 055301.
Cheng, Zhi Gang, Fabien Souris, and John Beamish (2016), "Shear modulus and dislocations in bcc solid $^3$He," Journal of Low Temperature Physics **183** (3-4), 99–105.
Chester, GV (1970), "Speculations on Bose-Einstein condensation and quantum crystals," Physical Review A **2** (1), 256.
Choi, Jaewon, Jaeho Shin, and Eunseong Kim (2015), "Frequency-dependent study of solid $^4$He contained in a rigid double-torus torsional oscillator," Physical Review B **92** (14), 144505.
Clark, Bryan K, and David M Ceperley (2008), "Path integral calculations of vacancies in solid helium," Computer Physics Communications **179** (1-3), 82–88.
Corboz, P, L Pollet, NV Prokof'ev, and M Troyer (2008), "Binding of a $^3$He impurity to a screw dislocation in solid $^4$He," Physical Review Letters **101** (15), 155302.
Crepeau, Richard Hanes, O Heybey, DM Lee, and Stanley A Strauss (1971), "Sound propagation in hcp solid helium

crystals of known orientation," Physical Review A **3** (3), 1162.
Dash, JG, and JS Wettlaufer (2005), "Classical rotational inertia of solid $^4$He," Physical Review Letters **94** (23), 235301.
Day, James, and John Beamish (2006), "Pressure-driven flow of solid helium," Physical Review Letters **96** (10), 105304.
Day, James, and John Beamish (2007a), "Flow of solid $^4$He near melting," Journal of Low Temperature Physics **148** (5-6), 683–687.
Day, James, and John Beamish (2007b), "Low-temperature shear modulus changes in solid $^4$He and connection to supersolidity," Nature **450** (7171), 853.
Day, James, and John Beamish (2012), "Acoustic resonances and non-linearity in solid $^4$He," Journal of Low Temperature Physics **166** (1-2), 33–48.
Day, James, Tobias Herman, and John Beamish (2005), "Freezing and pressure-driven flow of solid helium in Vycor," Physical Review Letters **95** (3), 035301.
Day, James, Oleksandr Syshchenko, and John Beamish (2009), "Intrinsic and dislocation-induced elastic behavior of solid helium," Physical Review B **79** (21), 214524.
Day, James, Oleksandr Syshchenko, and John Beamish (2010), "Nonlinear elastic response in solid helium: critical velocity or strain?" Physical Review Letters **104** (7), 075302.
Degtyarev, IA, AA Lisunov, VA Maidanov, V Yu Rubanskiy, SP Rubets, E Ya Rudavskii, AS Rybalko, and VA Tikhii (2010), "Formation of a disordered (glassy) phase in deformed solid $^4$He in the region of supersolid state," Journal of Experimental and Theoretical Physics **111** (4), 619–626.
Dobbs, ER (2000), *Helium three* (Oxford University Press).
Eckert, J, W Thomlinson, and G Shirane (1977), "Lattice dynamics of fcc helium at high pressure," Physical Review B **16** (3), 1057.
Eckert, J, W THomlinson, and G Shirane (1978), "Lattice dynamics of hcp $^4$He at high pressure," Physical Review B **18** (7), 3071.
Eckstein, Y, J. Landau, S. G. Lipson, and Z. Olami (1980), "Role of substrate symmetry in nucleating solid helium," Physical Review Letters **45**, 1805–1808.
Edwards, DO, and S. Balibar (1989), "Calculation of the phase diagram of $^3$He-$^4$He solid and liquid mixtures," Physical Review B **39**, 4083–4097.
Edwards, DO, AS McWilliams, and JG Daunt (1962), "Phase separation in solid $^3$He -$^4$He mixtures, as shown by specific heat measurements," Physical Review Letters **9** (5), 195.
Edwards, DO, S Mukherjee, and MS Pettersen (1990), "Quantum kinks and the growth resistance of atomically rough $^4$He crystals," Physical Review Letters **64** (8), 902.
Edwards, DO, MS Pettersen, and H Baddar (1991), "The inertia of the $^4$He crystal surface and the calculation of the phonon transmission," in *Excitations in Two-Dimensional and Three-Dimensional Quantum Fluids* (Springer) pp. 361–374.
Fartash, Arjang, and John M Goodkind (1986), "Acoustic properties of solid $^3$He at low temperatures," Physical Review Letters **56** (13), 1389.
Fefferman, AD, Fabien Souris, Ariel Haziot, JR Beamish, and Sebastien Balibar (2014), "Dislocation networks in $^4$He crystals," Physical Review B **89** (1), 014105.
Fraass, BA, PR Granfors, and RO Simmons (1989), "X-ray measurements of thermal vacancies in hcp $^4$He," Physical Review B **39** (1), 124.
Franck, JP (1980), "Calorimetric study of the transition between the close-packed phases of $^4$He from the triple point to 3.9 kbar," Physical Review B **22** (9), 4315.
Franck, JP, KE Kornelsen, and JR Manuel (1983), "Wetting of fcc $^4$He grain boundaries by fluid $^4$He," Physical Review Letters **50** (19), 1463.
Franck, JP, and R Wanner (1970), "Elastic constants of hcp $^4$He," Physical Review Letters **25** (6), 345.
Friedel, J (1964), *Dislocations* (Pergamon Press).
Gallet, F, PE Wolf, and S Balibar (1984), "Liquid-solid $^4$He interfacial tension: Temperature variation near the superfluid transition," Physical Review Letters **52** (25), 2253.
Gardner, WR, JK Hoffer, and NE Phillips (1973), "Thermodynamic properties of $^4$He. the hcp phase at low densities," Physical Review A **7** (3), 1029.
Gessner, Oliver, and Andrey F Vilesov (2019), "Imaging quantum vortices in superfluid helium droplets," Annual review of physical chemistry **70**, 173–198.
Glyde, HR (1976), "Rare Gas Solids vol 7, eds. ML Klein and JA Venables,".
Gomez, Luis F, Ken R Ferguson, James P Cryan, Camila Bacellar, Rico Mayro P Tanyag, Curtis Jones, Sebastian Schorb, Denis Anielski, Ali Belkacem, Charles Bernando, *et al.* (2014), "Shapes and vorticities of superfluid helium nanodroplets," Science **345** (6199), 906–909.
Gorman, J A, D. S. Wood, and T. Vreeland Jr. (1969), "Mobility of dislocations in aluminum," Journal of Applied Physics **40** (2), 833–841.
Granato, A v, and Kurt Lücke (1956), "Theory of mechanical damping due to dislocations," Journal of Applied Physics **27** (6), 583–593.
Granato, AV, and Kurt Lücke (1981), "Temperature dependence of amplitude-dependent dislocation damping," Journal of Applied Physics **52** (12), 7136–7142.
Granfors, PR, BA Fraass, and RO Simmons (1987), "Direct measurements of thermal vacancies in bcc $^4$He," Journal of Low Temperature Physics **67** (5-6), 353–375.
Greywall, Dennis Stanley (1971), "Sound propagation in x-ray-oriented single crystals of hcp helium-4 and bcc helium-3," Physical Review A **3** (6), 2106.
Greywall, DS (1975), "Elastic constants and Debye temperature of bcc $^3$He," Physical Review B **11** (3), 1070.
Greywall, DS (1976), "Elastic constants of bcc $^4$He," Physical Review B **13** (3), 1056.
Greywall, DS (1977a), "Elastic constants of hcp $^4$He," Physical Review B **16** (11), 5127.
Greywall, DS (1977b), "Search for superfluidity in solid $^4$He," Physical Review B **16** (3), 1291.
Greywall, DS (1977c), "Specific heat of bcc $^3$He," Physical Review B **15** (5), 2604.
Grigor'ev, VN (1997), "Diffusion in solid helium (a review)," Low Temperature Physics **23** (1), 3–14.
Grilly, ER (1971), "Pressure-volume-temperature relations in liquid and solid $^3$He," Journal of Low Temperature Physics **4** (6), 615–635.
Grilly, ER (1973), "Pressure-volume-temperature relations in liquid and solid $^4$He," Journal of Low Temperature Physics **11** (1-2), 33–52.
Grilly, ER, and RL Mills (1962), "PVT relations in $^4$He near the melting curve and the $\lambda$-line," Annals of Physics **18** (2), 250–263.
Guyer, RA, RC Richardson, and LI Zane (1971), "Excitations in quantum crystals (a survey of NMR experiments in solid helium)," Reviews of Modern Physics **43** (4), 532.

Hallock, RB (2015), "Solid $^4$He: Progress, status, and outlook for mass flux measurements," Journal of Low Temperature Physics **180** (1-2), 6–19.

Hallock, RB (2019), "Mass flux experiments in solid $^4$He: some history, recent work and the current status," Journal of Low Temperature Physics , 1–21.

Haziot, Ariel, Andrew D Fefferman, John R Beamish, and Sébastien Balibar (2013a), "Dislocation densities and lengths in solid $^4$He from elasticity measurements," Physical Review B **87** (6), 060509.

Haziot, Ariel, Andrew D Fefferman, Fabien Souris, John R Beamish, Humphrey J Maris, and Sébastien Balibar (2013b), "Critical dislocation speed in helium-4 crystals," Physical Review B **88** (1), 014106.

Haziot, Ariel, Xavier Rojas, Andrew D Fefferman, John R Beamish, and Sébastien Balibar (2013c), "Giant plasticity of a quantum crystal," Physical Review Letters **110** (3), 035301.

Haziot, Ariel, Xavier Rojas, Andrew D Fefferman, John R Beamish, and Sébastien Balibar (2013d), "Haziot et al. reply," Physical Review Letters **111** (11), 119602.

Heald, SM, DR Baer, and RO Simmons (1983), "X-ray diffraction study of thermal vacancies in solid helium-3," Solid state communications **47** (10), 807–810.

Heald, SM, DR Baer, and RO Simmons (1984), "Thermal vacancies in solid $^3$He," Physical Review B **30** (5), 2531.

Hendry, PC, and Peter VE McClintock (1987), "Continuous flow apparatus for preparing isotopically pure $^4$He," Cryogenics **27** (3), 131–138.

Heybey, OW, and DM Lee (1967), "Optical birefringence and crystal growth of hexagonal-close-packed $^4$He from superfluid helium," Physical Review Letters **19** (3), 106.

Hirth, JP, and J Lothe (1982), *Theory of Dislocations, 2nd ed.* (Wiley).

Hoffer, JK, WR Gardner, CG Waterfield, and NE Phillips (1976), "Thermodynamic properties of $^4$He. ii. the bcc phase and the P-T and V-T phase diagrams below 2 K," Journal of Low Temperature Physics **23** (1-2), 63–102.

Hull, Derek, and David J Bacon (2011), *Introduction to Dislocations* (Elsevier).

Islam, Md Shahidul, and John Beamish (2018), "Shear piezoelectric and dielectric properties of $LiNbO_3$, PMN-PT and PZT-5A at low temperatures," Journal of Low Temperature Physics , 1–17.

Iwasa, I (2013), "Dislocation-pinning mechanism for the hysteresis of torsional-oscillator experiments on solid helium," Journal of Low Temperature Physics **171** (3-4), 287–294.

Iwasa, Izumi (2002), "Dislocation image on x-ray topographs within kinematical theory," Physical Review B **66** (14), 144111.

Iwasa, Izumi, Keisuke Araki, and Hideji Suzuki (1979), "Temperature and frequency dependence of the sound velocity in hcp $^4$He crystals," Journal of the Physical Society of Japan **46** (4), 1119–1126.

Iwasa, Izumi, and Harry Kojima (2017), "Nonlinear ultrasound propagation in solid $^4$He compared with shear modulus experiments," Journal of Low Temperature Physics **187** (5-6), 459–467.

Iwasa, Izumi, and Hideji Suzuki (1980), "Sound velocity and attenuation in hcp $^4$He crystals containing $^3$He impurities," Journal of the Physical Society of Japan **49** (5), 1722–1730.

Iwasa, Izumi, and Hideji Suzuki (1982), "Temperature dependence of the sound velocity in bcc $^3$He crystals," Journal of the Physical Society of Japan **51** (7), 2116–2122.

Iwasa, Izumi, Hideji Suzuki, Tetsuo Nakajima, Shigeo Suzuki, Masami Ando, Ichiro Yonenaga, Masahiro Takebe, and Koji Sumino (1987), "Observation of lattice defects in solid helium by SR X-ray topography," Journal of the Physical Society of Japan **56** (12), 4225–4228.

Iwasa, Izumi, Hideji Suzuki, Takayoshi Suzuki, Tetsuo Nakajima, Ichiro Yonenaga, Haruhiko Suzuki, Hirokazu Koizumi, Yuji Nishio, and Joji Ota (1995), "Subboundaries in hcp $^4$He crystals studied by SR X-ray topography," Journal of Low Temperature Physics **100** (1-2), 147–165.

Kamimura, Y, K Edagawa, and S Takeuchi (2013), "Experimental evaluation of the Peierls stresses in a variety of crystals and their relation to the crystal structure," Acta Materialia **61** (1), 294–309.

Kang, Evan SH, Duk Y Kim, Hyoung Chan Kim, and Eunseong Kim (2013), "Stress-and temperature-dependent hysteresis of the shear modulus of solid helium," Physical Review B **87** (9), 094512.

Kang, Evan SH, Hongkee Yoon, and Eunseong Kim (2015), "Modified Granato-Lucke theory with pinning length distribution in solid $^4$He," Journal of the Physical Society of Japan **84**, 034602.

Keesom, W H (1926), "Solid helium," Leiden Communications , 184b.

Keesom, WH, and KW Taconis (1938), "On the structure of solid helium," Physica **5** (3), 161–169.

Keller, William E (1969), *Helium-3 and Helium-4* (Plenum).

Keshishev, KO, A Ya Parshin, and AV Babkin (1979), "Experimental detection of crystallization waves in $^4$He," JETP Lett **30** (1).

Keshishev, KO, A Ya Parshin, and AV Babkin (1981), "Crystallization waves in $^4$He," Zhurnal Ehksperimental'noj i Teoreticheskoj Fiziki **80** (2), 716–728.

Keshishev, Konstantin, and Olga Andreeva (1991), "Anisotropy of surface stiffness, growth kinetics and roughening transition in $^4$He," in *Excitations in two-dimensional and three-dimensional quantum fluids* (Springer) pp. 387–395.

Keyse, RJ, and JA Venables (1985), "Stacking fault energy and crystal stability of solid krypton and xenon," Journal of Physics C: Solid State Physics **18** (23), 4435.

Kim, Duk Y, and Moses HW Chan (2012), "Absence of supersolidity in solid helium in porous Vycor glass," Physical Review Letters **109** (15), 155301.

Kim, DY, Hyoungsoon Choi, W Choi, S Kwon, Eunseong Kim, and HC Kim (2011), "Unaffected nonclassical response of solid $^4$He under elastic modulus variation," Physical Review B **83** (5), 052503.

Kim, Eunseong, and MHW Chan (2004a), "Probable observation of a supersolid helium phase," Nature **427** (6971), 225.

Kim, Eunseong, and Moses HW Chan (2004b), "Observation of superflow in solid helium," Science **305** (5692), 1941–1944.

Kim, SS, C Huan, L Yin, JS Xia, D Candela, and NS Sullivan (2013), "Nmr investigation of the low-temperature dynamics of solid $^4$He doped with $^3$He impurities," Physical Review B **87** (22), 224303.

Klein, ML, and GK Horton (1972), "The rise of self-consistent phonon theory," Journal of Low Temperature Physics **9** (3-4), 151–166.

Kuklov, AB (2019), "Plasticity induced superclimb in solid He-4: Direct and inverse effects," Physical Review B **100** (1), 014513.

Landau, J, SG Lipson, LM Määttänen, LS Balfour, and DO Edwards (1980), "Interface between superfluid and solid $^4$He," Physical Review Letters **45** (1), 31.

Lebyodkin, M A, T. A. Lebedkina, F. Chmelík, T. T. Lamark, Y. Estrin, C. Fressengeas, and J. Weiss (2009), "Intrinsic structure of acoustic emission events during jerky flow in an Al alloy," Physical Review B **79**, 174114.

Leggett, Anthony J (1970), "Can a solid be "superfluid"?" Physical Review Letters **25** (22), 1543.

Legrand, Par B (1984), "Relations entre la structure électronique et la facilité de glissement dans les métaux hexagonaux compacts," Philosophical Magazine B **49** (2), 171–184.

Lengua, Gabriel A, and John M Goodkind (1990), "Elementary excitations and a collective mode in hcp $^4$He," Journal of Low Temperature Physics **79** (5-6), 251–287.

Levchenko, AA, and LP Mezhov-Deglin (1982), "Thermal conductivity of perfect and plastically deformed $^4$He crystals grown in a narrow bent capillary," Zhurnal Ehksperimental'noj i Teoreticheskoj Fiziki **82** (1), 278–292.

Levchenko, AA, and LP Mezhov-Deglin (1984), "The annealing of freshly induced defects in $^4$He crystals," Zhurnal Ehksperimental'noj i Teoreticheskoj Fiziki **86**, 2123–2133.

Lipschultz, FP, and DM Lee (1965), "Shear waves in solid $^4$He," Physical Review Letters **14** (25), 1017.

Lisunov, A, V Maidanov, N Mikhin, A Neoneta, V Rubanskyi, S Rubets, E Rudavskii, and V Zhuchkov (2014), "The plastic flow of solid $^4$He through a porous membrane," Journal of Low Temperature Physics **175** (1-2), 113–119.

Lisunov, A, V Maidanov, V Rubanskyi, S Rubets, E Rudavskii, S Smirnov, and V Zhuchkov (2015), "Thermally activated and quantum plasticity of solid $^3$He at temperatures below 0.5 K," Physical Review B **92** (14), 140505.

Lisunov, AA, VA Maidanov, V Yu Rubanskyi, SP Rubets, E Ya Rudavskii, and SN Smirnov (2016), "Plastic flow of solid $^3$He through a porous elastic film," Low Temperature Physics **42** (12), 1075–1093.

Lücke, K, AV Granato, and LJ Teutonico (1968), "Thermally assisted unpinning of a dislocation double loop," Journal of Applied Physics **39** (11), 5181–5191.

Maass, R, and PM Derlet (2018), "Micro-plasticity and recent insights from intermittent and small-scale plasticity," Acta Materialia **143**, 338–363.

Manninen, A J, J. P. Pekola, G. M. Kira, J. P. Ruutu, A. V. Babkin, H. Alles, and O. V. Lounasmaa (1992), "First optical observations of superfluid $^3$He," Physical Review Letters **69**, 2392–2395.

Manning, MB, MJ Moelter, and C Elbaum (1986), "Plastic deformation, vacancy diffusion, and vacancy delocalization in bcc $^3$He," Physical Review B **33** (3), 1634.

Maris, Humphrey J (1971), "Interaction of sound waves with thermal phonons in dielectric crystals," in *Physical acoustics*, Vol. 8 (Academic Press) pp. 279–345.

Maris, Humphrey J (2012), "Effect of elasticity on torsional oscillator experiments probing the possible supersolidity of helium," Physical Review B **86** (2), 020502.

Maris, Humphrey J, and Sebastien Balibar (2010), "Elastic properties of polycrystalline solid helium," Journal of Low Temperature Physics **160** (1-2), 5–11.

Maris, Humphrey J, and Sebastien Balibar (2011), "Effect of helium elasticity on torsional oscillator measurements," Journal of Low Temperature Physics **162** (1-2), 12–22.

McGreer, K, and JP Franck (1990), "Temperature dependence of elastic constants: a material-independent parameter and data in hcp $^4$He," Physical Review B **41** (1), 162.

Mezhov-Deglin, LP (1966), "Measurement of the thermal conductivity of crystalline $^4$He," Soviet Physics JETP **22**, 47–56.

Miura, Y, K Mori, and T Mamiya (2000a), "Dislocation damping in bcc solid $^3$He at small strain amplitude," Physica B: Condensed Matter **284**, 357–358.

Miura, Y, K Ogawa, K Mori, and T Mamiya (2000b), "Pinning mechanism of the dislocation lines in bcc solid $^3$He," Journal of Low Temperature Physics **121** (5-6), 689–693.

Miura, Yuichi, Tetsumasa Nakayasu, Takayoshi Mamiya, and Hideharu Kato (1998), "Dislocation motion in bcc solid $^3$He," Journal of Low Temperature Physics **110** (1-2), 115–119.

Molz, Eric B, and John R Beamish (1995), "Freezing and melting of helium in different porous media," Journal of Low Temperature Physics **101** (5-6), 1055–1077.

Mukharsky, Y, and A Penzev (2012), "Elastic and acoustic measurements in solid $^4$He," Journal of Low Temperature Physics **169** (3-4), 197–207.

Mukharsky, Yu, A Penzev, and E Varoquaux (2009), "Low-frequency acoustics in solid $^4$He at low temperature," Physical Review B **80** (14), 140504.

Mumm, HP, MG Huber, W Bauder, N Abrams, CM Deibel, CR Huffer, PR Huffman, KW Schelhammer, R Janssens, CL Jiang, *et al.* (2016), "High-sensitivity measurement of $^3$He -$^4$He isotopic ratios for ultracold neutron experiments," Physical Review C **93** (6), 065502.

Ninomiya, Toshiyuki (1974), "Frictional force acting on a dislocation - fluttering mechanism," Journal of the Physical Society of Japan **36** (2), 399–405.

Nomura, R, M Yamaguchi, K Takaoka, X Xu, Y Sasaki, and T Mizusaki (2000), "Sound velocity measurements of nuclear-ordered solid $^3$He along the melting curve," Physical Review Letters **85** (14), 2977–2980.

Nowick, Arthur S, and B S Berry (1972), *Anelastic relaxation in crystalline solids* (Academic Press).

Osborne, DW, BM Abraham, and B Weinstock (1951), "Solidification of $^3$He," Physical Review **82** (2), 263.

Osborne, DW, B. Weinstock, and B. Abraham (1949), "Comparison of flow of isotopically pure liquid $^3$He and $^4$He," Physical Review **75**, 988.

Osheroff, DD (1992), "Nuclear magnetic order in solid $^3$He," Journal of Low Temperature Physics **87** (3-4), 297–342.

Oxburgh, ER, RK O'nions, and RI Hill (1986), "Helium isotopes in sedimentary basins," Nature **324** (6098), 632.

Paalanen, MA, DJ Bishop, and HW Dail (1981), "Dislocation motion in hcp $^4$He," Physical Review Letters **46** (10), 664.

Pantalei, Claudia, Xavier Rojas, David O Edwards, Humphrey J Maris, and Sébastien Balibar (2010), "How to prepare an ideal helium 4 crystal," Journal of Low Temperature Physics **159** (3-4), 452–461.

Pelleg, O, M Shay, SG Lipson, E Polturak, J Bossy, JC Marmeggi, K Horibe, E Farhi, and A Stunault (2006), "Observation of macroscopic structural fluctuations in bcc solid $^4$He," Physical Review B **73** (2), 024301.

Pessoa, Renato, M de Koning, and SA Vitiello (2012), "Elastic constants and supersolidity in solid hcp $^4$He," arXiv preprint arXiv:1203.0456.

Poirier, Jean-Paul (1985), *Creep of crystals: high-temperature deformation processes in metals, ceramics and minerals* (Cambridge University Press).

Pollet, L, M Boninsegni, AB Kuklov, NV Prokof'ev, BV Svistunov, and M Troyer (2007), "Superfluidity of grain

boundaries in solid $^4$He," Physical Review Letters **98** (13), 135301.

Pollet, L, M Boninsegni, AB Kuklov, NV Prokof'ev, BV Svistunov, and M Troyer (2008), "Local stress and superfluid properties of solid $^4$He," Physical Review Letters **101** (9), 097202.

Pollock, EL, and David M Ceperley (1987), "Path-integral computation of superfluid densities," Physical Review B **36** (16), 8343.

Pratt, EJ, B Hunt, V Gadagkar, M Yamashita, MJ Graf, AV Balatsky, and JC Davis (2011), "Interplay of rotational, relaxational, and shear dynamics in solid $^4$He," Science **332** (6031), 821–824.

Prokof'ev, Nikolay, and Boris Svistunov (2005), "Supersolid state of matter," Physical Review Letters **94** (15), 155302.

Ramesh, S, Q. Zhang, G. Torzo, and J. D. Maynard (1984), "Experimental observation of the increase of the two-dimensional critical temperature in multilayer adsorption," Physical Review Letters **52**, 2375–2378.

Ray, MW, and RB Hallock (2008), "Observation of unusual mass transport in solid hcp $^4$He," Physical Review Letters **100** (23), 235301.

Ray, MW, and RB Hallock (2009), "Observation of mass flux through hcp $^4$He off the melting curve," in *Journal of Physics: Conference Series*, Vol. 150 (IOP Publishing) p. 032087.

Reese, RA, SK Sinha, TO Brun, and CR Tilford (1971), "Phonon dispersion relations for hcp $^4$He at a molar volume of 16 cm$^3$," Physical Review A **3** (5), 1688.

Reppy, John D, Xiao Mi, Alexander Justin, and Erich J Mueller (2012), "Interpreting torsional oscillator measurements: Effect of shear modulus and supersolidity," Journal of Low Temperature Physics **168** (3-4), 175–193.

Richeton, Thiebaud, Jerome Weiss, and Francois Louchet (2005), "Dislocation avalanches: Role of temperature, grain size and strain hardening," Acta Materialia **53** (16), 4463 – 4471.

Rittner, Ann Sophie C, and John D Reppy (2007), "Disorder and the supersolid state of solid $^4$He," Physical Review Letters **98** (17), 175302.

Rittner, Ann Sophie C, and John D Reppy (2009), "Pressure relaxations in solid helium-4," in *Journal of Physics: Conference Series*, Vol. 150 (IOP Publishing) p. 032089.

Rojas, Xavier, Ariel Haziot, Victor Bapst, Sébastien Balibar, and Humphrey J Maris (2010), "Anomalous softening of $^4$He crystals," Physical Review Letters **105** (14), 145302.

Rolley, E, S Balibar, and F Gallet (1986), "The first roughening transition of $^3$He crystals," EPL (Europhysics Letters) **2** (3), 247.

Rolley, E, S Balibar, F Gallet, F Graner, and C Guthmann (1989), "The surface tension of bcc $^3$He crystals," EPL (Europhysics Letters) **8** (6), 523.

Rolley, E, S Balibar, C Guthmann, and P Nozieres (1995a), "Adsorption of $^3$He on $^4$He crystal surfaces," Physica B: Condensed Matter **210** (3-4), 397–402.

Rolley, E, C Guthmann, E Chevalier, and S Balibar (1995b), "The static and dynamic properties of vicinal surfaces on helium 4 crystals," Journal of Low Temperature Physics **99** (5-6), 851–886.

Rolley, Etienne, Sébastien Balibar, and François Graner (1994a), "Growth shape of $^3$He needle crystals," Physical Review E **49** (2), 1500.

Rolley, Etienne, Eric Chevalier, Claude Guthmann, and Sébastien Balibar (1994b), "Stepped surfaces of hcp helium-4 crystals," Physical Review Letters **72**, 872–875.

Rubanskyi, Valentyn, and Robert Hallock (2019), "Mass flux measurements in solid $^4$He." APS **2019**, V06–004.

Ruutu, JP, P.J. Hakonen, and A.V. Babkin (1998), "Growth of $^4$He crystals at mK temperatures," Journal of Low Temperature Physics **112**, 117–164.

Ruutu, JP, P.J. Hakonen, J.S. Penttila, A.V. Babkin, J.P. Saramaki, and E.B. Sonin (1996), "Evidence of $^4$He crystallization via quantum tunneling at mK temperatures," Physical Review Letters **77**, 2514–2517.

Sakai, Akira, Yasushiro Nishioka, and Hideji Suzuki (1979), "Plastic flow in bcc $^3$He," Journal of the Physical Society of Japan **46** (3), 881–888.

Sanders, DJ, H Kwun, A Hikata, and C Elbaum (1977), "Plastic deformation of free-standing crystals of hcp $^4$He," Physical Review Letters **39** (13), 815.

Sanders, DJ, H Kwun, A Hikata, and C Elbaum (1978), "Plastic deformation of bcc $^4$He," Physical Review Letters **40** (7), 458.

Sasaki, S, Caupin F, and S. Balibar (2008), "Optical observations of disorder in solid helium 4," Journal of Low Temperature Physics **153**, 43–76.

Sasaki, Satoshi, Frédéric Caupin, and Sébastien Balibar (2007), "Wetting properties of grain boundaries in solid $^4$He," Physical Review Letters **99** (20), 205302.

Sasaki, Satoshi, Frédéric Caupin, and Sébastien Balibar (2008), "Optical observations of disorder in solid helium 4," Journal of Low Temperature Physics **153** (3-4), 43–76.

Schaarwachter, W, and H. Ebener (1990), "Acoustic emission: A probe into dislocation dynamics in plasticity," Acta Metallurgica et Materialia **38** (2), 195 – 205.

Schoffel, P, and MH Muser (2001), "Elastic constants of quantum solids by path integral simulations," Physical Review B **63**, 224108.

Schuch, AF, E.R. Grilly, and R.L. Mills (1958), "Structure of the $\alpha$ and $\beta$ forms of solid $^3$He," Phys. Rev. **110**, 775.

Shal'nikov, AI (1962), "Measurement of the thermal conductivity of crystalline $^4$He," Soviet Physics JETP **14**, 753–754.

Shashkov, IV, M.A. Lebyodkin, and T.A. Lebedkina (2012), "Multiscale study of acoustic emission during smooth and jerky flow in an AlMg alloy," Acta Materialia **60** (19), 6842 – 6850.

Shin, Jaeho, and Moses HW Chan (2019), "Mass transport through dislocation network in solid $^4$He," Physical Review B **99** (14), 140502.

Shin, Jaeho, Jaewon Choi, Keiya Shirahama, and Eunseong Kim (2016), "Simultaneous investigation of shear modulus and torsional resonance of solid $^4$He," Physical Review B **93** (21), 214512.

Shin, Jaeho, Duk Y Kim, Ariel Haziot, and Moses HW Chan (2017), "Superfluidlike mass flow through 8 $\mu$m thick solid $^4$He samples," Physical Review Letters **118** (23), 235301.

Simmons, RO (1994), "Thermal vacancies in quantum solid heliums," Journal of Physics and Chemistry of Solids **55** (10), 895–906.

Souris, F, AD Fefferman, A Haziot, N Garroum, JR Beamish, and S Balibar (2015), "Search for dislocation free helium crystals," Journal of Low Temperature Physics **178** (3-4), 149–161.

Souris, Fabien, Andrew D Fefferman, Humphrey J Maris, Vincent Dauvois, Philippe Jean-Baptiste, John R Beamish, and Sébastien Balibar (2014), "Movement of dislocations dressed with $^3$He impurities in $^4$He crystals," Physical Re-

view B **90** (18), 180103.
Souris, Fabien, Xavier Rojas, Paul H Kim, and John P Davis (2017), "Ultralow-dissipation superfluid micromechanical resonator," Physical Review Applied **7** (4), 044008.
Straty, G C, and E. D. Adams (1966a), "$^4$He melting curve below 1 K," Physical Review Letters **17**, 290–292.
Straty, GC, and ED Adams (1966b), "Pvt measurements of the hcp-bcc phase transition in solid $^3$He," Physical Review **150** (1), 123.
Suhel, A, and JR Beamish (2011), "Pressure gradients in solid $^4$He: Thermal quenching and annealing," Physical Review B **84** (9), 094512.
Suzuki, Hideji (1973), "Plastic flow in solid helium," Journal of the Physical Society of Japan **35** (5), 1472–1479.
Suzuki, Hideji (1977), "Plastic flow in hcp $^4$He: II," Journal of the Physical Society of Japan **42** (6), 1865–1872.
Suzuki, Taira, Shin Takeuchi, and Hideo Yoshinaga (2013), *Dislocation dynamics and plasticity*, Vol. 12 (Springer Science & Business Media).
Syshchenko, Oleksandr, James Day, and John Beamish (2010), "Frequency dependence and dissipation in the dynamics of solid helium," Physical Review Letters **104** (19), 195301.
Takeuchi, Shin, and Ali S Argon (1979), "Glide and climb resistance to the motion of an edge dislocation due to dragging a Cottrell atmosphere," Philosophical Magazine A **40** (1), 65–75.
Thomlinson, W, J Eckert, and G Shirane (1978), "Inelastic neutron scattering from high-density fcc $^4$He," Physical Review B **18** (3), 1120.
Thompson, DO, and DK Holmes (1959), "Dislocation contribution to the temperature dependence of the internal friction and Young's modulus of copper," Journal of Applied Physics **30** (4), 525–541.
Todoshchenko, Igor A, Harry Alles, Heikki J Junes, Alexander Ya Parshin, and Viktor Tsepelin (2005), "Measurements on the surface tension of $^3$He crystals near 100 mK," Journal of Low Temperature Physics **138** (3-4), 811–816.
Treiner, J (1993), "Helium mixtures on weak binding substrates," Journal of Low Temperature Physics **92** (1-2), 1–9.
Trickey, SB, WP Kirk, and ED Adams (1972), "Thermodynamic, elastic, and magnetic properties of solid helium," Reviews of Modern Physics **44** (4), 668.
Tsepelin, Viktor, Harry Alles, A Babkin, JPH Härme, Reyer Jochemsen, A Ya Parshin, and G Tvalashvili (2001), "Observation of higher order facets on $^3$He crystals," Physical Review Letters **86** (6), 1042.
Tsepelin, Viktor, Harry Alles, Alexei Babkin, Reyer Jochemsen, Alexander Ya. Parshin, and Igor A. Todoshchenko (2002), "Morphology and growth kinetics of $^3$He crystals below 1 mK," Journal of Low Temperature Physics **129**, 489–530.
Tsuruoka, Fujio, and Yosio Hiki (1979), "Ultrasonic attenuation and dislocation damping in helium crystals," Physical Review B **20** (7), 2702.
Tsymbalenko, VL (1976), "Plastic flow of crystalline $^4$He," JETP Letters **23** (12).
Tsymbalenko, VL (1977), "Measurements of the yield strength for crystalline," Zhurnal Ehksperimental'noj i Teoreticheskoj Fiziki **72** (5), 1885–1890.
Tsymbalenko, VL (1978), "Measuring internal friction in solid $^4$He," Zhurnal Ehksperimental'noj i Teoreticheskoj Fiziki **74** (4), 1507–1515.
Tsymbalenko, VL (1979), "Effect of plastic deformation and impurities on internal friction in solid $^4$He," Zhurnal Ehksperimental'noj i Teoreticheskoj Fiziki **76** (5), 1690–1699.
Tsymbalenko, VL (1984), "Measurement of the temperature dependence of the shear modulus of solid $^4$He," Soviet Physics JETP **60**, 537.
Tsymbalenko, VL (1986), "Effect of $^3$He impurities on the internal friction in crystalline $^4$He," Zhurnal Ehksperimental'noj i Teoreticheskoj Fiziki **91**, 941.
Tsymbalenko, VL (1992), "A possible observation of quantum nucleation in superfluid $^4$He near crystallization," Journal of Low Temperature Physics **88**, 55–71.
Tsymbalenko, VL (1995), "Study of the growth kinetics of facets in a free-growing $^4$He crystal," Fizika Nizkikh Temperatur **21**, 162–172.
Vekhov, Ye, and Robert B Hallock (2012), "Mass flux characteristics in solid $^4$He for T $>$ 100 mK: Evidence for bosonic Luttinger-liquid behavior," Physical Review Letters **109** (4), 045303.
Vekhov, Ye, WJ Mullin, and Robert B Hallock (2014), "Universal temperature dependence, flux extinction, and the role of $^3$He impurities in superfluid mass transport through solid $^4$He," Physical Review Letters **113** (3), 035302.
Vignos, James H, and Henry A Fairbank (1961), "New solid phase in $^4$He," Physical Review Letters **6** (6), 265.
Wagner, Raymond, Stephen C. Steel, Olga A. Andreeva, Reyer Jochemsen, and Giorgio Frossati (1996), "First observation of (100) and (211) facets on $^3$He crystals," Physical Review Letters **76**, 263–266.
Wang, Chia-Lai, and Glenn Agnolet (1992), "Effects of $^3$He impurities on the $^4$He solid-liquid interface," Journal of Low Temperature Physics **89** (3-4), 759–762.
Wanner, R (1971), "Elastic constants of bcc $^3$He from measurements of sound velocity, Debye temperature and compressibility," Physical Review A **3** (1), 448.
Wanner, R, I Iwasa, and S Wales (1976), "Evidence for dislocations in solid hcp helium-4 from sound velocity experiments," Solid State Communications **18** (7), 853–856.
Wanner, R, KH Mueller, and HA Fairbank (1973), "Temperature dependence of the sound velocities and elastic constants of bcc $^3$He," Journal of Low Temperature Physics **13** (1-2), 153–173.
Wanner, R, and KH Mueller Jr (1974), "The temperature dependence of the longitudinal sound velocity in solid $^4$He," Physics Letters A **49** (3), 209–210.
Weertman, J (1955), "Theory of steady-state creep based on dislocation climb," Journal of Applied Physics **26** (10), 1213–1217.
Werthamer, NR (1969), "Theory of quantum crystals," American Journal of Physics **37** (8), 763–782.
West, Joshua T, Oleksandr Syshchenko, John Beamish, and Moses HW Chan (2009), "Role of shear modulus and statistics in the supersolidity of helium," Nature Physics **5** (8), 598.
Wilks, John (1967), *The properties of liquid and solid helium* (Clarendon Press).
Wolf, PE, F Gallet, S Balibar, E Rolley, and Ph Nozieres (1985), "Crystal growth and crystal curvature near roughening transitions in hcp $^4$He," Journal de Physique **46** (11), 1987–2007.
Zhou, Caizhi, Jung-Jung Su, Matthias J Graf, Charles Reichhardt, Alexander V Balatsky, and Irene J Beyerlein (2013), "Plastic response of dislocation glide in solid helium under

dc strain-rate loading," Physical Review B **88** (2), 024513.
Zhuchkov, VA, AA Lisunov, VA Maidanov, AS Neoneta, V Yu Rubanskyi, SP Rubets, E Ya Rudavskii, and SN Smirnov (2015), "Creep in solid $^4$He at temperatures below 1 K," Low Temperature Physics **41** (3), 169–176.